On the applicability of fast neutral He beams for fusion plasma diagnostics

PhD thesis

by

Susanne MENHART

Institut für Allgemeine Physik

Vienna University of Technology

Vienna, Austria

November 2000

Abstract

Precise knowledge of plasma temperature- and -density profiles in experimental fusion plasmas is a prerequisite for satisfactory understanding and modelling of plasma confinement. The photon emission from fast lithium beams has been successfully used for the measurement of density profiles in the scrape-off layer. From the photon emission of thermal helium beams, electron density- and -temperature profiles can be deduced. Both, thermal helium- and fast lithium beams, have a penetration depth limited to the scrape-off layer of plasmas. By using fast helium beams with a much deeper penetration it is expected to also extend the range of measurements deeper into the plasma.

Fast neutral helium beams can be produced by neutralizing an accelerated helium-ion beam by collisions with a target gas. After this neutralization process a fraction of the helium atoms is in the metastable states. Atoms in metastable states have much higher cross sections for processes relevant in fusion plasmas than those in ground state. The first part of this thesis is therefore devoted to the production and characterization of so-called mixed beams, i.e. beams with a sizeable metastable fraction. These experiments were carried out at the Institut für Allgemeine Physik (IAP) using an existing 2.45 GHz ECR ion source. Helium-ion beams of up to 12.5 keV energy have been produced and subsequently neutralized in sodium vapour and/or helium gas. The beam composition was measured spectroscopically by a neon-gas filled attenuation chamber using the emission of either a NeI line (633 nm) or a HeI line (389 nm). Helium beams with metastable fractions of up to about 80% could be produced.

In the second part of this thesis the potential of helium beam emission spectroscopy as diagnostic tool is investigated by modelling the photon emission of a helium beam penetrating typical fusion plasmas. The calculations are based on a collisional-radiative model developed by the ADAS group at the University of Strathclyde, Glasgow. The code SCOTTIE, written at IAP in ANSI/C, solves the differential balance equation of the He-beam flux and -composition on its way through the plasma. By using typical temperature- and density profiles from ASDEX-Upgrade and JET, the photon emission profiles are calculated taking the metastable triplet fraction as a free parameter. From these modelling calculations the sensitivity of the method with respect to electron density and -temperature can be extracted. The photon emission at some visible lines is mainly sensitive to the plasma density, with only weak dependence to electron temperature. Other lines show a higher temperature sensitivity of the order of 20%, i.e. a 100% increase in temperature results in a 20% increase in emission intensity. It is expected that both temperature- and density profiles can be derived iteratively from measured photon emission profiles using suitable HeI lines.

In the last section of this thesis the modelling calculations are applied to Helium-beam emission profiles measured at ASDEX Upgrade- and JET Plasmas. Comparison between measurement and modelled photon-emission profiles, calculated from density- and temperature profiles taken from other diagnostics, shows a promising agreement.

The calculations performed in this thesis and the preliminary experiments at tokamak plasmas seem to confirm that fast He beams may serve for useful plasma temperature and -density diagnostics in a much larger plasma region than the one covered by lithium- or thermal helium beam diagnostics. However, appropriate methods to derive temperature- and density profiles from such measured HeI-emission profiles still have to be developed.

Contents

Chapter 1

Introduction

1.1 Motivation

Until a few years ago experimental phenomena like particle and energy transport in magnetically confined plasmas could not be reproduced satisfactorily by plasma theory. In the last years some improvement could be achieved, but there is still need for a more detailed understanding of the processes involved. For illustration, figure 1.1 shows a comparison of theoretical and experimental results for ion heat diffusivity at JET.

The knowledge of the plasma parameters, especially in the plasma edge, is very important for the understanding of the plasma confinement in magnetic traps. In toroidal magnetically confined plasmas one distinguishes between the core plasma and the scrape-off layer. The core plasma is the region of closed flux surfaces, the scrape-off layer is the region where magnetically confined particles can get into contact with the vessel. In limiter plasmas (figure 1.2, left illustration) this contact occurs at the limiter, in so-called X-point plasmas the particles hit a divertor (figure 1.2, right illustration). In both scenarios the magnetic field lines outside the separatrix, i.e. the last closed flux surface, connect into the wall. The term 'plasma edge' denotes the separatrix and the scrape-off layer.

Energy and particle transport through the plasma edge are crucial for both the properties of the core plasma and the power deposition onto the wall. For understanding of transport phenomena in the plasma edge and for the definition of the input parameters in transport codes a precise knowledge of the temperature- and density gradients is essential.

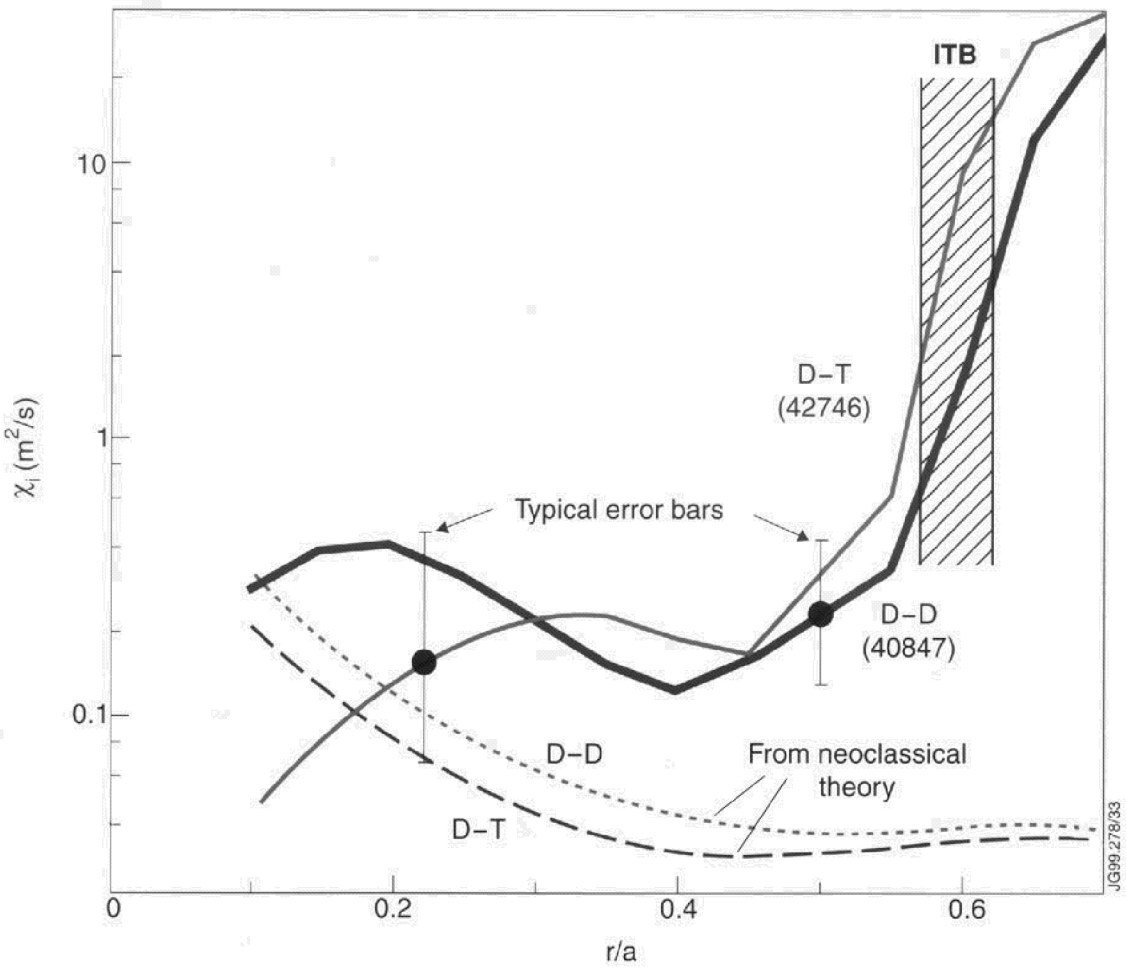

Figure 1.1: Radial ion thermal diffusivity profiles for typical optimized shear pulses in D-D- (discharge #42746) and D-T plasmas (discharge #40847) at JET [4].

Four different types of plasma confinement have been identified experimentally:

- L-mode confinement with smooth pressure profiles,
- H-mode confinement with reduced transport at the edge, leading to the formation of a so-called pedestal,
- ITB discharges in which an **i**nternal **t**ransport **b**arrier with a steeper pressure gradient is achieved by optimizing the current profile in L- or H-mode plasmas,
- RI-mode confinement where a transport barrier is produced by injection of impurities [6, 7].

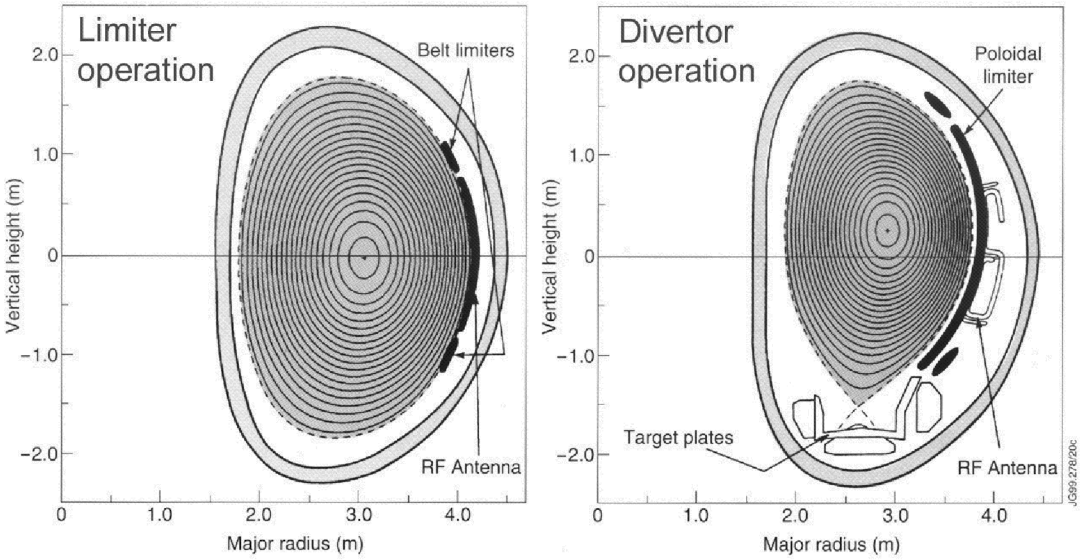

Figure 1.2: Schematic diagram of poloidal magnetic flux surfaces. Left: with a limiter, right: with a divertor ('target plates'). The concentric curves indicate the closed magnetic flux surfaces, the dashed line the separatrix [4].

The first three of these regimes are shown in figure 1.3. The change in temperature- and density profiles during the development of an ITB is illustrated in figures 1.4 and 1.5.

The formation of transport barriers has a dramatic effect onto plasma performance [9, 10]. Hence, for a detailed understanding of all processes affecting confinement, a precise knowledge of the temperature- and density gradients of both the edge transport barrier and the ITB is essential. However, no satisfactory method for a high local resolution measurement of these steep-parameter profiles, especially the temperature profiles (see figures 1.1 and 1.5), exists until now. Consequently, there is a strong interest in the development of diagnostics accommodating this demand. A newly developed method, fast He beam diagnostics, could be a suitable candidate for this. The aim of this work is to explore the diagnostic capabilities of fast He beams.

In the next chapters a survey of the most important diagnostic methods for the determination of plasma temperatures and -densities will be given. In chapter 1.3 the principle of fast He beam diagnostics is explained.

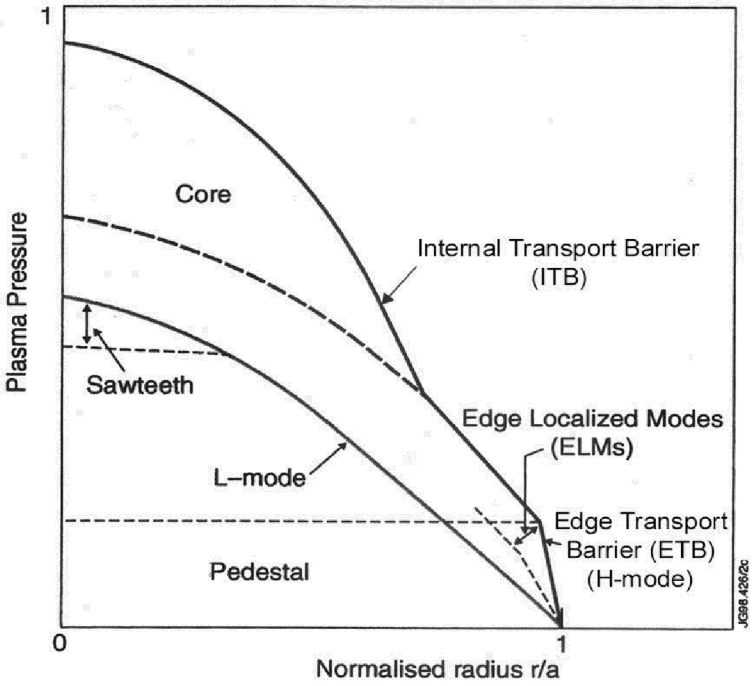

Figure 1.3: Normalized plasma-pressure profiles of L- and H-mode plasmas with and without internal transport barrier [5]. r stands for the major radius, a for the radial position of the separatrix (r/a=1).

1.2 Established Diagnostic Methods

The progress in fusion research over the last decade is not only measured by its success on the way to controlled fusion but also by the parallel development of novel diagnostic tools providing reliable and quantitative values of relevant plasma parameters. Because of the high temperatures in nowadays fusion plasmas, methods involving physical contact with the plasma can be used only at the outermost part of the discharge. Hence, for measurements in the plasma core, non-invasive techniques have to be used. Some methods are 'passive' and utilize particles or radiation that are emitted spontaneously by the plasma. 'Active techniques' use beams of particles or radiation from external sources as probes. The following diagnostic methods for determining electron- and ion density and -temperature are of relevance for present magnetically confined fusion experiments:

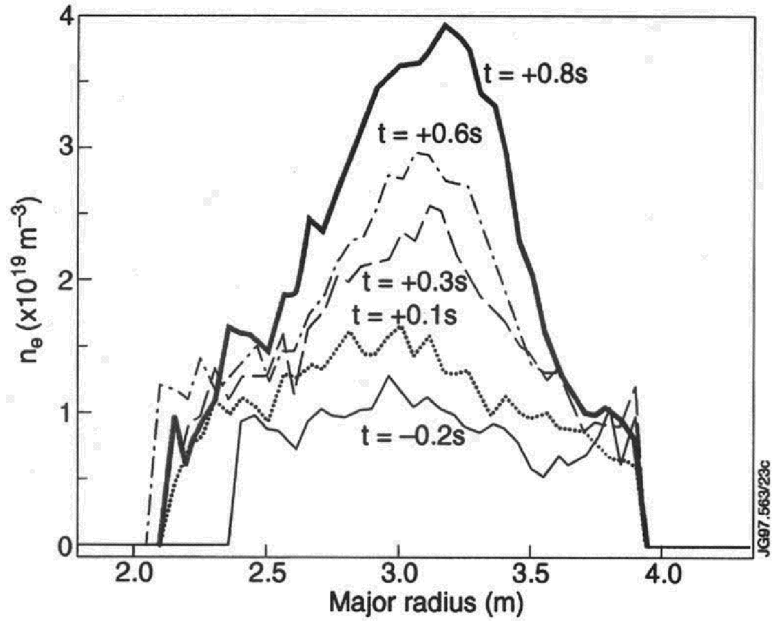

Figure 1.4: Change in electron-density profiles during the production of ITBs in a JET D-T plasma (discharge #42940) [8]. The separatrix is located at a major radius of about 3.85 m and 2.15 m, respectively.

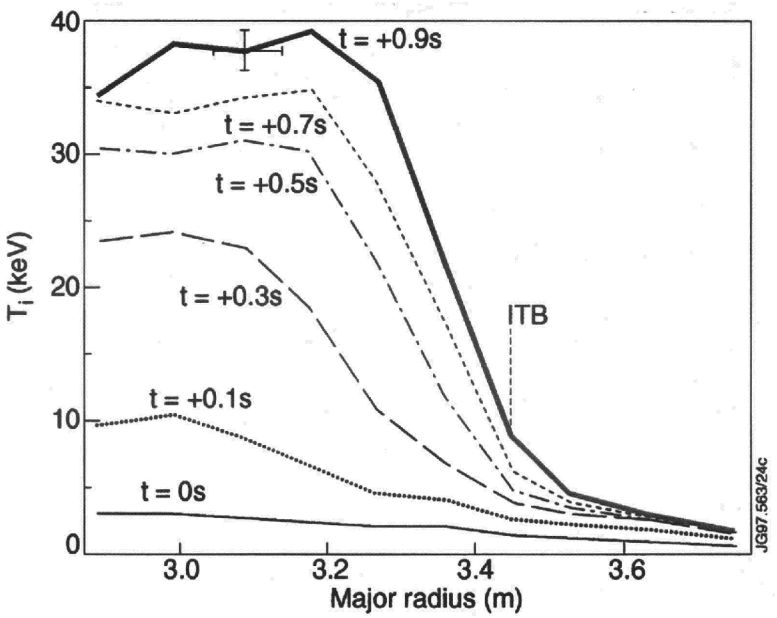

Figure 1.5: Change in ion-temperature profiles during the production of ITBs in a JET D-T plasma (discharge #42940) [8].

Langmuir probes
Thomson scattering
electron cyclotron emission (ECE)
reflectometry
interferometry
laser induced fluorescence
neutral particle analysis
neutral beam diagnostics (Li, fast H and D, and thermal He)

1.2.1 Langmuir Probes

This technique, developed by Irving Langmuir in the 1920s, is based on current measurements. In its simplest form, a Langmuir probe consists of a single electrode inserted into the plasma. A voltage is applied to the probe with respect to the vessel and the resulting current through the electrode is measured. From the current-voltage characteristics the electron density and -temperature at the position of the probe can be deduced.

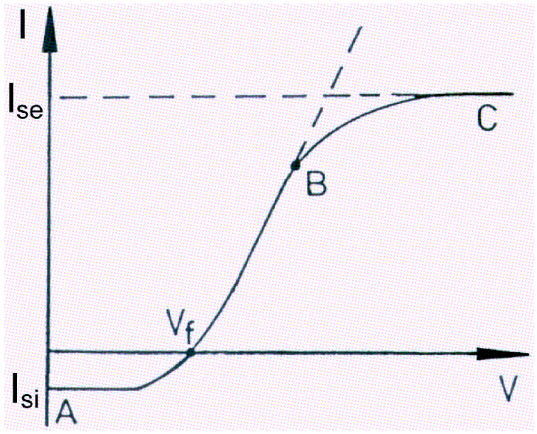

Figure 1.6: Current-voltage characteristics of a Langmuir probe [11], details are explained in the text.

Figure 1.6 shows the current-voltage characteristics of a Langmuir probe. V denotes the applied voltage, I the current through the probe, and V_f the floating potential which is reached when the net current is zero (if electrically isolated, the probe would float at this potential). The saturation current I_{si} is reached for strong negative voltage (all electrons are repelled), the electron saturation current I_{se} for strong positive voltage (all ions are repelled). The current-voltage profile between $I(V = 0)$ and I(B) (see figure 1.6) follows approximately

$$ln\,(I + I_{si}) \propto \frac{e\,V}{k_B\,T_e}\,. \tag{1.1}$$

where e denotes the elementary charge ($1.602{\cdot}10^{-19}$ C) and k_B the Boltzmann constant ($1.38{\cdot}10^{-23}$ J/K). Hence, the electron temperature T_e at the probe position can be determined by measuring V, I, and I_{si}. Assuming equal ion- and electron temperatures leads to the following correlation between I_{se} and the electron density n_e:

$$I_{se} = e\,n_e\sqrt{\frac{k_B\,T_e}{2\,\pi\,m_e}}\,S\,. \tag{1.2}$$

S stands for the projected surface area of the inner electrode seen by the plasma and m_e for the electron mass ($9.109{\cdot}10^{-31}$ kg). In magnetized plasmas, the measured I_{se} is much less than expected from theory. Only the tail of the electron distribution (about 5% of the total) is collected [12]. Nevertheless, n_e can be derived from measurement of I_{si} assuming equal T_i and T_e:

$$n_e = \frac{I_{si}}{e\,S}\sqrt{\frac{2\,\pi\,m_i}{k_B\,T_e}}\,, \tag{1.3}$$

m_i denotes the ion mass.

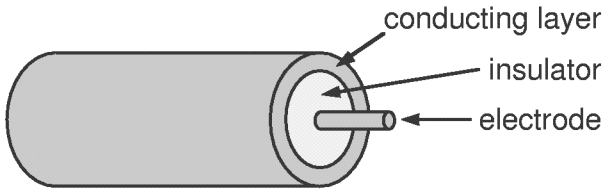

Figure 1.7: Schematic construction of a coaxial Langmuir probe.

Figure 1.7 shows a typical Langmuir probe of coaxial construction. It consists of an inner electrode made of heavy metal (e.g. platinum, molybdenum) sticking out of an isolating layer (e.g. alumina, quartz), which is shielded by a conducting layer.

The probes have to be in contact with the plasma and can only be used in areas where the power density is below the limit set by the probe material. The use of so-called 'reciprocating probes', i.e. an array of Langmuir probes which is only shortly inserted into the plasma edge (see figure 1.8), allows to extend the diagnostic region deeper into the plasma. However, the application of this type of probes is confined to plasma regions where $T_e \leq 100$ eV and $n_e \leq 10^{20}$ m^{-3}. At higher particle fluxes the probe would be destroyed leading to an increase

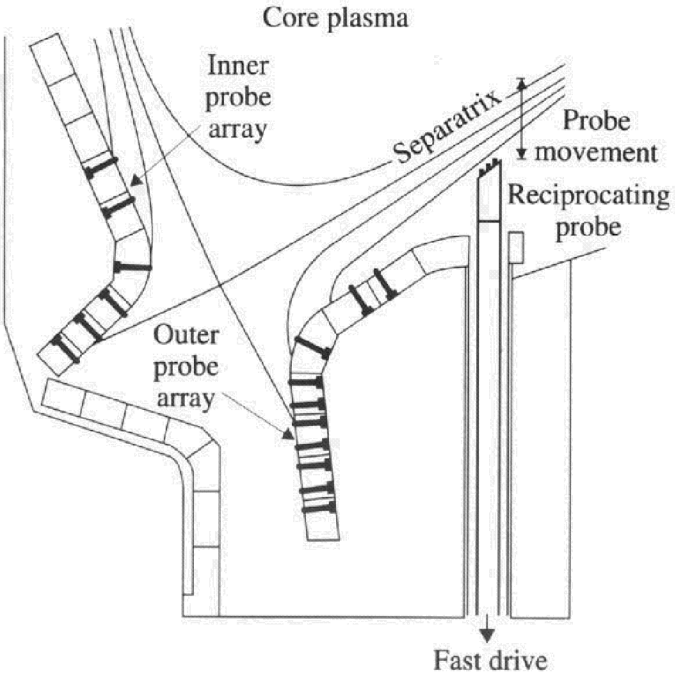

Figure 1.8: Fast reciprocating Langmuir probe and fixed Langmuir probe arrays in the divertor region of Alcator C-mod tokamak [12, 13].

of the impurity density and to undesired cooling of the plasma edge. Hence, the use of Langmuir probes inside the separatrix is fairly limited, even if installed on a reciprocating probe. An additional disadvantage of this diagnostic method is the difficult interpretation of the measured signals in the presence of high magnetic fields.

1.2.2 Thomson Scattering

Thomson scattering is used for measuring electron temperature- and density profiles by directing a laser beam into the plasma and detecting the scattered radiation.

Charged plasma particles hit by the laser light are accelerated and emit electromagnetic radiation like Hertzian dipoles. Being based on charge acceleration, this effect is much larger for electrons because of their smaller mass than for any other plasma particle. The differential cross section for Thomson scattering at an electron is given by

$$\frac{d\sigma}{d\Omega} = r_o^2 \, sin^2\theta = \left(\frac{e^2}{4\,\pi\,\epsilon_o\,m_e\,c^2} \right)^2 sin^2\theta\,, \tag{1.4}$$

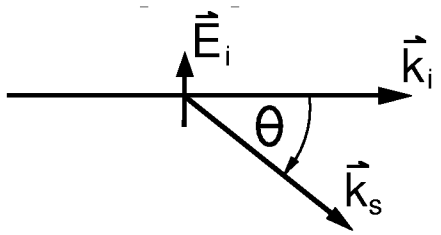

Figure 1.9: Definition of the scattering angle θ. $\vec{k_i}$ and $\vec{k_s}$ denote the wave vector of the incident and the scattered light wave, respectively, $\vec{E_i}$ stands for the electric field vector of the incident beam.

where Ω denotes the solid angle, r_o the 'classical electron radius' ($2.82{\cdot}10^{-15}$ m), θ the scattering angle (see figure 1.9), ϵ_o the electric constant ($8.85{\cdot}10^{-12}$ $\frac{As}{Vm}$), and c the speed of light ($2.998{\cdot}10^{8}$ m/s). Due to the high electron temperature T_e, a scattered line with wavelength λ_o exhibits Doppler broadening with a full width at half maximum of

$$\Delta\lambda = 4\,\lambda_o\,sin\left(\frac{\theta}{2}\right)\sqrt{\frac{2\,k_B\,T_e\,ln2}{m_e\,c^2}}\,, \tag{1.5}$$

which makes it possible to determine T_e. The scattered power P_s per unit angle θ in the frequency bandwidth $d\omega$ is given by

$$P_s = P_o\,n_e\,r_o^2\,sin^2\theta\,L\,S(k,\omega)\,d\omega\,, \tag{1.6}$$

where P_o denotes the total incident laser power, L the interaction length, and $S(k,\omega)$ the spectral density function. k stands for the magnitude of the difference between incident and scattered wave vectors and ω for the difference between scattered and incident frequencies [12]. The dependence of P_s on n_e allows the determination of the latter by measuring the differential scattered power, which requires a much higher laser power or a much better sensitivity of the detection system than needed in T_e measurements. At JET several of these Thomson laser beams are installed and used for real-time controlling of n_e [14].

As P_s depends on r_o^2 ($8{\cdot}10^{-30}$ m^2), the scattering effect is quite weak. In order to get signals from the scattering processes exceeding the background radiation, multimegawatt pulsed lasers (Nd:YAG or ruby lasers) and very sensitive detection systems have to be used. Figure 1.10 shows the technique usually termed 'Thomson scattering'. Here the scattered light is observed at angles close to perpendicular to the beam path. In another version of the Thomson scattering method called 'LIDAR' (**li**ght **d**etection **a**nd **r**anging) a pulsed

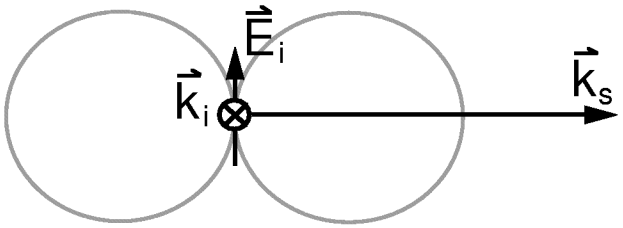

Figure 1.10: Principle of Thomson scattering measurements with observation perpendicular to the laser beam. $\vec{k_i}$ and $\vec{k_s}$ denote the wave vector of the incident and the scattered beam, respectively. $\vec{E_i}$ stands for the electric field vector of the incident beam.

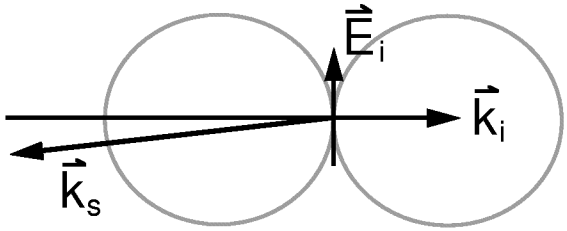

Figure 1.11: Principle of LIDAR measurements. $\vec{k_i}$ and $\vec{k_s}$ denote the wave vector of the incident and the scattered beam, respectively. $\vec{E_i}$ stands for the electric field vector of the incident beam.

laser is used and the backscattered light is recorded as function of time by a fast detection and recording system. As the laser pulses are rather short, the position of the laser photon packet is known at each time point. LIDAR uses the time of flight of this short laser pulse to spatially resolve the n_e and T_e data. Figure 1.11 shows the geometry for this diagnostic. At the LIDAR system at JET the pulse duration is 300 ps (9 cm wave packets) and the repetition rate 4 Hz. With this system a local resolution of 5 cm could be achieved [15].

Thomson scattering systems observing perpendicular to the incident laser beam require at least two approximately orthogonal views, i.e. one for the incident beam and another for the observation system. The latter has to allow wide angle observations (see figure 1.12). LIDAR requires only a single line of sight access to the plasma, which makes this kind of diagnostic more favourable for future fusion devices. Nevertheless, all temperature profiles of transport barriers determined by Thomson scattering or LIDAR known to the author (e.g. figure 1.5) are characterized by low spatial resolution and do not allow evaluation of detailed T_e profiles.

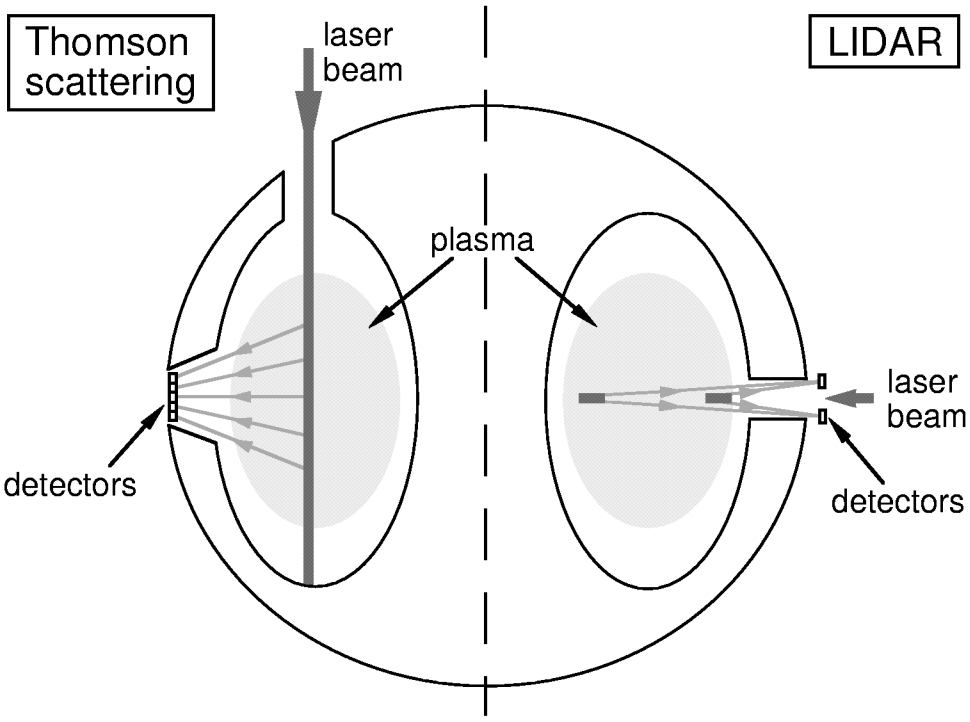

Figure 1.12: Schematic view of the Thomson scattering and the LIDAR system installed at JET.

1.2.3 Electron Cyclotron Emission (ECE)

This passive diagnostic method makes use of the electron gyration in a magnetic field. During this acceleration movement the electrons emit radiation at frequencies ω corresponding to the electron cyclotron frequency ω_{ce} and its harmonics

$$\omega = l\,\omega_{ce} = l\,\frac{e\,B}{m_e}, \tag{1.7}$$

where l (l = 1,2,3...) denotes the harmonic number and B the local magnetic field. Under some circumstances, the intensity of the emission is directly related to T_e. In the general case the calculation of the electron cyclotron emission of a plasma is extremely complicated. Even for the simplified case of a plasma with Maxwellian velocity distribution and electron densities $n_e \leq 10^{20}$ m^{-3}, the emission $j(l\,\omega_{ce})$ is a rather complicated function of T_e, l, and of the angle θ between the direction of the emission and the confining magnetic field [12].

This correlation becomes very simple if the plasma is optically thick for the frequency ω under consideration. This means that the optical depth $\tau(\omega)$, an absolute measure of the

plasma for this frequency defined by

$$\tau(\omega) = \int \alpha(\omega, s)\, ds\,, \tag{1.8}$$

should be larger than 1. In equation 1.8 $\alpha(\omega, s)$ stands for the absorption coefficient of the wave in the plasma which has to be integrated along the line of sight (line parameter s). In this case, the wave gets re-absorbed in the plasma and the radiation intensity becomes that of a blackbody. For typical Tokamak experiments ($2\,T \leq B \leq 8\,T,\ 5\,mm \geq \lambda \geq 0.5\,mm$), the emission lines of interest are on the long wavelength side of the blackbody spectrum ($h\nu \ll k_B T_e$). Hence, the Rayleigh-Jeans law holds,

$$I_n(\omega) = \frac{\omega^2\, T_e}{8\,\pi^3\, c^2}\,, \tag{1.9}$$

allowing the calculation of T_e from the measurement of the intensity $I_n(\omega)$ of the emission of an optically thick harmonic.

The fundamental wave is absorbed at the upper hybrid resonance with the frequency

$$\omega_{uh} = \sqrt{\omega_{pe}^2 + \omega_{ce}^2} \approx \omega_{ce}\,, \tag{1.10}$$

where

$$\omega_{pe} = \sqrt{\frac{n_p\, e^2}{\epsilon_o\, m_e}} \tag{1.11}$$

denotes the electron plasma frequency. Thus, the fundamental wave can not be detected. Consequently, the second harmonic ($\omega = 2\,\omega_{ce}$) is commonly chosen for the measurement.

The magnetic field B of a Tokamak varies inversely with the major radius R. Consequently the electron cyclotron frequency shows the same $1/R$ behaviour. This means that the frequency of the emission can be used to deduce the radial location of the source of the emission and, hence, the spatial T_e profile can be deduced. The spatial resolution is typically a few cm, which limits the local resolution for high T_e gradients.

There are several effects that can limit the usefulness of this diagnostics, such as deviation of the velocity distribution from Maxwellian, plasma currents which generate an additional magnetic field, refraction of the emission light, and density effects which change the propagation properties. Due to large variations of the magnetic field in the plasma, two or even more harmonics may be resonant at the same frequency at different radii ('harmonic overlap').

Comparison of results for T_e from ECE and Thomson scattering measurements show that the derived ECE data are reliable for $T_e \cdot n_e \geq 3 \cdot 10^{18}\,\mathrm{keV\,m^{-3}}$. Below this plasma pressure the optical depth is decreased to such an extent that the plasma can not be considered a blackbody any more. Hence, the simple correlation between T_e and $I_n(\omega)$ given above does not hold any longer. Effects like the reflectivity of the inner wall of the plasma vessel become important. Measurements during H-modes with very steep edge T_e gradients and low densities showed enhanced emission (local maximum of T_e outside the separatrix). This phenomenon is not fully understood until now, an explanation could be a non-thermal electron velocity distribution due to enhanced transport of fast electrons in this region [16].

1.2.4 Reflectometry

A beam of microwave radiation is directed into the plasma and reflected at the density layer where the local electron density is equal to the cut-off density (cf. equ. 1.11) which is a function of the wave frequency. By sweeping the frequency, the electron-density profile can be determined.

The refractive index N for a so-called 'ordinary' electromagnetic wave (electric vector parallel to magnetic field) with the frequency ω is given by

$$N = \sqrt{1 - \frac{\omega_{pe}^2}{\omega^2}} = \sqrt{1 - \frac{n_e\, e^2}{\epsilon_o\, m_e\, \omega^2}}\,. \tag{1.12}$$

At the location where the electron density exceeds the critical density

$$n_c(\omega) = \frac{\epsilon_o\, m_e\, \omega^2}{e^2} \tag{1.13}$$

an electromagnetic wave of the frequency ω can not propagate any more and thus becomes reflected.

Using a Michelson interferometer, the phase shift between the incident and the reflected wave can be measured, which makes it possible to determine the position of the corresponding $n_c(\omega)$ layer (so-called 'cut-off layer') as shown in figure 1.13. By tuning the laser frequency the electron-density profile can be measured. The accessible density area is limited by the frequency range of the tuneable microwave source. E.g. at JET the reflectometer used covers the density range $4{\cdot}10^{18}$ m^{-3} to $8{\cdot}10^{19}$ m^{-3} [12]. Furthermore, only monotonously increasing density profiles can be measured, and the measurements can be disturbed by local density fluctuations.

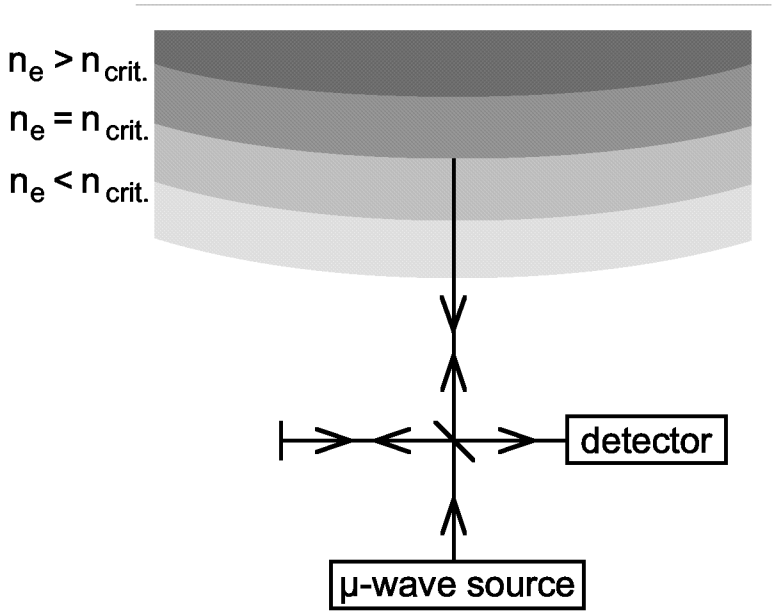

Figure 1.13: Schematic diagram of a reflectometer for determining n_e profiles.

1.2.5 Interferometry

Transmission interferometry is one of the oldest established diagnostic methods for measuring the electron-density profile. A laser beam is split by semipermeable mirrors into several coherent waves which are directed through the plasma (see figure 1.14). From the phase shifts of the single beams the electron-density profile can be deduced. In this case the laser frequency has to be higher than the maximum plasma frequency in the region of interest. Therefore, usually lasers with frequencies in the far infrared, e.g. HCN-lasers, are employed.

The difference of the phases of a beam with frequency λ passing through a plasma and those of the reference beam is proportional to the electron density integrated along the beam path [12]:

$$\Delta\phi = \frac{\lambda\, e^2}{4\,\pi\,\epsilon_o\, m_e\, c^2} \int n_e\, dl\,. \tag{1.14}$$

These phase shifts can be measured, e.g. with a Michelson interferometer. From the known phase shifts, electron-density profiles can be deduced by tomographic inversion (Abel inversion). Multiple lines of sight through the plasma would be required in order to measure detailed plasma-density profiles. This appears to be extremely difficult to implement in a device such as ITER, i.e. the next major step for the development of nuclear fusion [17].

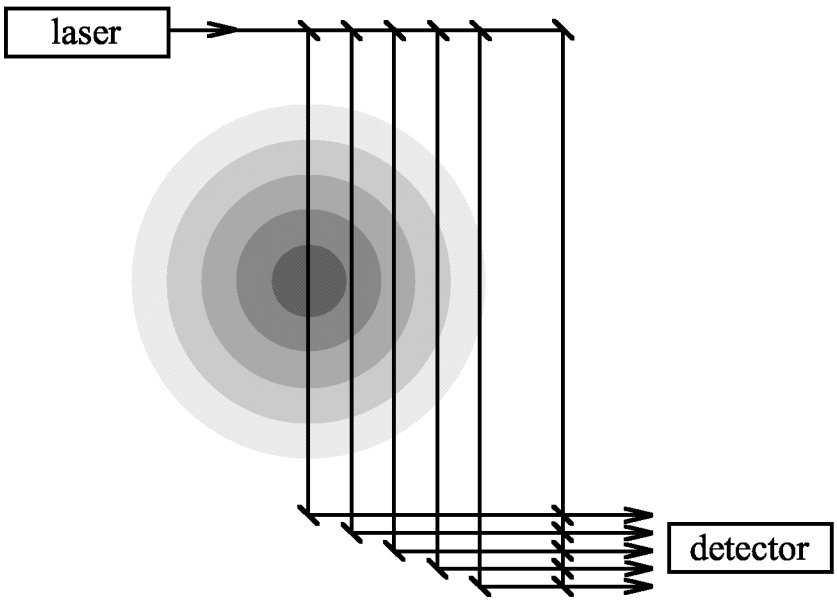

Figure 1.14: Schematic layout of an interferometer used for n_e measurements.

Even at JET there are insufficient lines of sight (5 vertical and 3 horizontal) to yield density profiles with good spatial resolution. Furthermore, interferometry systems are very sensitive to mechanical vibrations. In order to decouple from the tokamak, the interferometer at JET is mounted on a large, independently supported frame. For ITER such a frame would be impracticably large. Hence, the use of interferometry as major diagnostics for density-profile measurements at ITER is questionable [18]. From that point of view, reflectometry seems preferable, as the measurements are done by probing the plasma along a single line of sight.

1.2.6 Laser Induced Fluorescence (LIF)

In a fusion plasma, there is often a difference between T_i and T_e because the ion-electron equilibration time can become comparable to or even longer than the ion energy confinement time. This is especially the case for auxiliary-heated discharges (RF- or neutral beam heating). Hence, a dedicated diagnostic method for determining the temperature of ions is of high interest. LIF is a method for measuring temperature and density of atoms and non fully stripped ions.

In LIF, laser light of a frequency equal to the excitation frequency of the atom or ion of interest is directed through the plasma. The intensity and Doppler broadening of the fluorescent radiation emitted by the excited particles gives access to the density and temperature

of the latter. One of the most important applications of LIF is the Lyman-α-fluorescence. Here, laser light of the frequency 121.6 nm is used to excite hydrogen atoms into their first excited level (n=2). This diagnostic requires neutrals or non-fully stripped ions, and is therefore rather limited. Nowadays, this diagnostics - no longer in use at the most important fusion experiments - has been replaced by neutral particle analysis and neutral beam charge-exchange spectroscopy.

1.2.7 Neutral Particle Analysis

This method makes use of fast neutrals escaping the plasma for determining ion-temperature profiles. Plasma neutrals have their origin either on the vessel wall or in low-charged ions recombining with other plasma particles. These slow neutrals are not confined by the magnetic field and, therefore, can either escape from the plasma or penetrate deeper into the plasma where a charge-exchange process with a plasma ion leads to a secondary neutral, and so on. By this process at low densities the hydrogen atoms can penetrate into the plasma center [12]. Hence, measurements of escaping neutrals give access not only to parameters of edge ions but also of core ions.

The neutral flux escaping a Maxwellian plasma is given by

$$S(E_o) = n_o\, n_i\, \langle \sigma_{01} v_i \rangle \, \frac{2\sqrt{E_0}}{\sqrt{\pi}\,\sqrt[3]{k_B T_i}}\, e^{\frac{E_o}{k_B T_i}}\,, \tag{1.15}$$

where E_o stands for the energy of the neutrals, n_o and n_i for the density of the neutrals and ions, respectively, and σ_{01} for the charge-exchange cross section. If n_i is known, the measurement of $S(E_o)$ gives access to T_i and n_o. One prerequisite for the applicability of equation 1.15 is that the mean free path of the escaping neutrals has to be much greater than the plasma radius a,

$$\frac{1}{n_i\, \sigma_{01}} > a\,, \tag{1.16}$$

which is correct for higher energies as σ_{01} decreases with increasing energy.

In the detection system the neutral particles are ionized in a gas stripping cell or thin carbon foil and afterwards analysed due to their energy and mass. The detected values for T_i and n_o are line-of-sight averaged. Thus, for the determination of radial profiles of these parameters, the measured values have to be interpreted by rather complicated plasma modelling [19]. Due to the complexity of these calculations, the results are - under some circumstances -

not very reliable. Application at small and medium tokamaks was quite successful but, for larger tokamaks, these measurements become less feasible because neutrals produced in the plasma center are ionized before leaving the plasma [12].

1.2.8 Neutral Beam Diagnostics

Neutral beams injected into the plasma are widely used for active spectroscopic measurements of key plasma parameters (see e.g. [20]). Two processes between beam atoms (B^o) and plasma particles (A^q, e) are important, i.e. charge-exchange reactions between beam atoms and plasma ions which in general lead to excitation of the latter,

$$B^o + A^q \rightarrow B^+ + (A^{q-1})^* , \tag{1.17}$$

and the excitation of the beam atoms themselves by collisions with electrons and ions,

$$B^o + A^q, e \rightarrow (B^o)^* + \dots . \tag{1.18}$$

Spectroscopy based on observing photons emitted by the plasma ions (or neutrals) is called 'charge-exchange spectroscopy' (CXS), observation of photons emitted by the beam atoms is termed 'beam emission spectroscopy' (BES) or 'impact excitation spectroscopy' (IXS). From the intensity of the CXS emission lines - determined by the density of the plasma ions, the flux density of the neutral beam, and the respective cross sections - the ion density can be deduced if the beam attenuation and the cross sections are known. Ion temperature and plasma rotation can be derived from width and Doppler shift of the spectral line. As these diagnostics are based on charge exchange, they enable the deduction of the parameters mentioned above even for fully ionized ions, in contrast to LIF. BES gives access to electron density and -temperature (see chapter 1.2.8.2), but also the local magnetic field (see chapter 1.2.8.1).

1.2.8.1 Hydrogen and Deuterium Beam Diagnostics

Hydrogen or deuterium heating beams are widely used also for plasma diagnostics [21, 22]. One very important application of H and D beams is the investigation of fusion alpha particles (i.e. CXS) [23]. As mentioned above, the neutral-beam density on the beam path has to be determined. In principle, two methods serve this purpose. The first one involves the direct measurement of the Balmer-α emission of the excited beam atoms. Then with the use

of atomic modelling to evaluate effective Balmer-α emission coefficients, the local neutral-beam density can be recovered. The second method is based on a numerical calculation of the attenuation along the beam path, which takes into consideration the atomic processes which contribute to ionizing the beam neutrals [24]. Presently, the spectroscopic method is the more accurate one, although it has proved difficult for several reasons. Firstly, the observed D_α emission is disturbed by Doppler shifts and the motional Stark effect in the magnetic field $\vec{B}$ caused by the Lorentz field

$$\vec{U}_L = \vec{v}_b \times \vec{B}\,, \tag{1.19}$$

where $\vec{v}_b$ denotes the velocity of the beam atoms. Furthermore, D (or H) beams have unwanted fractional energy components due to the production of these beams. In the beam source D_2 gas is ionized and D^+, D_2^+, and D_3^+ (D^++D_2) are formed and accelerated by an electric field. After acceleration the ions are neutralized and dissociated in a gas cell. Neutrals from dissociated D_2^+ have only one half and those from D_3^+ have only one third of the full energy. These fractional energy components in the atom beam leads to a superposition of the single Stark multiplets. Hence, the interpretation of these spectra is complicated by a large number of fits [24].

The spectral shape of the Balmer-α line can also be used for deduction of the total magnetic field perpendicular to the neutral beam, and the polarization of the line gives access to the pitch angle of the local magnetic field [22].

A disadvantage of D beams besides the complexity of the spectra is the high neutron production from beam-beam and beam-plasma interactions [25]. These neutrons contribute to the activation of the vessel [14].

1.2.8.2 Lithium Beam Diagnostics

Lithium beams of ≈ 0.1 eV (thermal beams produced with an oven, [26]), several eV (laser blow-off technique, [27, 28]) or several 10 keV and some mA equivalent current (produced by neutralizing a Li ion beam [3]) may be injected into the plasma. The emission of the Li(2p$\rightarrow$2s) transition gives access to the electron density (Li-IXS [29]) and the emission of excited impurity ions makes it possible to determine the temperature- and density profiles of the latter (Li-CXS [30]). The basis of the interpretation of the observed Li-IXS spectra is a collisional-radiative model which includes all relevant processes between the Li atoms and the plasma particles. As the rate coefficient for electron-impact excitation of Li is almost

independent of the electron temperature in the range of the accessible diagnostic region (several eV to several 100 eV), the exact profile of T_e can be neglected and the determination of n_e out of the diagnostic measurements is simplified considerably. But this also means that T_e can not be measured by Li beam diagnostics.

Li beam diagnostics enables spatial resolutions of about 5 mm [3], which is sufficient for the determination of detailed edge gradients. But due to the low ionization energy of Li, i.e. 5.39 eV, the beam does not penetrate far beyond the scrape-off layer in dense plasmas of nowadays tokamaks. Even fast lithium beam diagnostics is confined to the plasma edge and the outermost part (few cm) of the core plasma. Moreover, the error of n_e values rises for increasing penetration depth [3] due to the beam attenuation which results in decreasing signal intensities.

Figure 1.15 shows a typical H-mode n_e profile determined by Li-IXS in the plasma edge and by DCN-laser interferometry in the core plasma at ASDEX Upgrade. None of the diagnostics covers the pedestal region. This illustrates that a diagnostic covering both the edge transport barrier region and parts of the plasma inside the pedestal is desirable.

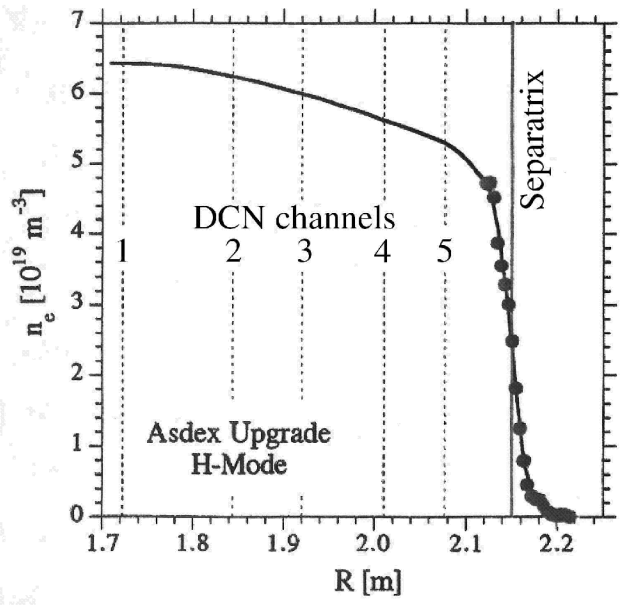

Figure 1.15: Typical H-mode n_e profile at ASDEX Upgrade. The broken lines denote the radial positions of the 5 DCN-laser interferometry channels, the circles denote the Li-IXS measurements [31].

This problem in the pedestal region gets worse for larger tokamaks (see figure 1.16 as an example for JET), especially for future devices, as the line integrated density rises.

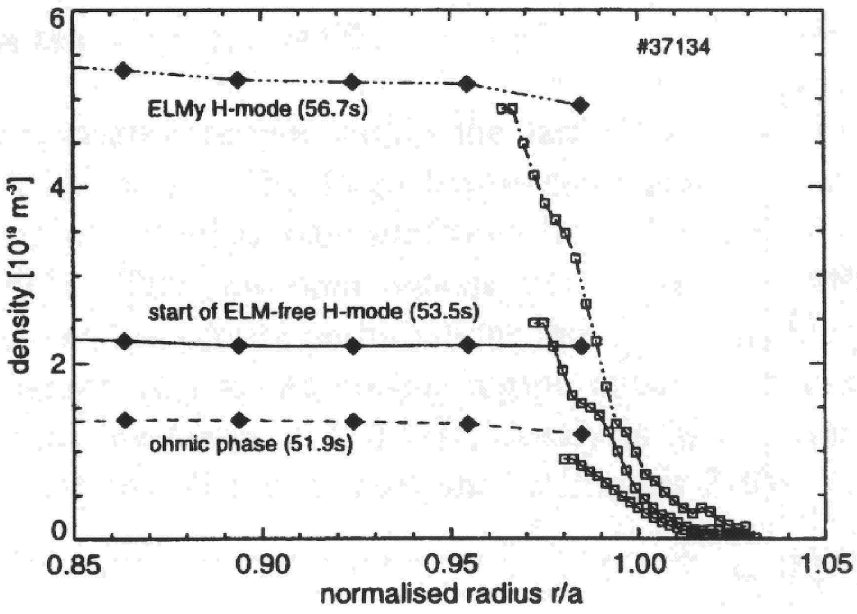

Figure 1.16: Density profiles for three different phases of a JET discharge. The black diamonds denote LIDAR measurements, the open squares Li beam diagnostics results [9].

1.2.8.3 Thermal Helium Beam Diagnostics

Thermal He beams - produced in an oven or by supersonic expansion through a nozzle - are injected into the plasma edge. At these beam energies the cross sections for reactions between the beam atoms and plasma ions can be neglected, see chapter 3.1. Neutral He has two different spin systems, i.e. singlet and triplet. The triplet system can only be populated from the He ground state by spin-changing processes. The different electron-temperature behaviour of the excitation cross sections for spin-conserving and spin-changing collisions gave rise to expectation, that the line-intensity ratio of a HeI-singlet and a HeI-triplet line should give access to the electron temperature [32]. On the other hand, the line-intensity ratio of two singlet lines can be used for the determination of the electron density. The deduction of n_e and T_e from line-intensity ratios is possible for thermal beams as the relevant excited levels are relaxed in typical tokamak discharges [33, 34]. Extensive calculations with a collisional-radiative model (cr-model, see chapter 3.2) make it possible to identify the most suitable ratios.

At TEXTOR, the ratio of the HeI emission at 728 nm ($3^1S \rightarrow 2^1P$) and at 707 nm ($3^3S \rightarrow 2^3P$) has been chosen for T_e measurements. The electron density is accessed by determining the ratio of the HeI emission at 728 nm and at 668 nm ($3^1D \rightarrow 2^1P$). Figure 1.17 shows the line-intensity ratios for 728 nm/707 nm and 668 nm/728 nm in the n_e-T_e-plane which are

used for the deduction of the n_e- and T_e profiles at TEXTOR [36].

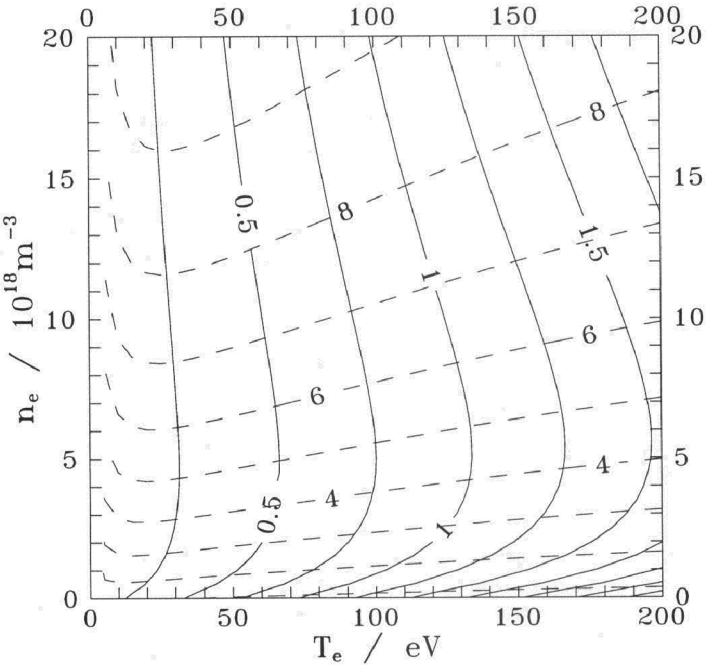

Figure 1.17: Line-intensity ratios for 728 nm/707 nm (solid line) and 668 nm/728 nm (broken line) in the n_e-T_e-plane for the deduction of the n_e- and T_e profiles [36].

Based on calculations performed with the cr-model by Fujimoto [34], several ratios of the emissions at 502 nm ($3^1P \rightarrow 3^1S$), 505 nm ($4^1S \rightarrow 2^1P$), 492 nm ($4^1D \rightarrow 2^1P$), and 471 nm ($4^3S \rightarrow 2^3P$) have been investigated at the NAGDIS-I linear plasma device (Nagoya University Divertor Simulator, [35]). The recommended line-intensity ratios are 492 nm/505 nm for the deduction of n_e and 505 nm/471 nm for T_e, respectively.

As the thermal He beams are ionized rather quickly, their diagnostic region is confined to the plasma edge (10^{18} m$^{-3} < n_e < 2 \cdot 10^{19}$ m^{-3} and 20 eV $< T_e <$ 200 eV [36]). A more detailed description of the diagnostic application and modelling of thermal He beams is given in chapter 3.1.

Summarizing the implementation of the methods described above, it is evident that there is considerable need for a method which allows to expand the diagnostic region deeper into the plasma than Li- or thermal He beams. This will be of special importance in view of future fusion devices which will involve much higher line integrated densities than the present ones. Furthermore, a more precise evaluation of T_e and n_e in plasma regions exhibiting high

gradients is desired. In the following chapter a new kind of plasma diagnostics using fast helium beams is presented, which seems to be a candidate for serving these purposes.

1.3 Fast Helium Beam Diagnostics

We assume that a neutral He beam of several 10 keV energy is injected into the plasma. As in the other neutral beam diagnostics mentioned above, observation of the HeI-line profiles should give access to the local n_e- and T_e profiles (BES). In addition, the emission lines of plasma-impurity ions which are excited via charge exchange with neutral He, may permit measurement of n_i and T_i (CXS). Furthermore, the resonant process of double charge exchange between ground-state He-beam atoms and plasma alpha particles enables the direct observation of the fast alpha particles (active neutral particle analysis [37]). As with Li beam diagnostics, a spatial resolution of several mm should be achievable.

Due to the high ionization energy of He atoms, fast He beams penetrate much deeper into the plasma than thermal He beams or fast Li beams. As with H or D beams, He beams could cover both the scrape-off layer and the core region. Besides the advantage of determining also n_e and T_e, neutral He beams produced by neutralizing a fast He-ion beam do not have fractional energy components as He does not form ionic molecules, and the He^{2+} fraction in the primary ion beam is negligibly small. Furthermore, He is not neutron producing - unlike deuterium.

Concerning CXS, the ground state helium atoms would be the primary donors for the $He^{+}(n = 4 - 3)$ emission lines, whereas $He(2^3S)$ metastable atoms would be primary donors for charge-exchange reactions like $C^{6+} \rightarrow C^{5+}(n = 8 - 7)$. Hence, for observation of the latter a high $He(2^3S)$ metastable fraction in the beam would be advantageous. In view of that application of He beams, so-called fast 'mixed' He beams, i.e. He beams with a high $He(2^3S)$ metastable fraction, were produced and characterized with regard to their composition in the first part of this thesis (chapter 2). These experiments were carried out at a 2.45 GHz ECR ion source of Institut für Allgemeine Physik (IAP). Also, the motional Stark effect on the $n \leq 3$ He levels is minimal. Hence, the $He(n = 3 \rightarrow 2)$ visible lines are not affected. This process becomes essential only for $n \geq 4$ shells, which in combination with the non-degenerate term structure of He may lead to the appearance of Stark induced forbidden lines [38]. This effect can be used for the determination of the internal magnetic field.

For quantitative interpretation of the observed line intensities, an extensive cr-model (see chapter 3.2) involving all collisions of importance between beam atoms and plasma particles had to be used. In contrast to the model used for thermal He beams, the ion-impact cross sections can not be neglected in comparison to the electron-impact cross sections (see chapter 3.1).

The line emission of fast He atoms inside a plasma has been modelled previously by several groups. Levinton [39] and Korotkov and Samsonov [40] developed a cr-model with the simplification of the metastables being in equilibrium relative to the ground state. This assumption was acceptable in view of calculating the attenuation of the He beam, as the most important process for ionizing the beam is ionization out of the ground state. This approach was continued by later work of Korotkov [41]. The population of each orbital-momentum substate of the low lying levels are evaluated, with the populations of the higher levels calculated for each principal quantum shell (nls-resolved/ns-resolved, cf. chapter 3.3). Korotkov and Janev [42] extended this work by using approximate methods to include metastable states of He. Brix [92] upgraded his cr-model for thermal He beams with proton impact- and charge-exchange cross sections. This model takes into account all levels up to $n = 5$.

During the last few years, a cr-model for He beams has been developed by the ADAS group at the University of Strathclyde, Glasgow [1], which is capable of calculating the He beam attenuation and excited state population structure. This is done by assembling effectively an infinite series of coupling equations (describing the population and depopulation of the single levels) with a varying resolution of substate populations [43]. The main part of this thesis presents modelling calculations based on this cr-model in order to investigate the diagnostic potential of a fast He beam. In chapter 3 the cr-model and the ANSI/C-code developed at IAP are described, which determine the population progression of the ground state and the two metastable states in the He beam, and resulting line-intensity profiles for optical lines of interest. In chapter 3.7 a survey of different methods for recalculating the electron density and -temperature from the observed emission lines is given. In order to make predictions for upcoming first experiments with fast He beams at Tokamak plasmas, calculations have been performed for He beams with various metastable fractions using electron density- and -temperature profiles typical for ASDEX Upgrade- and JET plasmas (chapter 4.1). Furthermore, the sensitivity of the line profiles to changes in electron density and temperature was analysed as presented in chapter 4.2. The last part of the present thesis - chapter 5 - deals with first relevant experiments performed at ASDEX Upgrade and JET, by which the results of these model calculations are compared with the experimental observations.

Chapter 2

Production and Characterization of Fast Mixed He Beams

As mentioned in the previous chapter the expectation that HeI beam emission could be used as electron temperature diagnostics is, among other reasons, based on the different energy dependence of the excitation of spin conserving and spin changing collisions. It was therefore felt useful to examine how the composition of a fast neutral He beam could be influenced with respect to its metastable fraction. Hence, fast He-atom beams with a comparably high metastable fraction (so-called mixed beams) were produced and analyzed in this part of the work. The actual experiments on tokamak plasmas have finally been performed by using the existing heating beam facilities, and modelling calculations revealed that the metastable population in the beam will be produced and destroyed more or less independently of the initial population. Furthermore it was discovered from calculations in view of the sensitivity of emission lines with respect to T_e and n_e (chapter 4.2) that a low metastable fraction in the beam is generally advantageous. Nevertheless, a brief description of the experimental setup at Institut für Allgemeine Physik (IAP), TU Wien, and the underlying physics will be given in the following chapters. The results of the experiments are discussed in chapter 2.3.

2.1 Underlying Physics

The following subsections deal with the physics for the production and characterization of mixed He beams.

2.1.1 Production of Mixed He Beams

Neutral He beams are produced from accelerated ion beams by charge-exchange collisions in a so-called neutralization cell. After neutralization, the remaining ions are removed from of the beam. A description of the applied ion source (2.45 GHz ECRIS [44, 45, 46]), the beam transport system, and the neutralization chamber [47] is given in chapter 2.2.

The probability for charge-exchange processes in the neutralization cell is strongly dependent on the energy defect ΔE between binding energies of the active electron after ($E_{B,beam}$) and before the collision ($E_{B,target}$):

$$\Delta E = E_{B,beam} - E_{B,target} \,. \tag{2.1}$$

For the energy range used (1 - 3 keV/amu) the charge-exchange process is resonant for processes with $\Delta E = 0$ or quasiresonant for $\Delta E \approx 0$ as the electron velocity is large compared to the velocity of the projectile ion.

In order to produce a He-atom beam with a high ground-state fraction, He gas is used as target, since the charge-exchange process is resonant:

$$He^+ + He^0\ (1^1S) \rightarrow He^0(1^1S) + He^+.$$

state	E_B
$He(1^1S)$	24.6 eV
$He(2^3S)$	4.77 eV
$He(2^1S)$	3.97 eV
$He(2^3P)$	3.63 eV
$He(2^1P)$	3.37 eV

Table 2.1: Binding energy E_B of He states with principal quantum numbers $n \leq 2$ [48].

The binding energy of the five lowest HeI levels are given in table 2.1. For the production of He-atom beams with high metastable fractions, targets with ionization energies close to the binding energies of the metastable levels $He(2^1S)$ and $He(2^3S)$ are advantageous. This is the case for alkalines. The binding energies of the valence electrons of ground-state Cs, Li, K, and Na and the corresponding energy defects for charge exchange into metastable

element	E_B	$\Delta E(2^1\mathrm{S})$	$\Delta E(2^3\mathrm{S})$
Cs	3.89 eV	**0.08**	0.88
K	4.34 eV	**-0.37**	0.43
Na	5.14 eV	-1.17	**-0.37**
Li	5.39 eV	-1.42	-0.62

Table 2.2: Binding energy E_B of the valence electrons of ground-state Cs, Li, K, and Na [50] and the corresponding energy defects for charge exchange into He(2^1S) and He(2^3S), respectively.

He(2^1S) and He(2^3S), respectively, are given in table 2.2. These charge-exchange reactions are quasiresonant and take place with large cross sections [49].

The highest He(2^3S) fraction from neutralization of a He-ion beam in alkali vapour can be obtained by using Na vapour since Na shows a quite low energy defect with respect to He(2^3S) and a relatively large energy defect with respect to He(2^1S). For a rough estimate of the final population fractions of ground-state He and the two metastable states we consider the statistical weights of those He levels with binding energies comparable to those of Na, i.e. levels with principal quantum number $n = 2$. The possible values for the total angular momentum quantum number J of a particle determined by its spin quantum number S and orbital momentum quantum number L are given by:

$$J = L + S, L + S - 1, \ldots, |L - S|. \tag{2.2}$$

The statistical weight of a state specified by J is thus given by

$$\sum (2\,J + 1). \tag{2.3}$$

Table 2.3 shows S, L, J, and statistical weight for all He($n = 2$) states. If we neglect the probability of populating both ground state ($E_B = 24.6$ eV) and higher excited levels ($E_B \leq 1.86$ eV) due to their large energy defects with respect to ground-state Na, and if we additionally consider the four $n = 2$ levels as giving rise approximately to the same energy defect, we find population fractions F as shown in the last column of table 2.3.

level	S	L	J	$\sum(2J+1)$	F
He(2^3S)	1	0	1	3	18.75%
He(2^1S)	0	0	0	1	6.25%
He(2^3P)	1	1	0,1,2	9	56.25%
He(2^1P)	0	1	1	3	18.75%

Table 2.3: Spin- (S), orbital momentum- (L), total angular momentum quantum number (J), statistical weight $\sum(2J+1)$ for He states with principal quantum number $n = 2$ and the resulting population fractions F, see text.

The decay time of the 2^1P state into the ground state is approximately 0.6 ns with a branching ratio of 99.9% and 0.1 μs into the metastable 2^1S state for the remaining 0.1%. This results in a final population structure after relaxation of the excited levels:

$$75\%\ 2^3\text{S},\ 6.25\%\ 2^1\text{S},\ \text{and}\ 18.75\%\ 1^1\text{S}.$$

Since the energy defect for charge exchange from Na into He(2^3S) is much smaller than into any other level, the population fraction of the 2^3S level is even higher than estimated [51, 52].

The above consideration is only valid for thin targets without further collisions after the charge-changing process. In a thick target the neutralized particle will encounter further collisions and the population of metastable- and ground state can be rearranged. As spin-changing collisions have much smaller cross sections than spin-conserving collisions [53], an atom exited from He(2^3S) is likely to stay in the triplet system and decay back into He(2^3S) leaving the population of He(2^3S) unchanged. A particle excited from the He(2^1S) will predominantly decay into the ground state. For He(3^1P) the branching ratio is for example 97.6% into He(1^1S) and 2.4% into He(2^1S). Hence, in a thick target the metastable singlet state is likely to be quenched into the ground state by excitation processes.

Another attenuation mechanism for the metastable states is ionization. Respective cross sections are in general larger than excitation cross sections for collisions between fast metastable He atoms and gas atoms [54]. Ionization processes lead to a higher ground-state fraction in the beam since ionization cross sections for He(2^3S) and He(2^1S) are much larger than for ground state He [54]. In addition, high ionization cross sections for metastable He atoms also demand low residual gas pressure.

2.1.2 Beam Characterization

In the next chapter a survey of different techniques for measuring the metastable fraction in atomic and ionic beams is given. Chapter 2.1.2.2 describes the technique used at IAP.

2.1.2.1 Methods for Determination of Metastable Beam Fractions

Several techniques have been developed to measure the metastable fraction in atomic and ionic beams, e.g.:

- time-of-flight method,
- laser atom-absorption spectroscopy,
- laser-induced fluorescence,
- beam attenuation method,
- optical attenuation method, and
- grazing incidence method.

Time-of-flight method

Energy conservation requires that in a charge-changing collision the difference in binding energy of the electron before and after the collision will affect the kinetic energy of the collision partners. He atoms in the metastable state after the collision will therefore have a different kinetic energy than those in the ground state. Particles of a sufficiently short beam pulse will therefore separate while passing from the neutralization cell to the detector where they are registered. E.g., Reynaud *et al.* [51] determined the metastable fractions of 1^1S, 2^1S, and 2^3S in He beams ($E \leq 1.5$ keV) after neutralization of He-ion beams in Na, K, Cs, and Rb vapor. Prerequisites for this technique are beams with small energy spread and particle detection systems with high energy resolution.

Laser atom-absorption spectroscopy

A laser beam is attenuated when passing through the particle beam. As the absorption is related to the beam particle density, absorption measurements yield the line-integrated population density of the metastable atoms [55]:

$$\int n(x)dx = \frac{4\,\epsilon_o\, m_e\, c}{F\, e^2} \int ln\left(\frac{S_A(\lambda)}{S_0(\lambda)}\right) d\lambda\,, \tag{2.4}$$

where $n(x)$ stands for the metastable-population density at the position x and F for the oscillator strength. $S_A(\lambda)$ and $S_0(\lambda)$ denote the wavelength (λ) dependent transmitted intensity with and without sample, respectively. Christmann *et al.* [55] analysed energetic He beams produced by neutralization of He ions in Li vapor using the $2^3S \rightarrow 2^3P$ transition at 1083 nm to measure the He(2^3S) fraction.

Laser-induced fluorescence

Here, the beam is irradiated by laser light and the resulting fluorescence of the beam particles is registered. The wavelength of the laser light has to correspond to an allowed transition with the lower level being the level of interest. With this technique measurements of the 2^3S fraction in fast He beams have been performed by Dinklage [56]. The allowed transition $2^3S \rightarrow 3^3P$ was pumped. Observation of the resulting fluorescence light at 398 nm yielded the 2^3S density in the He beam.

Beam attenuation method

This technique, introduced by Gilbody *et al.* [57], is based on the substantial difference in the binding energies and, hence, ionization cross sections between ground- and metastable states. The particle beam passes through a well defined target (density n, interaction length L) and all beam atoms which are ionized are removed from the beam by an electrostatic field. With increasing target thickness $\Pi = n \cdot L$ the metastable population will be more and more reduced leaving only ground-state particles for a sufficiently thick target. The beam-particle intensity $I(\Pi)$ is measured from low target thicknesses (thin target) to large target thicknesses where the metastable atoms have been completely attenuated (thick target). Plotting $\ln I(\Pi)/\ln I(0)$ against target thickness gives a decaying curve. In the first section representing the thin target the intensity shows a linear decay which is dominated by the attenuation of the metastable levels which defines the slope of the curve. For increasing target density the metastable fraction becomes too small to contribute to the intensity. Consequently, the slope of the curve changes and becomes linear again for thick targets, where the attenuation of the ground state atoms defines the slope of the curve. From the slopes and the intercepts of these linear segments the ionization cross sections of the ground state, σ_{01}, and of the metastable states, σ_{m1} (both 2^1S and 2^3S), and the metastable fraction f can be derived.

The drawback of this method is that it does not discriminate between He(2^1S) and He(2^3S) due to the small difference of their binding energies. Furthermore, secondary processes influence the measured metastable fraction. Collisions with the target atoms not only result

in ionization but also de-excitation of the beam particles. Since these atoms are not removed from the beam by the electrostatic field, the measured fraction f_m of metastables is lower than the true fraction f [49]:

$$f_m = f \frac{\sigma_{m1} - \sigma_{01}}{\sigma_{m1} + \sigma_{m0} - \sigma_{01}} \tag{2.5}$$

where σ_{m0} stands for the de-excitation cross section of metastable atoms into the ground-state. This cross section has to be known since it can not be determined with this method.

Optical attenuation method (OAM)

This technique introduced by Matsumoto *et al.* [58] is based on the spectroscopic studies of Hollstein *et al.* [59] on de-excitation of He atoms involving metastable He(2^1S) and He(2^3S) atoms. In these measurements ion beams are attenuated by electron capture in suitable atomic targets. From the intensity of light emitted by the excited projectiles in the neutralization cell the electron-capture cross sections of the initial projectile levels can be deduced. Combination with AM gives the fractions in the primary-ion beam.

OAM assumes conservation of the primary ion electron configuration during electron capture from a suitable atomic target, in particular alkali atoms. If such 'core conservation' holds, radiation observed from the final excited projectile directly shows which initial levels have been involved in the capture processes. The observed transition has to be characteristic for the initial ion-beam metastable component of interest. Matsumoto *et al.* [58] utilized this technique for determining the cross sections of ground-state $Ar^{2+}(3p^4\ ^3P)$, σ_{21}, and of metastable $Ar^{2+}(3p^4\ ^1D)$, σ^*_{21}, respectively, for one-electron capture from Na. Since these two cross sections are very similar, they could not be resolved by AM alone. With the assumption of core conservation in the one-electron capture process $Ar^+(3p^4[^3P]nl)$, i.e. $Ar^+(nl)$, ions come only from ground-state $Ar^{2+}(3p^4\ ^3P)$, $Ar^+(3p^4[^1D]nl)$, i.e. $Ar^+(nl')$, ions are only produced from metastable $Ar^{2+}(3p^4\ ^1D)$. Both final states $Ar^+(nl)$ and $Ar^+(nl')$ are excited and consequently emit characteristic light with intensity $S(x)$ and $S'(x)$, respectively, at position x along the beam axis:

$$S(x) \propto (1 - f)\, I_0\, A_{nl}\, n_{Na}\, e^{-\sigma_{21} n_{Na}\, x}\,, \tag{2.6}$$

$$S'(x) \propto f\, I_0\, A_{nl'}\, n_{Na}\, e^{-\sigma^*_{21} n_{Na}\, x}\,. \tag{2.7}$$

f denotes the $Ar^{2+}(3p^4\ ^1D)$ fraction and I_0 the initial intensity of the primary-ion beam. n_{Na} is the Na target density, A_{nl} and $A_{nl'}$ the spontaneous emission coefficient of $Ar^+(nl)$

and Ar^+(nl'), respectively, σ_{21} and σ_{21}^* stand for the one-electron capture cross sections of $Ar^{2+}(3p^4\ ^3P)$ and $Ar^{2+}(3p^4\ ^1D)$, respectively. Therefore, σ_{21} and σ_{21}^* can be determined independently from the slopes of $\ln(S(x))$ and $\ln(S'(x))$ against $n_{Na}\,x$.

The Ar^{2+} ion beam attenuates as follows

$$I(L)/I_0 = (1-f)\,e^{-\sigma_{21} n_{Na}\,L} + f\,e^{-\sigma_{21}^* n_{Na}\,L}, \tag{2.8}$$

where $I(L)$ stands for the final Ar^{2+} intensity and L for the collision length. If the cross sections σ_{21} and σ_{21}^* are known from OAM measurements, the fraction of the metastable Ar^{2+} beam can be determined.

Brazuk *et al.* [61] extended the OAM to photon emission in the VUV spectral region in order to investigate electron capture in Ne^{2+}-Xe collisions and subsequently introduced a similar method utilizing **e**xcitation due to **c**ore **c**onserving electron **c**apture from alkali atoms ('X3C' method) which relies on relative measurements only [62]. The metastable fractions are derived from photon-signal ratios, which are determined for a sufficient number of beams with substantially different metastable ion-beam compositions. The X3C method has been successfully applied to beams of multiply charged ions (C^{2+}, N^{2+}, N^{3+}, and O^{4+}) from an ECR ion source as well as singly charged ions (C^+, N^+, and O^+ [63]).

Grazing incidence method

This rather new technique for analyzing fast metastable atomic beams makes use of effects of the image charge on projectile trajectories in scattering of fast beams on surfaces under grazing angles of incidence. Hecht *et al.* [60] analysed fast He beams on Al (111) surfaces. Metastable He atoms approaching the surface are ionized at about 14 a.u. distance to the surface. Consequently they are deflected and gain energy due to the image-charge force. When the distance to the surface has decreased to about 2 a.u., these He ions undergo Auger neutralization and are reflected from the surface as ground-state He atoms, but with a larger angle of reflection than the initial angle of incidence. Since ground-state He atoms are not ionized when approaching the surface, they are not affected by image forces and their angle of reflection equals the angle of incidence. Hence, ground-state- and metastable atoms are spatially separated during the scattering process. Detection of the beam densities of the separated beam components behind the surface yields the metastable fraction. The difficulties of this technique lie in the preparation of target and beam, i.e. the target surfaces have to be perfectly flat and the beam has to be well collimated.

2.1.2.2 Determination of the He Metastable Beam Fraction at IAP

The technique for measuring the metastable fraction of fast He-beams utilized during this work is similar to the optical attenuation method, but in contrast to the experiments by groups like Matsumoto *et al.* [58] and Brazuk *et al.* [61, 62], we base our measurements on excitation rather than electron capture.

In collisions between fast He beams and a target gas, excited projectile- and target atoms are produced. The intensity of the spontaneous emission from these excited states is proportional to their population density. Cross sections are particularly large for quasiresonant reactions. In a quasiresonant reaction the energy difference for the transition of the target atom matches closely the energy difference for the transition of the projectile. This is the case for excitation-transfer collisions between metastable He atoms and Ne, as utilized in the He-Ne laser. Figure 2.1 gives the energy-level diagrams of HeI- and NeI levels involved in excitation-transfer collisions between metastable He and ground-state Ne. For easier notation the levels Ne($1s^2\,2s^2\,2p^5$ nl) and Ne($1s^2\,2s^2\,2p^5$ nl') are summarized as Ne(nl,nl'). In quasiresonant excitation-transfer collisions between He(2^1S) and ground-state Ne the He atom is de-excited into the ground state. Its energy is transferred to the Ne atom, which is excited to Ne(5s,5s') and consequently decays to Ne(3p,3p'). In the case of quasiresonant excitation-transfer collisions between He(2^3S) and ground-state Ne the latter is excited into Ne(4s,4s'), which is followed by spontaneous emission to Ne(3p,3p') and consequently to Ne(3s,3s'). Finally, Ne(3s,3s') decays into Ne ground state.

A multitude of lines in a large wavelength range are emitted during these spontaneous emission processes due to the multiplicity of the Ne levels involved. The transition Ne(5s,5s') $\rightarrow$ Ne(3p,3p'), which is a measure for the initial He(2^1S) population, emits light at wavelengths between 543 nm and 773 nm. One of these emission lines, i.e. the 632.8 nm emission, is well known from He-Ne lasers. Emission lines of Ne(3p,3p') $\rightarrow$ Ne(3s,3s'), which are a measure for the total metastable He population (2^1S and 2^3S), occur between 540 nm and 808 nm. Hence, the two wavelength regions of Ne(5s,5s') $\rightarrow$ Ne(3p,3p') and Ne(3p,3p') $\rightarrow$ Ne(3s,3s') overlap. Table 2.4 shows emission lines of both transitions in the wavelength region between 625 nm and 641 nm.

From the measurements of Huber [65] using the same experimental setup we conclude that the emitted spectrum in the vicinity of 633 nm is dominated by the Ne(3p,3p') $\rightarrow$ Ne(3s,3s') transition (figure 2.2), as only the lines displayed in the right column of table 2.4 (e.g. 630.5 nm and 633.4 nm) are visible. The contribution from excitation transfer out

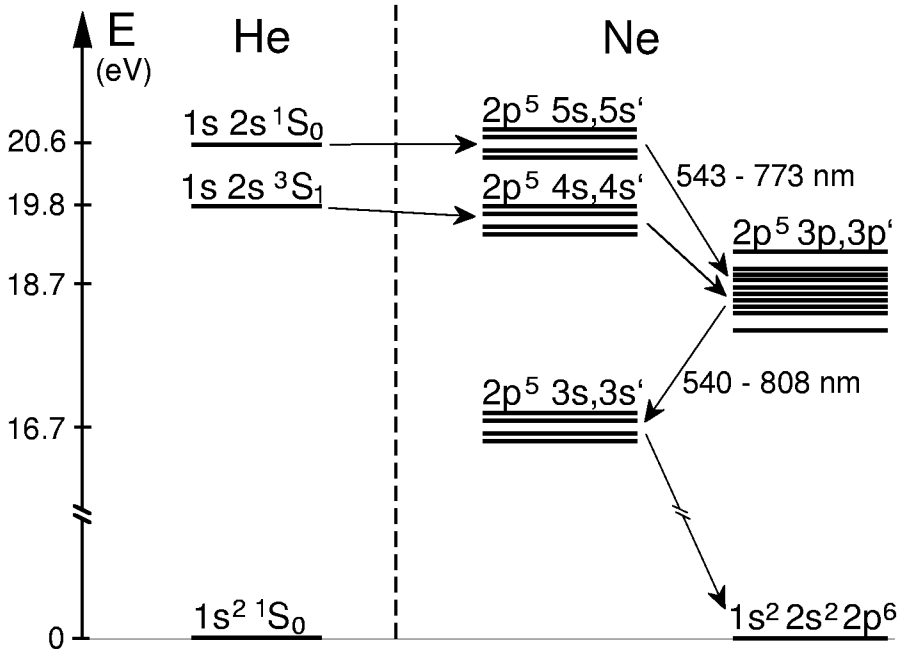

Figure 2.1: Energy levels involved in excitation-transfer collisions between metastable He atoms and ground-state Ne atoms and subsequent spontaneous emission of Ne.

Ne(5s,5s') → Ne(3p,3p')	Ne(3p,3p') → Ne(3s,3s')
629.4 nm	626.6 nm
631.4 nm	630.5 nm
632.8 nm	633.4 nm
633.1 nm	638.3 nm
635.2 nm	640.2 nm
636.5 nm	
640.1 nm	

Table 2.4: Wavelengths of transitions occurring during Ne(5s,5s') → Ne(3p,3p') and Ne(3p,3p') → Ne(3s,3s') spontaneous emission in the region between 625 nm and 641 nm [64].

of the 2^1S state, which yields lines displayed in the left column of table 2.4, were below our detection limit. Obviously the 2^1S state had already been efficiently quenched by residual gas atom collisions as mentioned in chapter 2.1.1. Consequently, the intensity of light observed with a 633 nm interference filter (see chapter 2.2.4) is a measure for the He(2^3S) population density.

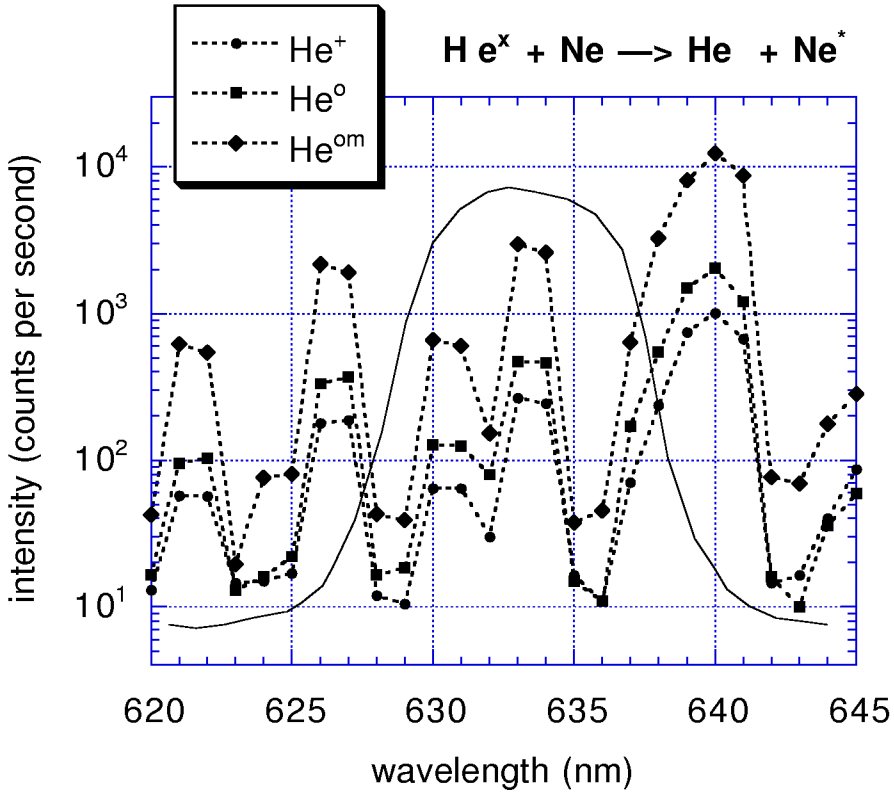

Figure 2.2: Emission spectrum of 10 keV He beams of different composition in Ne registered with a Czerny Turner spectrometer [65]. He^+ denotes an ion beam, He^o and He^{om} indicate He beams neutralized in He gas or Na vapour, respectively. Additionally, the transmission of the 633 nm interference filter used for the measurements presented in chapter 2.3 is shown (solid line).

Another process leading to a rather strong emission, characteristic for the initial $He(2^3S)$ population, is the excitation process $He(2^3S) \rightarrow He(3^3P)$. $He(3^3P)$ decays back to $He(2^3S)$ emitting at 389 nm. As the cross section for spin-changing collisions are negligibly small compared to spin-conserving collisions, the line intensity at 389 nm can be assumed to originate from $He(2^3S)$ only. Hence, the emission intensity observed at this wavelength can also be used as a measure for the initial $He(2^3S)$ fraction.

Several possibilities for determination of f have been suggested and discussed by Huber [65], e.g.:

- singlet/triplet He line-intensity ratios, e.g. 389 nm/502 nm,
- Ne line-intensity ratios,
- He/Ne line ratios,
- changes in intensity due to variation of beam composition.

As the 502 nm ($3^1P \rightarrow 2^1S$) emission is too weak, the first suggestion failed. Some other singlet and triplet emission lines exhibit sufficient intensity, e.g. 588 nm ($3^3D \rightarrow 2^3P$) and 668 nm ($3^1D \rightarrow 2^1P$). Prerequisite for determination of f is the knowledge of the corresponding excitation cross sections for collisions between He (ground state and 2^3S) and ground state Ne. Unfortunately, the relevant cross section databases (e.g. [54]) are not sufficiently complete.

Determination of f using Ne line-intensity ratios is problematic due to the multiplicity of the levels. To use only one line each for characterization of singlet or triplet metastables is not suitable as the relevant cross sections are not sufficiently well known.

Another idea was the calibration of the optical system at one characteristic wavelength (e.g. 633 nm or 389 nm) with beams exhibiting metastable fractions known from literature [49, 51, 52]. The beam composition can be adjusted by variation of the neutralization-target thickness, i.e. the product of target density and interaction length between beam and target (Na or He, see chapter 2.1.1).

In the present work, another method for determining f is introduced utilizing the variation of the beam composition with attenuation-target thickness. A collisional model has been developed for calculating the population-density progression of levels of interest during attenuation of the He beam in Ne gas. By adjusting the variable parameter f until the calculated Ne(3p,3p') $\rightarrow$ Ne(3s,3s') emission matches the measured Ne emission in the range selected by the 633 nm interference filter, the metastable fraction f of the incident beam can be deduced. A detailed description of this model is given in chapter 2.3.

2.2 Mixed He Beam Setup

The schematic view of the He-beam setup at IAP termed 'HELMA' (a composition of **hel**ium and **m**etastable **a**toms) is given in figure 2.3. A He ion beam is produced with a 2.45 GHz-ECRIS (**e**lectron **c**yclotron **r**esonance **i**on **s**ource [44, 45, 46]). By setting the ion source to high potential, He ions are extracted from the ion source and accelerated to several kV by an electrostatic accel-/decel system, and pass an electrostatic lens and a sector magnet which deflects the ions by 50° degree. The deflected monoenergetic ions pass the neutralization chamber [66, 47] either filled with Na vapour or He gas, and are removed from the beam by electrostatic deflection plates. The neutral particles enter an attenuation chamber [65] which is filled with neon gas, and are finally registered in a Faraday cup. Optical emission from

collisions between the neutral He- and the Ne-gas atoms is analysed by means of interference filters and a photomultiplier. The single parts of the setup are described in the following chapters.

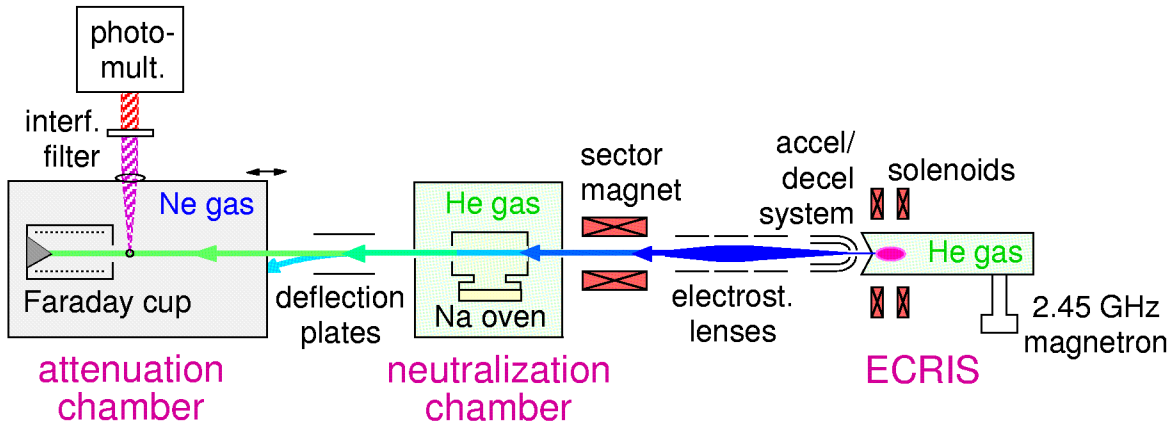

Figure 2.3: Schematic illustration of the He-beam setup HELMA.

2.2.1 2.45 GHz ECRIS

An ECRIS ion source consists of a confining magnetic field structure which also contains the resonance layer for electron-cyclotron radiation launched into the source. Electrons near the resonance region absorb the emitted radiation and are accelerated. The ions are produced in collisions of these accelerated electrons with the gas filled into the source. A detailed description of the 2.45 GHz-ECRIS at IAP can be found in [44, 46].

The plasma is trapped by the magnetic field of two solenoids positioned coaxially to the plasma tube (figure 2.3, [44, 45]). The solenoids produce a so-called magnetic mirror field $B(\vec{r})$, see figure 2.4.

Due to the invariance of the magnetic momentum μ,

$$\mu = \frac{m\, v_{\perp}^2(\vec{r})}{2\, B(\vec{r})}, \tag{2.9}$$

the charged particles with mass m are trapped in the magnetic mirror configuration depending on their velocity $v_{\perp}(\vec{r})$ perpendicular to the magnetic field $B(\vec{r})$. Increasing $B(\vec{r})$ leads to an increase in $v_{\perp}(\vec{r})$. As a result the velocity parallel to $B(\vec{r})$, $v_{\parallel}(\vec{r})$, decreases due to

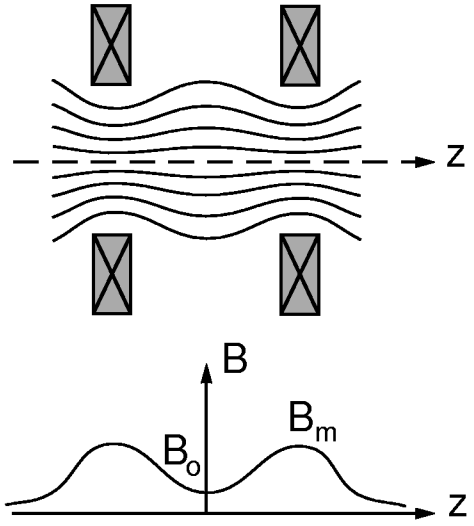

Figure 2.4: 'Minimum B' configuration generated by two solenoids positioned radially around the z-axis. Above: magnetic field lines, below: magnetic field at z-axis.

conservation of energy until becoming zero. At that position ($\vec{r}_r$), the particle velocity has only a perpendicular component, $v(\vec{r}_r) = v_\perp(\vec{r}_r)$, i.e. the particle is reflected at $\vec{r}_r$ and thus trapped in the magnetic field. Particles with $v_\parallel(z = 0) \equiv v_{\parallel o}$ above the critical velocity

$$v_{\parallel c} = \sqrt{\frac{2\,\mu}{m}(B_m - B_o)} \tag{2.10}$$

are able to escape the mirror field. B_o denotes the magnetic field at $z = 0$ and B_m the maximum magnetic field on the z-axis (see figure 2.4). In velocity space the region of the lost particles is cone shaped (so-called loss cone):

$$\left(\frac{v_{\perp o}}{v_o}\right)_c^2 = \frac{v_{\perp o}^2}{v_{\perp o}^2 + v_{\parallel c}^2} = \frac{B_o}{B_m} = sin^2\Theta_m. \tag{2.11}$$

The angle Θ_m determines the loss cone, which is equal for electrons and ions. Particle loss is determined by scattering into the loss cone predominantly due to Coulomb collisions. Electrons having a higher loss rate than ions due to their much higher collision frequency, cause a positive electrostatic potential, the so-called ambipolar potential Φ_a, which compensates for the difference in loss rates of electrons and ions.

As the magnetic field is not homogenous, the gyration frequency ω_{ce} of the electrons depends on its location in the plasma tube:

$$\omega_{ce}(r,\theta) = \frac{e\,B(r,\theta)}{m_e}. \tag{2.12}$$

r and θ denote radius and angle in cylindric coordinates. In the regions where ω_{ce} equals the microwave frequency the electrons will be accelerated. This results in a highly efficient ionization of the gas particles in that region. At 2.45 GHz this resonance occurs at a magnetic field of 87.5 mT which corresponds to a solenoid current of about 250 A in this geometry. Since the ion-gyration frequency is much lower than the electron gyration frequency ω_{ce} due to their large mass difference ($m_{He} \approx 8000\ m_e$), only the electrons are heated directly by the microwave.

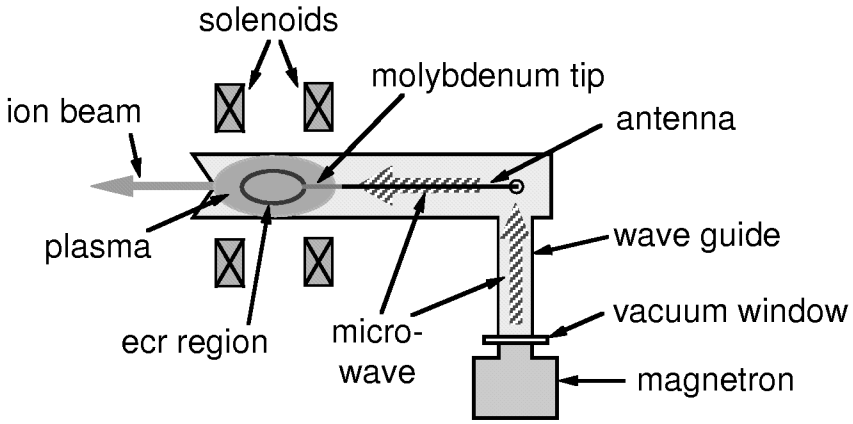

Figure 2.5: Schematic diagram of the 2.45 GHz ECRIS at IAP.

The heating microwave is generated in a water-cooled magnetron with an output power in the range of 200 W to 1.2 kW. It can be operated in continuous or pulsed mode. During the experiments conducted in this thesis the magnetron was used in continuous mode at about 300 W only. The microwave is directed via a rectangular wave guide and a 90° coupling into the cylindrical plasma tube to a coaxial molybdenum antenna [44, 45], see figure 2.5. The vacuum window in the rectangular wave guide consists of a 5 mm thick teflon plate which also serves as high voltage insulator. The antenna ends close to the ECR region. The extracted ions leave the ion source through the extraction aperture, in this case a Pierce-shaped electrode with an aperture of 3 mm diameter. The extracted current is of the order of several hundred μA.

The conductivity L_c (unit: m^3/s) for a hole with area F (unit: m^2) is given by [68]

$$L_c = 0.25\,\bar{v}\,F, \tag{2.13}$$

where $\bar{v}$ (unit: m/s) denotes the average particle velocity which for He at room temperature is $1.25{\cdot}10^3$ m/s. The conductivity of the plasma electrode is with $2.2{\cdot}10^{-3}$ m^3/s by a factor of 136 smaller than the pumping speed of the turbo pump (0.3 m^3/s) yielding a similar pressure ratio between plasma tube and extraction vessel. With a pressure in the plasma tube of about 10^{-3} mbar during operation, the pressure in the extraction vessel therefore amounts to about 10^{-5} mbar. This corresponds to a He gas density of about 10^{17} m^{-3}.

2.2.2 Beam Transport

The ion source is operated at a potential of up to +12.5 kV with respect to ground, the decel electrode is set to ground potential and the accel electrode to typically -2 kV. The ion optics is dominated by space charge and the focussing effect of electrostatic lenses. The beam trajectories can be further influenced by an electrostatic lens consisting of three cylindrical electrodes, see figure 2.3. The first and third electrodes are grounded and the second one is set to several kV. This leads to an electric field with high gradients in the gaps between the three electrodes, where the beam particles are accelerated or decelerated. As with the accel/decel system, an appropriate combination of acceleration and deceleration results in focussing of the ion beam [69].

In addition, a movable Faraday cup has been arranged in the vacuum region where the accel-/decel system and the first electrostatic lens are located. This Faraday cup is only moved into the beam path for coarse positioning of the beam, but not during routine operation of the system. Subsequently, the ion beam passes a second electrostatic lens system [70] with an inner diameter of 45 mm.

Ion beams produced from He gas in the 2.45 GHz ECRIS of IAP consist not only of He^+ but also contain unwanted beam components (He^{2+}, H^+ and H_2^+), as can be seen in figure 2.6. These components are eliminated by the 50° sector magnet. In the magnetic field of a sector magnet the beam particles are selected due to their mass/charge ratio. As no other beam particles with a mass/charge value similar to that of He^+ are expected in the beam, the He^+ beam can be considered as pure after passing the sector magnet.

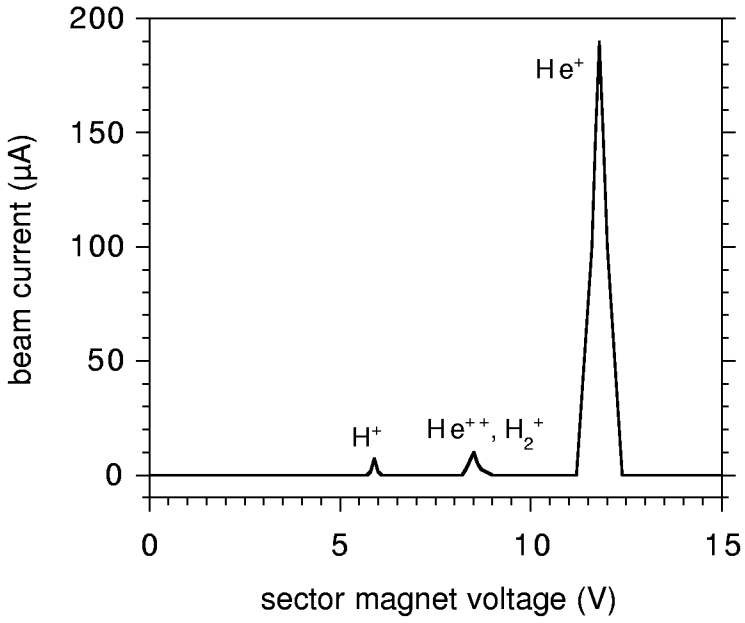

Figure 2.6: Ion beam spectrum taken after the sector magnet for a 12.5 keV He beam. Magnet settings are indicated by the voltage of the power supply.

2.2.3 Neutralization Chamber

The He-ion beam has been neutralized in either He gas or Na vapour. If He gas is used for charge-exchange, the resulting He-beam atoms are predominantly in ground state. Neutralization in Na leads to a He-atom beam with a considerable He(2^3S) fraction, see chapter 2.1.1.

The Na-vapour cell displayed in figure 2.7 has been made available to IAP by IPP Garching [71] and has been adapted to the HELMA setup in several ways [66, 47]. It consists of a cylindrical tube with 120 mm length and an inner diameter of 24 mm. In its center there is an opening to the Na reservoir mounted beneath. This opening can be closed by a plug mechanism from outside the vessel via a feedthrough, see figure 2.7. If the Na reservoir is closed, the ion beam can still pass the then empty tube of the Na-vapour cell. This is important for neutralization in He gas only.

In order to heat the neutralization tube and the Na reservoir, a thermocoax wire with 1 mm outer diameter is wrapped around them. It consists of an inner conductor with a resistivity of 12.5 Ω/m and an outer stainless steel tube isolated by ceramic powder. The temperature can be measured by four thermocouples, three at the tube and one at the reservoir. The vapour

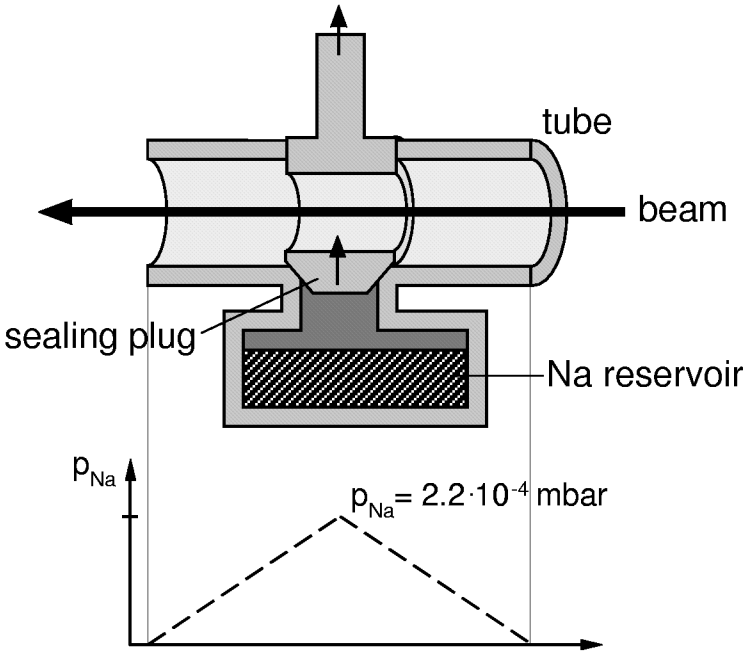

Figure 2.7: Schematic diagram of the Na-vapour cell at HELMA. Also shown is the Na-pressure distribution inside the tube for estimation of single collision condition, see text.

cell is heated to 200°C which corresponds to a Na-vapour pressure of $2.2{\cdot}10^{-4}$ mbar [50], i.e. a density of $3.4 \cdot 10^{18}$ particles per m^3. At this temperature, the Na in the oven is in liquid state (melting point 98°C [50]). The neutralization cell is located in the neutralization chamber (figure 2.3) which is pumped by a turbomolecular pump with 0.26 m^3/s pumping speed for He. A residual He-gas pressure of $3{\cdot}10^{-7}$ mbar could be achieved. This corresponds to a density of $7{\cdot}10^{15}$ He atoms per m^3, i.e. about 1/500 of the Na density. Hence, the probability for He-He collisions can be neglected compared to He-Na collisions.

Conflicting requirements exist for the target density in the neutralization cell. The interpretation of the measurement is most straightforward for single-collision conditions in which the target density is small enough to exclude multiple collisions between beam particles and target gas. However, the neutral fraction is initially proportional to the target density and the sensitivity of the detection system can set a lower limit for the target density. In the neutralizer of neutral beam systems (e.g. neutral beam diagnostics, heating beam systems) the target density is normally optimized towards the highest possible neutral beam flux. In our measurements the conditions were set as follows.

The probability P for collisions with cross section σ is given by

$$P = \sigma \int_0^L n_T(l)\, dl, \tag{2.14}$$

where n_T denotes the target density, l the line parameter along the beam path and L the interaction length. As a reasonable approach for single-collision conditions, P should be smaller than 10%.

The largest cross section for rearrangement of ground state- and metastable population fractions is ionization out of the metastable states. For collisions of 10 keV He(2^3S) in Na this cross section is smaller than $5{\cdot}10^{-20}$ m^2 [72]. Additionally, we assume a Na density distribution along the beam path as indicated in figure 2.7. This leads to a value for P of less than 0.01, which means that the chance for a He(2^3S) particle to become neutralized by a second collision with Na is smaller than 1%.

For using He gas as neutralizer, the neutralization chamber is filled with He gas through a precision valve on top of the charge-exchange vacuum vessel. The gas pressure can be measured by an ionization gauge. The neutralization chamber is closed off by two apertures with a diameter of 15 mm, and the distance between the two apertures is about 0.3 m. The cross section for charge exchange between 10 keV He ions and thermal He atoms is $6.1{\cdot}10^{-20}$ m^2 [73]. For the experiments presented in chapter 2.3, a He pressure of $3{\cdot}10^{-4}$ mbar was chosen, corresponding to a 15% chance for a He ion to be neutralized. A collision between two He atoms leads most likely to excitation into He(2^3S) ($\sigma \approx 10^{-20}$ m^2 [54]). Hence, the probability for an already neutralized He beam particle to get excited by a second collision with a He-gas atom is only 2%.

In the following vacuum vessel after the neutralization chamber an additional Faraday cup is located which can be moved into the beam if needed. The remaining ions are removed from the beam by a set of deflection plates.

2.2.4 Attenuation Chamber for Determination of the He Beam Composition

In this chamber, attenuation of the He beam in Ne gas is analysed by detecting the NeI emission at 633 nm and the HeI emission at 389 nm. Additionally, the beam particle flux is monitored by a specially designed neutral particle Faraday cup [67]. A detailed description of the attenuation chamber can be found in [65].

A schematic illustration of the attenuation chamber is given in figure 2.8. The chamber was filled with Ne gas via a needle valve. The beam passes the pre-chamber and enters the attenuation chamber through a 2 mm diameter aperture adjustable in beam direction. Its position determines the interaction length L of the beam in the gas target after which the beam reaches the observation position of the optical system and the Faraday cup. The attenuation chamber is connected with the pre-chamber also via a bypass which can be valved off. The pre-chamber is pumped with a 0.33 m^3/s turbomolecular pump. If the bypass valve is open, the residual gas pressure inside the attenuation chamber is less than 10^{-7} mbar. If the bypass valve is closed, the resulting pressure rises to about $5{\cdot}10^{-5}$ mbar while the He beam is on.

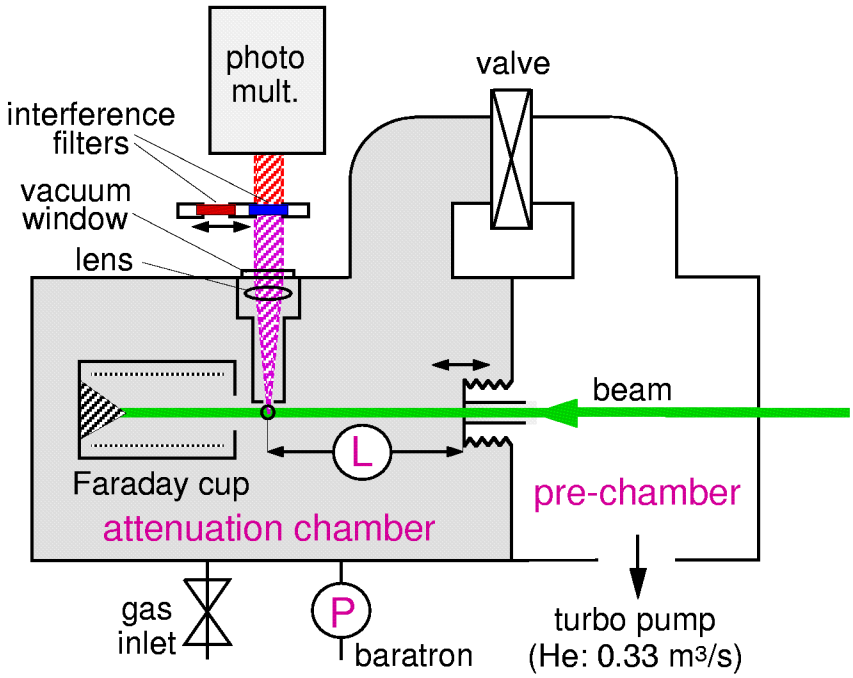

Figure 2.8: Schematic diagram of the attenuation chamber at HELMA.

Light emitted by the excited He- and Ne atoms reaches the photomultiplier via an optical system which consists of the following elements:

plano-convex lens	(Schott, 150 mm focal length, 90% transmission for 380 nm to 700 nm)
vacuum window	(borofloat quartz plate, Stölzle Oberglas, transmission $\geq$ 93% above 380 nm)
narrow-band interference filters	(Melles Griot 18F/I3900 10MK: 390 $\pm$ 4.5 nm, Melles Griot 03FIL026: 633 $\pm$ 5 nm, located in a moveable filter cassette)
photomultiplier	(EMI 9816B, 22% sensitivity at 380 nm, 8% sensitivity at 650 nm; Peltier-cooled)

The photomultiplier output is routed through a preamplifier, discriminator and to the LAB NB-card of the data acquisition system described in chapter 2.2.5. A hollow cylinder with a variable slit opening (0 to 3 mm) towards the beam was located between vacuum window and beam in order to narrow down the observed beam path region. In this way, a beam-path region of about 4 mm is imaged. The interference filters could easily be changed by shifting it within the filter cassette.

Assuming proportionality between the intensity S_{633} of the 633 nm emission and the He(2^3S) population, S_{633} is given by

$$S_{633} \propto n_{Ne}\, e^{-\sigma_m\, n_{Ne}\, L}, \tag{2.15}$$

where σ_m stands for the quenching cross section of He(2^3S) in Ne gas (density n_{Ne}), and L denotes the interaction length. In order to vary the target thickness $n_{Ne} \cdot L$, either the Ne pressure or the position of the beam entrance aperture (see figure 2.8) could be varied. The aperture can be moved with a stepper motor (dual stepper motor drive SMD2, Arun Microelectronics Ltd.) which is located outside the chamber. This motor is controlled by the LabVIEW program described in chapter 2.2.5. The gas pressure inside the chamber is measured with a baratron (MKS 627).

The beam was analysed with a specially designed Faraday cup [67] mounted behind the observation position. With this Faraday cup not only ion-beam currents but also the flux

of neutral beam particles can be measured. This 'neutral particle Faraday cup' (NPFC) is shown in figure 2.9.

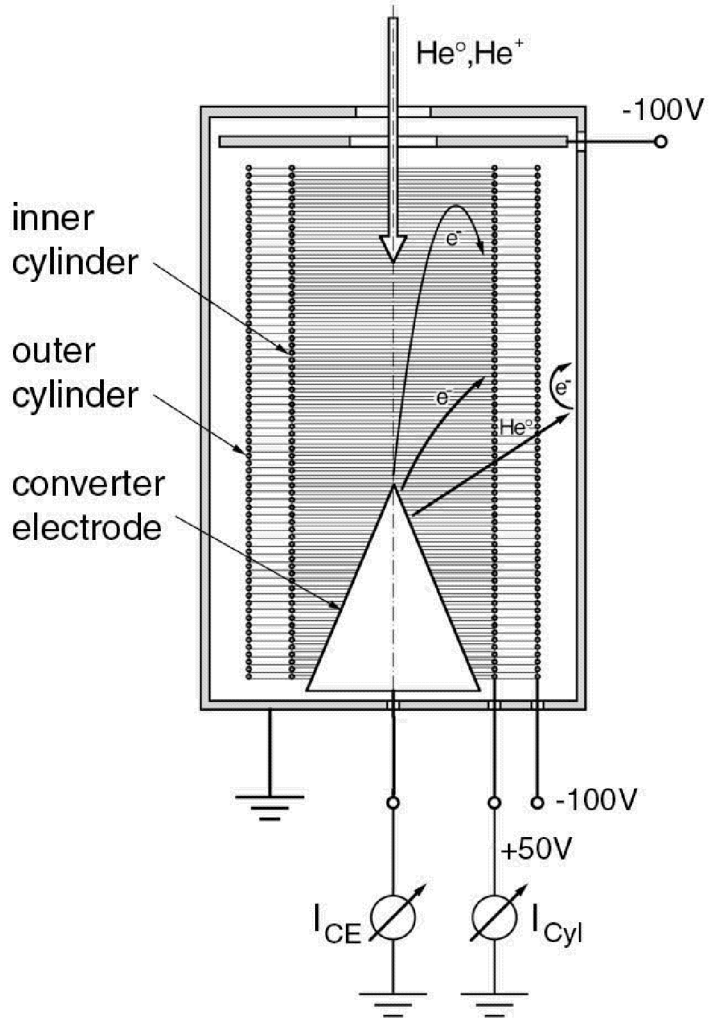

Figure 2.9: Schematic diagram of the NPFC at HELMA.

The Faraday cup consists of a grounded stainless steel housing. The beam enters the cup through a drilling (7 mm diameter) at the top, passes a negatively biased repeller electrode and hits the converter electrode made of stainless steel, which is surrounded by two cylinders made from wire mesh with 92% transparency. The inner cylinder acts as anode for secondary electrons released from the converter electrode by impact of beam particles. The outer cylinder is biased negatively and acts as reflector for the electrons passing through the anode mesh and also prevents secondary electrons from the housing wall to reach the anode.

In case of an incident beam consisting of both ions (current I_+) and atoms (equivalent current

I_o), the current at the converter electrode, I_{CE}, is given by

$$I_{CE} = I_+ + \gamma\,(I_+ + I_o)\,, \tag{2.16}$$

and the current at the inner cylinder, I_{Cyl}, by

$$I_{Cyl} = \gamma\,(I_+ + I_o)\,, \tag{2.17}$$

where γ denotes the electron-emission yield of the converter electrode, i.e. number of electrons emitted per incident beam particle. For a pure neutral beam, the neutral beam equivalent current I_o can be deduced by measuring the current I_{CE} at the converter electrode:

$$I_{CE} = \gamma\, I_o\,, \tag{2.18}$$

if γ is known. In principle, γ can be determined from a single measurement with a pure ion beam. But no ion beam with a negligible atom fraction could be produced due to neutralization of He^+ in the residual gas. Hence, γ was determined with two measurements, the first one with a beam consisting of ions and atoms and the second one with a pure atomic beam. At the beam energies used (several keV) potential electron emission is much weaker than kinetic electron emission [74]. Therefore, γ is assumed to be the same for He ions and atoms. From the measurements with on the one hand a beam consisting of ions and atoms ($I_{CE,1}$, $I_{Cyl,1}$) and on the other hand with a pure atomic beam ($I_{CE,2} = I_{Cyl,2}$), we get

$$\gamma = \frac{I_{Cyl,1} - I_{CE,2}}{I_{CE,1} - I_{Cyl,1}}\,. \tag{2.19}$$

During operation at room temperature, a time-dependent change of γ was observed [65]. This effect can be explained by adsorption of atoms and molecules (e.g. Na, H_20) on the converter surface. In order to reduce this adsorption to an acceptable value, the converter electrode is heated to 200°C. This is achieved by a thermocoax heater wrapped around a ceramic cylinder inside a hole drilled into the back side of the converter. Figure 2.10 shows experimentally deduced γ values for He beam energies between 3 keV and 12 keV.

The currents at cylinder, I_{Cyl}, and converter electrode, I_{CE}, are measured simultaneously with two picoamperemeters (Keithley 480), by which means the neutral particle flux I_o and the ion current I_+ can be deduced:

$$I_o = I_{Cyl}\,\frac{1+\gamma}{\gamma} - I_{CE}\,, \tag{2.20}$$

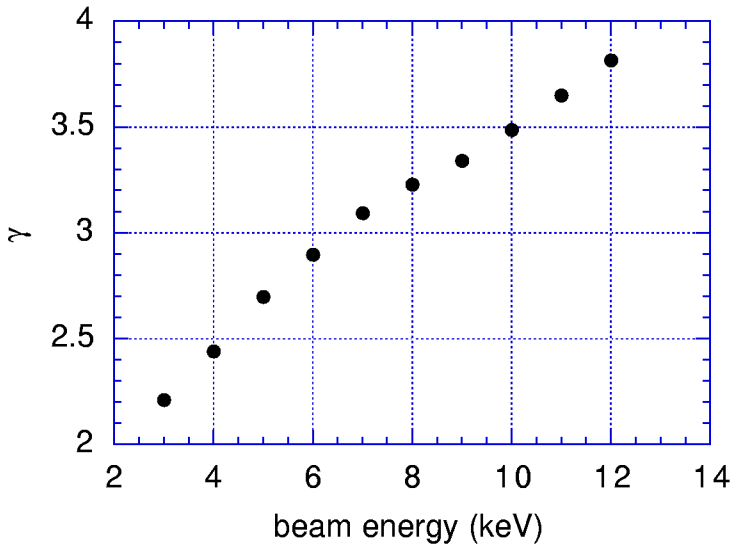

Figure 2.10: Experimentally deduced γ values for He atoms hitting the converter electrode of the NPFC [67].

$$I_+ = I_{CE} - I_{Cyl}\,. \tag{2.21}$$

The interaction length L has to be large compared with the distance $\tau{\cdot}v$, which the particle of velocity v travels between excitation and spontaneous emission of lifetime τ. If this is not the case, the measured beam emission S_M at the location viewed by the diagnostic system is not at the equilibrium level S_{LT}. To get the equilibrium level the measured quantity has to be corrected by the the following expression [75]:

$$S_{LT} = S_M\, F_{LT} = S_M \left(1 - \frac{\tau\, v}{\Delta L}\, e^{\frac{L}{\tau\, v}} \left(1 - e^{\frac{\Delta L}{\tau\, v}}\right)\right)\,. \tag{2.22}$$

ΔL stands for the extension of the observed beam path area. The lifetime of the considered HeI emission line at 389 nm amounts to $1.05{\cdot}10^{-7}$ s. Figure 2.11 shows F_{LT} values for this emission for three different beam energies.

2.2.5 Experiment Control and Data acquisition

The position of the aperture leading to the attenuation chamber and the data acquisition are computer controlled. This is done by an interactive LabVIEW program called 'current/counter/stepper' which controls a LAB NB-card (National Instruments Inc.).

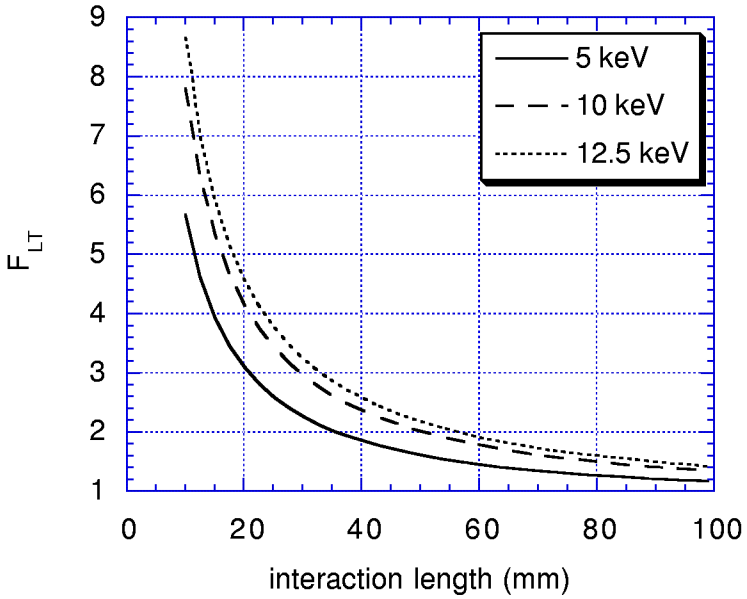

Figure 2.11: Lifetime correction factor F_{LT} of the 389 nm emission vs. interaction length of the beam in the target gas for three different beam energies.

The program reads photomultiplier counts and both cylinder- and converter-electrode current from the two picoamperemeters. For a better handling of beam-current fluctuations, the photomultiplier signal is normalized to the beam equivalent current. This is done by simultaneous integration of both the photomultiplier counting rate R_{PM} and the current I_{Cyl} with time t, until a charge

$$C_{Cyl} = \int_{t_1}^{t_2} \frac{I_{Cyl}}{\gamma}\, dt \tag{2.23}$$

has reached a pre-specified value. Hence, the value for the integrated photomultiplier signal

$$S_M = \int_{t_1}^{t_2} R_{PM}\, dt - R_B\,(t_2 - t_1) \tag{2.24}$$

is independent of beam-current variations. R_B denotes the photomultiplier background counting rate which is also determined with the program. The program can handle up to $6.5{\cdot}10^4$ counts per second and currents up to 2 mA.

Additionally, the program controls the movement of the aperture stepper motor. Parameters like direction of movement, distance for each step, and velocity of the movement can be chosen. It is also possible to move the aperture directly to a pre-defined position.

The output file contains the charge C_{Cyl}, last reading of cylinder- ($I_{Cyl}(t_2)$) and converter-electrode current ($I_{CE}(t_2)$), time elapsed during measurement ($t_2 - t_1$), and background-subtracted photomultiplier signal S_M.

An additional program can be used for calculating the electron yield γ by evaluation of I_{Cyl} and I_{CE} data for both pure neutral beams and beams containing neutrals and ions as described in chapter 2.2.4.

2.3 Results and Discussion

Neutral He beams in the energy range between 5 keV and 12.5 keV have been produced from He^+ ion beams passed through the neutralization chamber either filled with pure He gas ($3{\cdot}10^{-4}$ mbar) or with Na vapour from the vapour cell (200°C oven temperature). The beam neutralized in He gas consists predominantly of ground-state atoms (He^0), while the beam neutralized in Na contains a considerable fraction of metastable He atoms and will be called He^m- or mixed beam. He-ion beams in the energy range between 5 keV and 12.5 keV have been produced. The attenuation chamber was filled with Ne and the pressure was varied between $1{\cdot}10^{-4}$ and $1{\cdot}10^{-2}$ mbar. The location of the aperture of the attenuation chamber, which defines the interaction length, was chosen at 43 mm in front of the volume from which the beam emission was analyzed. The emission at 633 nm (NeI) and 389 nm (HeI) were measured. The photomultiplier signals were summed up until the charge C_{Cyl} in the neutral-particle Faraday cup reached 90 μC. The measured photomultiplier signals were lifetime- and background corrected as described in chapter 2.2.4. Examples from He^0- and He^m beams with three different beam energies are given in figures 2.12 and 2.13. As expected, the intensity of both emission lines is quite different for beams with low and high 2^3S fraction and could indeed be used to measure the metastable triplet fraction as proposed by [65]. Furthermore, the 633 nm emission yields about twice as much photomultiplier counts as the 389 nm emission.

Quantitative analysis of the 2^3S fraction has been done by comparing the experimental 633 nm intensity with that from a newly developed model, i.e. a simple 3-level model for calculating the He beam attenuation during collisions with Ne atoms and the resulting NeI emission at 633 nm. Figure 2.14 shows the transitions between He(1^1S), He(2^3S), and He^+ levels which are included in our simplified model. The corresponding collisions and cross sections are given in table 2.5.

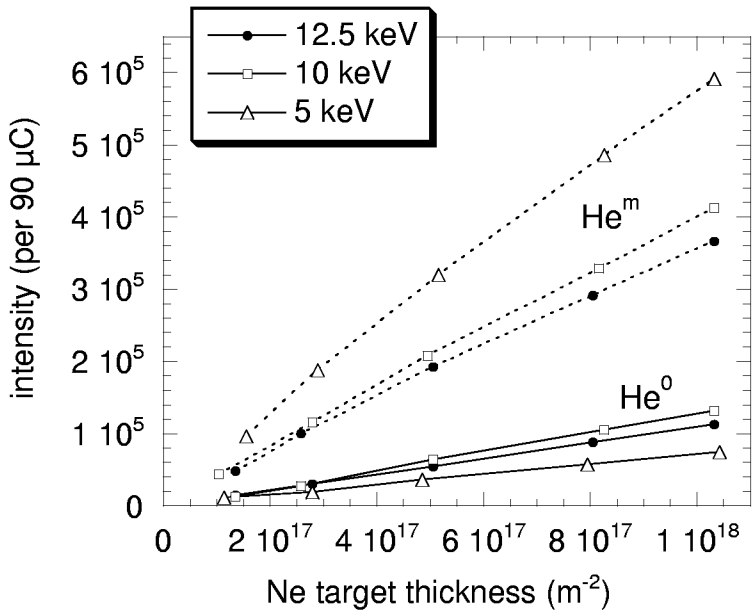

Figure 2.12: Photomultiplier signal (per 90 μC at the inner cylinder) versus Ne-gas thickness ($\hat{=}$ $1{\cdot}10^{-4}$ - $1{\cdot}10^{-3}$ mbar) using a HeI 389 nm filter for a He^+ beam neutralized in He gas (He^0) or Na vapour (He^m).

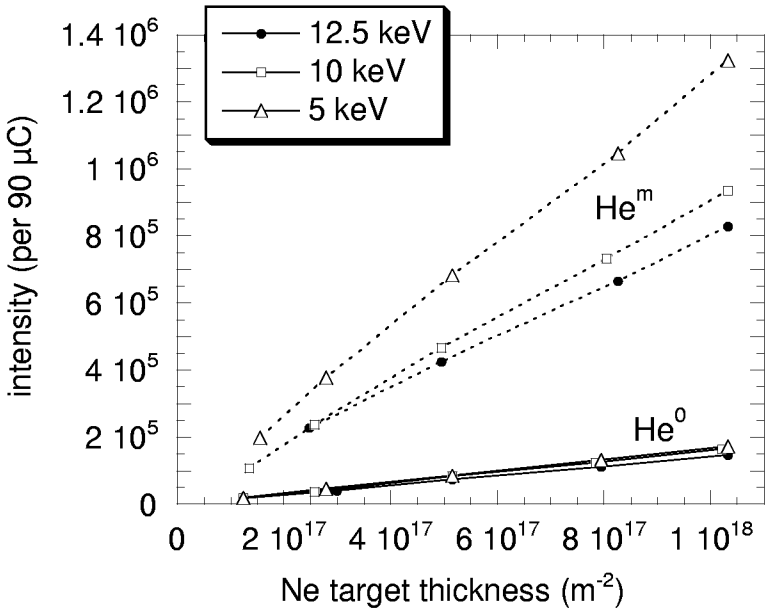

Figure 2.13: Photomultiplier signal (per 90 μC at the inner cylinder) versus Ne-gas thickness ($\hat{=}$ $1{\cdot}10^{-4}$ - $1{\cdot}10^{-3}$ mbar) using a NeI 633 nm filter for a He^+ beam neutralized in He gas (He^0) or Na vapour (He^m).

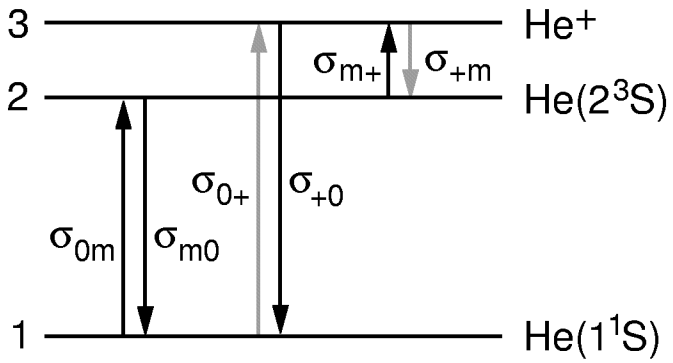

Figure 2.14: Levels and transitions included in the 3-level model for He-Ne collisions. Also displayed are the corresponding cross sections. The grey arrows mark the transitions which can be neglected due to their small cross section.

collisional process	cross section at 10 keV
$He(1^1S) + Ne \rightarrow He(2^3S) + Ne$	σ_{0m}
$He(2^3S) + Ne \rightarrow He(1^1S) + Ne(4s,4s')$	$\sigma_{m0} \approx 9{\cdot}10^{-20}$ m^2 [72, 76]
$He(2^3S) + Ne \rightarrow He^+ + Ne + e^-$	$\sigma_{m+} = 1.8{\cdot}10^{-21}$ m^2 [77]
$He^+ + Ne \rightarrow He(2^3S) + Ne^+$	$\sigma_{+m} \ll 10^{-20}$ m^2 [75, 73]
$He(1^1S) + Ne \rightarrow He^+ + Ne + e^-$	$\sigma_{0+} \ll 10^{-20}$ m^2 [72]
$He^+ + Ne \rightarrow He(1^1S) + Ne^+$	$\sigma_{+0} = 7.55{\cdot}10^{-20}$ m^2 [73, 78]

Table 2.5: Collisions included in the He-Ne model and cross sections at 10 keV as far as known from literature.

Some of the cross sections could either be found in literature in the wrong energy range only (σ_{m0}, σ_{+m}, and σ_{0+}), or could not be found at all (σ_{0m}). Only the values for σ_{m+} and σ_{+0} are given in the literature in the here considered energy range [77, 73, 78]. The cross section for the excitation transfer process, σ_{m0}, was found for lower (thermal He beams [76]) and higher ($\geq$ 50 keV [72]) beam energies and was estimated to be close to that of the thermal He beam, i.e. $9{\cdot}10^{-20}$ m^2. From extrapolation of the values for σ_{+m} [75, 73] and σ_{0+} [72] to the considered energy range, they have been assumed as negligibly small compared to the cross sections of the reverse processes. σ_{0m} was used as a free parameter in the modelling with the limitation of being small compared to the reverse collision cross section σ_{m0} since the latter is a resonant process. Hence, the balance equations for the three levels can be written as:

$$
\begin{aligned}
\frac{dn_{He(1^1S)}}{dx} &= n_{Ne}\left[-n_{He(1^1S)}(x)\,\sigma_{0m} + n_{He(2^3S)}(x)\,\sigma_{m0} + n_{He^+}(x)\,\sigma_{+0}\right] \\
\frac{dn_{He(2^3S)}}{dx} &= n_{Ne}\left[n_{He(1^1S)}(x)\,\sigma_{0m} - n_{He(2^3S)}(x)\,(\sigma_{m0} + \sigma_{m+})\right] \\
\frac{dn_{He^+}}{dx} &= n_{Ne}\left[n_{He(2^3S)}(x)\,\sigma_{m+} - n_{He^+}(x)\,\sigma_{+0}\right]
\end{aligned}
\tag{2.25}
$$

A mathematica code was developed in order to solve these balance equations and calculate the normalized intensity of the NeI 633 nm line given by

$$
\frac{S_{633}(x)}{n_{Ne}} \propto n_{He(2^3S)}(x)\,\sigma_{m0} + n_{He(1^1S)}\,\sigma_{0*}\,, \tag{2.26}
$$

where σ_{0*} denotes the cross section for the excitation reaction

$$
\mathrm{He}(1^1\mathrm{S}) + \mathrm{Ne} \rightarrow \mathrm{He}(1^1\mathrm{S}) + \mathrm{Ne}(4\mathrm{s},4\mathrm{s}'),
$$

which is assumed to be much smaller than σ_{m0}. This cross section could not be found in the literature either and, hence, it is used as free parameter in the modelling. The third free parameter is the He(2^3S) fraction

$$
f = \frac{n_{He(2^3S)}}{n_{beam}} = \frac{n_{He(2^3S)}}{n_{He(1^1S)} + n_{He(2^3S)}}, \tag{2.27}
$$

where n_{beam} stands for the total density of the beam atoms.

The calculations have been performed by attenuation of 10 keV He beams with two different He-beam compositions (He^0 and He^m) in Ne gas up to a pressure of $1{\cdot}10^{-2}$ mbar, where already multiple collisions occur which are included in the model. The measurement results given in figure 2.15 show a slightly increasing normalized intensity for the He^0 beam which consists mainly of ground-state atoms, and a rapidly decreasing one for the He^m beam with a high He(2^3S) fraction f. This can be qualitatively explained by an increase in the metastable fraction for the He^0 beam (more He(2^3S) produced than destroyed) whereas in the case of the He^m beam the destruction rate for He(2^3S) is larger than the production rate. As expected, the emitted normalized intensities of both beams have to converge to the same value for sufficiently thick targets. The calculation results exhibit the same attenuation behaviour as the measurements, which can be seen in figure 2.16.

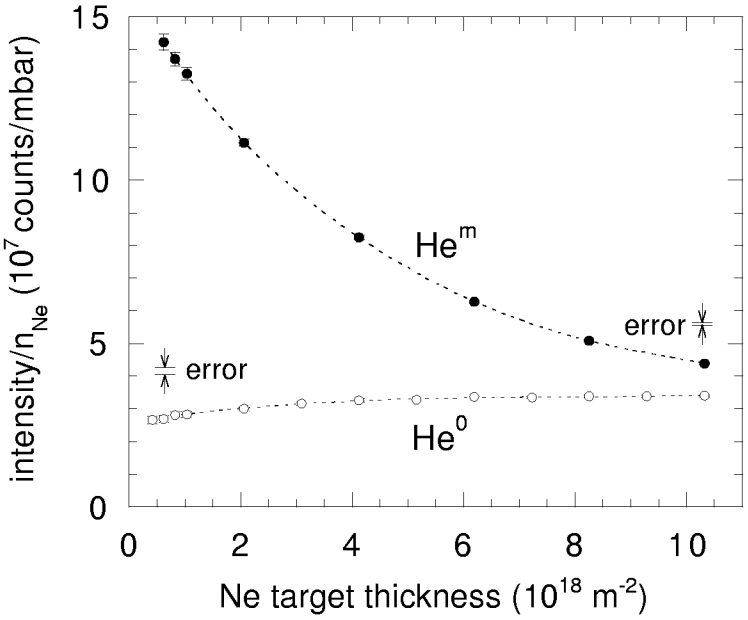

Figure 2.15: Normalized 633 nm emission of a 10 keV He beam neutralized either in Na vapour (He^m) or in He gas (He^0) vs. target thickness derived from measurement. The errors decrease with increasing target thickness as indicated in the figure. The dashed line is a polynomial fit.

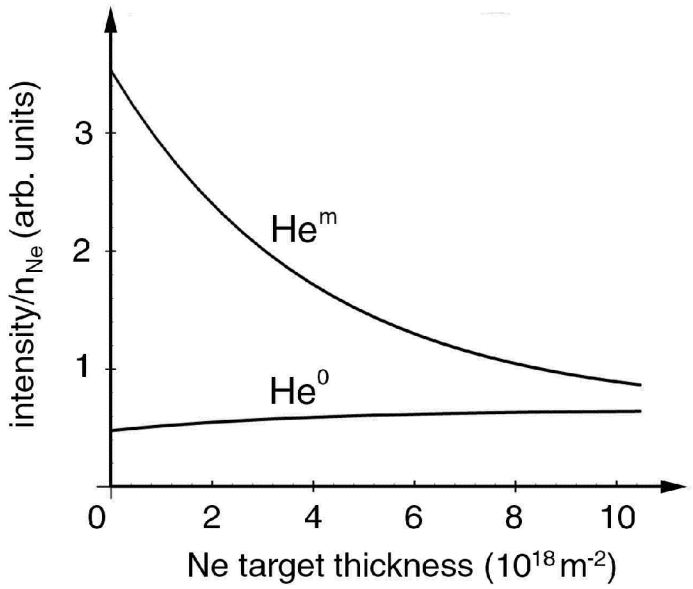

Figure 2.16: Progression of the normalized 633 nm emission calculated with the 3-level He-Ne model for a 10 keV He beam with either 80% (He^m) or 3% (He^0) metastable triplet fraction vs. target thickness.

The free parameters f, σ_{0m}, and σ_{0*} were optimized so that the shape of the normalized 633 nm intensity vs. target thickness for both He^m- and He^0 beam fitted the corresponding calculated curves. A reasonable match could be achieved for the following values of the cross sections:

$$\sigma_{0m} \approx \sigma_{0*} \approx 8{\cdot}10^{-21}\ \mathrm{m}^2.$$

The resulting values for the metastable triplet fractions are:

$$f(He^m) \approx 0.80, \text{ and}$$

$$f(He^0) \approx 0.03,$$

i.e. about 80% of the He^m-beam atoms and about 3% of the He^0-beam atoms are in metastable triplet state when entering the attenuation chamber. As mentioned above the exact value of f depends on the values of the cross sections used for the modelling. The considered values have been obtained with reasonable assumptions for the cross sections and have to be regarded as approximate.

From these measurements and calculations it can be concluded that with the He-beam setup HELMA we are able to produce He-atom beams with high metastable triplet fractions of up to about 80%. Furthermore, it is in principle possible to determine the triplet metastable fraction by comparing the measured and modelled beam attenuation. However, the cross-section database would have to be extended for a more precise evaluation. For the characterization of these mixed beams the emission at 633 nm is suitable for monitoring the metastable triplet fraction.

Chapter 3

Modelling of He Diagnostic Beams

3.1 Introduction

During the last years, fast lithium beam diagnostics has become a well established tool for determining electron density profiles (Li-IXS, Li impact excitation spectroscopy [2, 3]) and impurity ion temperature- and density profiles (Li-CXS, Li charge-exchange spectroscopy [2, 79]) of fusion edge plasmas. For such diagnostic measurements, a fast Li beam of several 10 keV energy and some mA equivalent current is injected into the fusion plasma. The electron spin configuration of neutral Li is doublet only, and the ionization energy is 5.39 eV. The excitation- and ionization rate coefficients of Li show only a weak dependence on the temperature in the temperature region of diagnostic interest (see figure 3.1), and furthermore, the ratio of these rate coefficients is almost independent of the electron temperature. Hence, the population densities of the ground state and excited levels can simply be determined by measuring one Li emission line along the beam path and solving the balance equations for all states involved. The model includes levels for up to n = 4, whereas higher levels can be neglected. The observed Li line is 670 nm (2p→2s) as the most intense one. The derived information about the population densities of ground state and excited states makes it possible to reconstruct the electron density profile by inverting the balance equations (Li-IXS [29, 80, 81]). In Li-CXS measurements the injected Li atoms act as electron donors for the impurity ions. Generally, the electrons are captured into excited states of the ions which subsequently emit photons. From the intensities of these lines the ion densities can be deduced. The full width at half maximum of the emission lines gives access to the ion temperature [30].

The atomic features of neutral He are somewhat different from neutral Li. Helium occurs

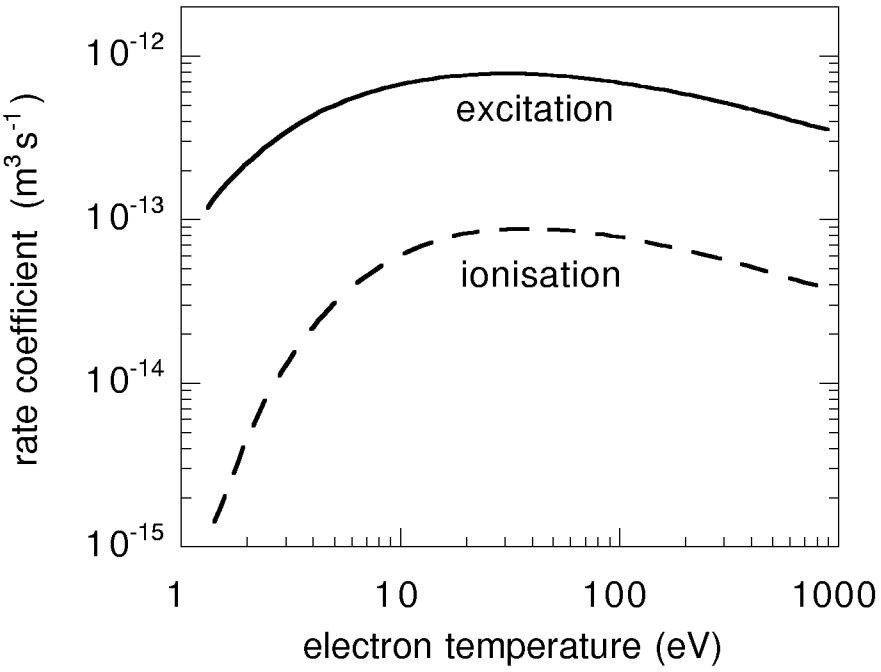

Figure 3.1: LiI rate coefficients for excitation from ground state to the lowest excited state (2p, solid line) and for ionization of the ground state (dashed line) [82].

in two different spin systems, namely singlet (i.e., $S = \sum s_i = 0$, the spins of the two electrons are antiparallel) and triplet (i.e., $S = \sum s_i = 1$, the two electron spins are parallel). Furthermore, two excited He states are metastable (the binding-energy level diagram of He is shown in figure 3.2). Helium has the largest ground state ionization energy of all atoms, 24.6 eV. Hence, a He beam should penetrate into a plasma much further than a Li beam of the same energy. Consequently the diagnostic region could be extended into the plasma core by using a He beam instead of a Li beam. The ionization energy of the two metastable levels 2^1S and 2^3S is 3.97 eV and 4.77 eV, respectively, which is in the order of the ionization energy of the Li ground state. This fact suggests using of He beams for charge-exchange spectroscopy also, where the metastable levels should act as electron donors for the impurity ions. This feature raises the question whether a high initial metastable fraction in the beam would be favourable.

An additional advantage of He beams compared with Li beams is based on the fact that He occurs in two different spin systems. The triplet system can only be populated by spin-changing processes, i.e. electron collisions, whereas the singlet metastable and other excited states are mainly populated by spin-conserving processes from the ground state. The different behaviour of cross sections for spin-changing and spin-conserving collisions leads to a rather different temperature dependence of the excitation rate coefficients, see

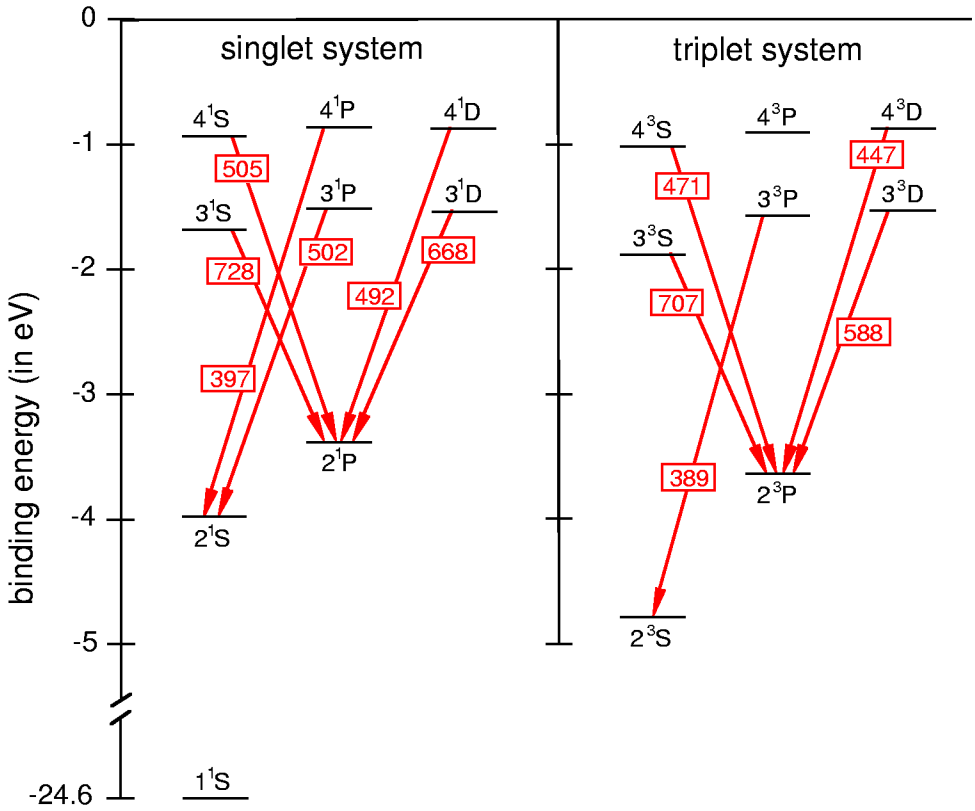

Figure 3.2: Binding energy level diagram of He including the states with n $\leq$ 4 and l $\leq$ 3, and optical lines of present diagnostic interest.

figures 3.3 to 3.5. For the electron-impact excitation out of the ground state (figure 3.3) the difference between spin-conserving and spin-changing processes becomes apparent for electron temperatures exceeding 20 eV. The spin-conserving processes have a rather flat maximum at several 100 eV and can be considered as almost constant in the region between 50 eV and 10 keV. The maximum of the rate coefficients for spin-changing collisions out of the ground state is at about 30 eV and at higher energies they decrease approximately with T_e^{-2}. In figures 3.4 and 3.5 excitation rate coefficients are shown out of the metastable triplet and singlet state, respectively. As expected, all the maxima are displaced toward lower temperatures compared with ground state excitation. The curves for the spin-conserving processes out of metastable states are much flatter than those out of the ground state, i.e. the temperature dependence is much smaller than for excitation out of the ground state, especially in the low temperature region. The spin-changing rate coefficients start to fall on the low temperature side at about 10 eV. In figure 3.4 also the excitation from the metastable triplet to the metastable singlet state is shown. It is about 10 times larger than excitation into the $(n = 3)$-singlet levels.

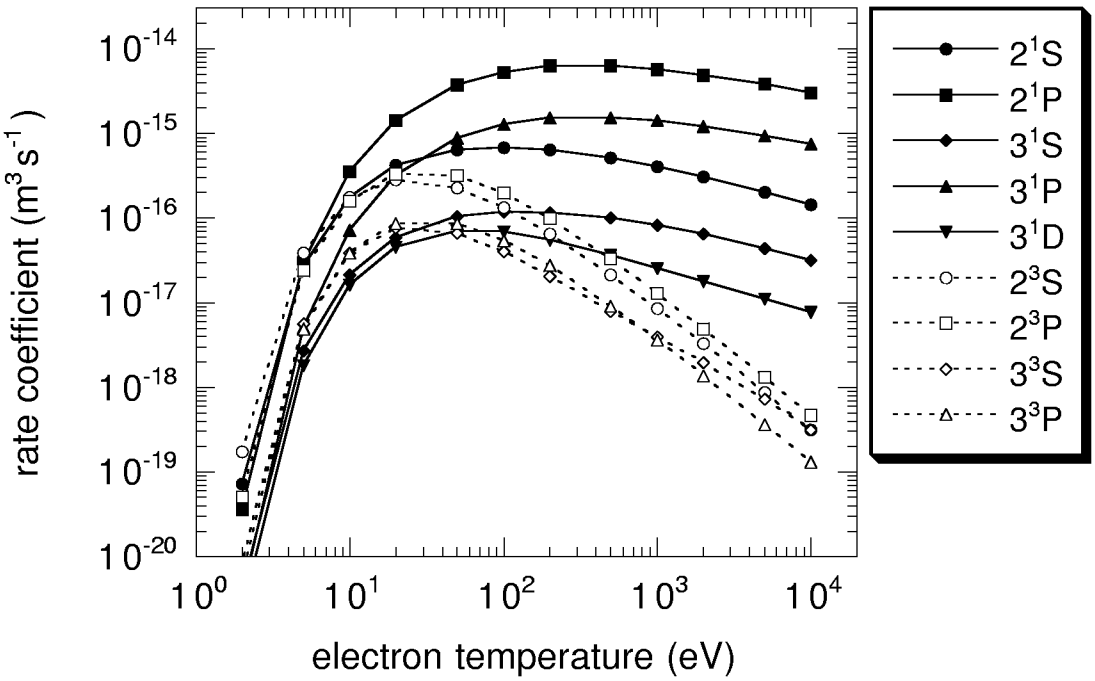

Figure 3.3: Electron temperature dependence of electron impact rate coefficients for excitation out of the He ground state into the two metastable levels and several excited levels [1].

Therefore, injection of neutral helium beams into the plasma should make it possible to determine as plasma parameters not only the electron density, ion density and -temperature, but also the electron temperature.

Extensive modelling has already been done for thermal He beams [33, 36]. Brosda [33] developed a collisional radiative model called HE-BEAM which calculates the population density profiles of a thermal He beam injected into a fusion plasma. At these beam energies the ion collisions can be neglected as the corresponding electron collision cross sections are much larger. For illustration, the cross sections for electron loss and excitation from ground state due to electron and ion impact are shown in figures 3.6 and 3.7. As the slow He beam is fully ionized in the plasma edge, the electron temperature range of interest is from about 1 eV to several 100 eV. Therefore, only electron induced de-/excitation, ionization and spontaneous decay are considered in the model.

As an advantage of the thermal He beam, modelling can be carried out in a rather simple way, but the diagnostic range of plasmas, which is comparable as for fast Li beams, is limited to the plasma edge. The first version of HE-BEAM took into account all levels up to the principal quantum number $n = 4$ (19 levels).

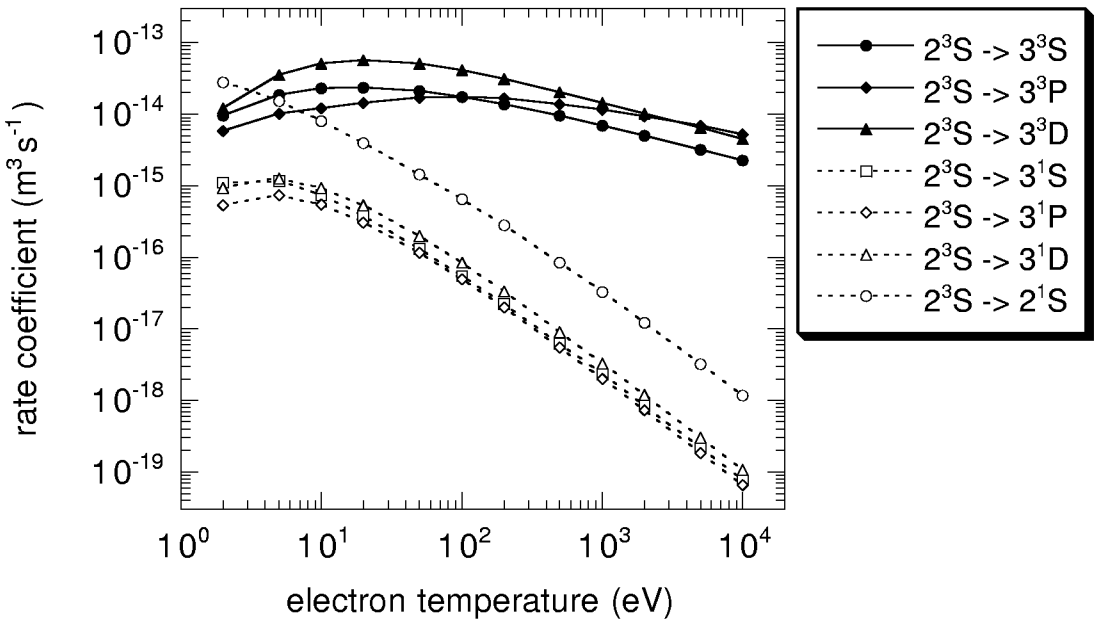

Figure 3.4: Electron temperature dependence of electron impact rate coefficients for excitation out of the metastable triplet He state into several excited levels (n=3) [1].

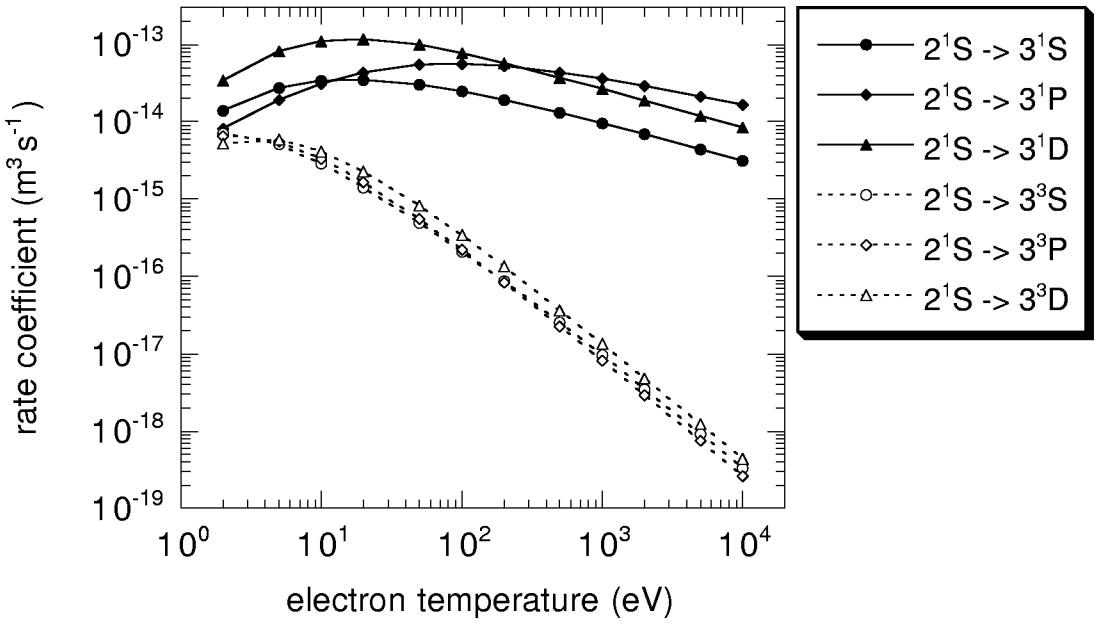

Figure 3.5: Electron temperature dependence of electron impact rate coefficients for excitation out of the metastable singlet He state into several excited levels (n=3) [1].

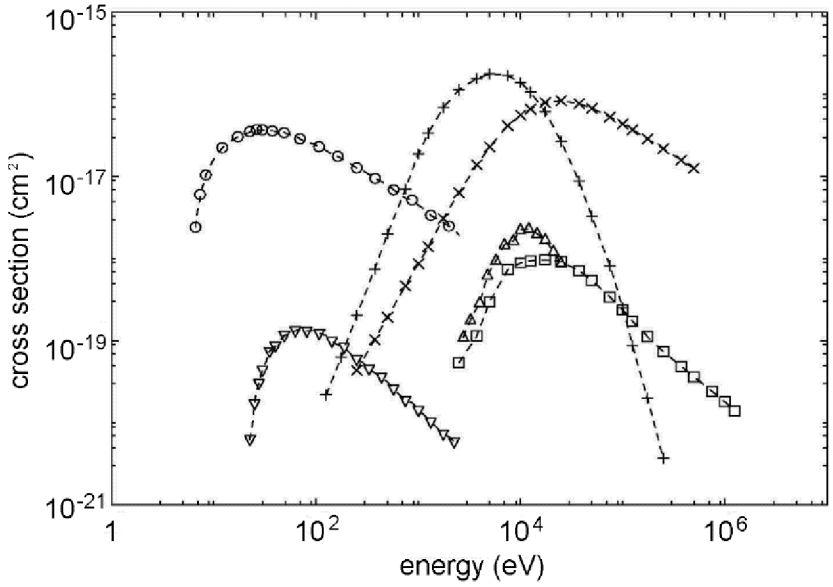

Figure 3.6: Cross sections for electron loss from ground-state He atoms, ∘: single electron impact ionization, △: double electron impact ionization, +: single charge exchange with protons, ×: single proton impact ionization, ▽: proton impact transfer double ionization, □: double proton impact ionization [43].

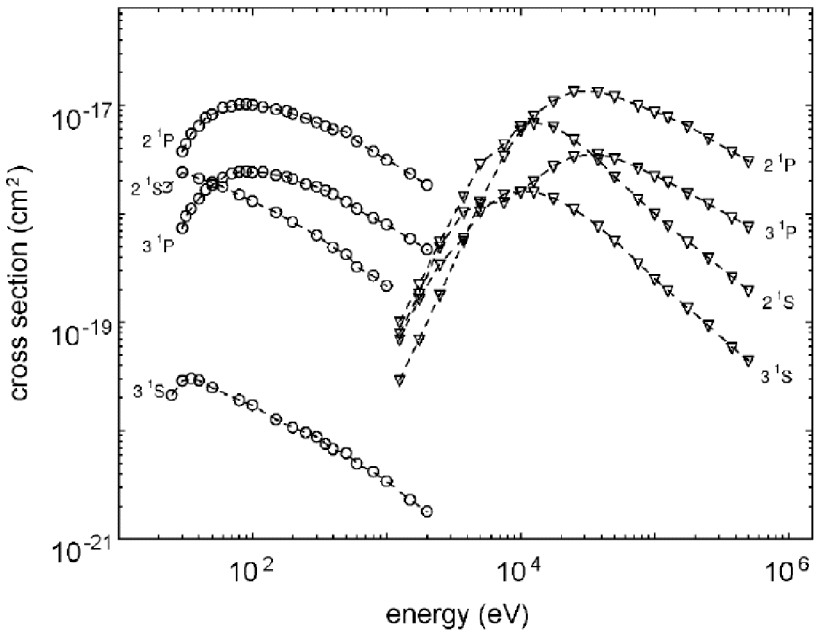

Figure 3.7: Cross sections for electron (∘) and proton (▽) impact excitation from ground-state He atoms into four low excited singlet states [43].

The evaluation routine for determining the plasma parameters from the observed line profiles is based on the fact, that for these slow beam energies the decay length for perturbations in the population of the beam is small compared to the length over which the plasma parameters change significantly. Hence, the excited states are referred to as 'totally relaxed'. From the solution for these totally relaxed excited- and metastable states, line-intensity ratios were determined which are a measure for electron density and -temperature, respectively. All lines considered in the present work except the 505 nm- ($4^1S \rightarrow 2^1P$) and 397 nm- ($4^1P \rightarrow 2^1S$) line were analysed.

Using a line-intensity ratio bears the advantage that no calibration with regard to the geometry of the beam and spectroscopic system has to be performed. The ratios 728 nm/707 nm (singlet/triplet) and 668 nm/728 nm (singlet/singlet) proved to be suitable for determining electron temperature and electron density, respectively. These lines are in the wavelength region (red) where optical spectrometers have large sensitivity and the transmission is almost the same for different wavelengths in usual optical systems. Hence, the system doesn't even have to be calibrated with regard to the frequency sensitivity. Comparison with other diagnostics showed that this model is capable of determining the plasma parameter profiles in the plasma edge of TEXTOR for plasma parameters in the range 10^{18} m$^{-3} < n_e < 10^{19}$ m^{-3} and 20 eV $< T_e <$ 100 eV.

Brix [36] has improved the model by including higher excited states ($n = 5$) and updating the fundamental cross-section data used for modelling. With this the maximum electron density available for diagnostics could be increased to $2{\cdot}10^{19}$ m^{-3} and the maximum electron temperature up to 200 eV. Meanwhile the thermal He beam is used as standard diagnostics at TEXTOR.

With this diagnostic method the plasma parameter profiles are available right from the measurements. This is also a big advantage over Li diagnostics where a time consuming calculation has to be performed. One big problem for the application of thermal He beams at future fusion devices is the beam divergence. At these experimental devices the diagnostic equipment has to be a few meters away from the plasma edge. First experiments at JET and ASDEX Upgrade showed that this problem can be overcome with a fast He beam, see chapter 5 of this thesis. Furthermore, the diagnostics won't be confined to the plasma edge any more.

In contrast to modelling thermal He beams the collisions with ions cannot be neglected for the fast beams considered in this study (several tens of keV), see figures 3.6 and 3.7. The proton-impact excitation cross sections reach values comparable to the electron-impact

excitation for beam energies of about 10 to 30 keV. For a process with a cross section σ the corresponding rate coefficient $\langle \sigma v_r \rangle$ depends on the relative velocity v_r between projectile and target. Although v_r is much larger for collisions between electrons and He atoms than for collisions between protons and He atoms and the ion rate coefficients are accordingly smaller in comparison to the electron rate coefficients, the influence of ion collisions on the beam ionization is still quite substantial. For an illustration, the total loss rate from the He ground state is given in figure 3.8. Note that, due to its dependence on v_r, the ion collision rate coefficients used for simulation in general (see chapter 3.3) depend on the beam energy only (not on the ion temperature), whereas the electron collision rate coefficients depend strongly on the electron temperature, but not on the He beam energy.

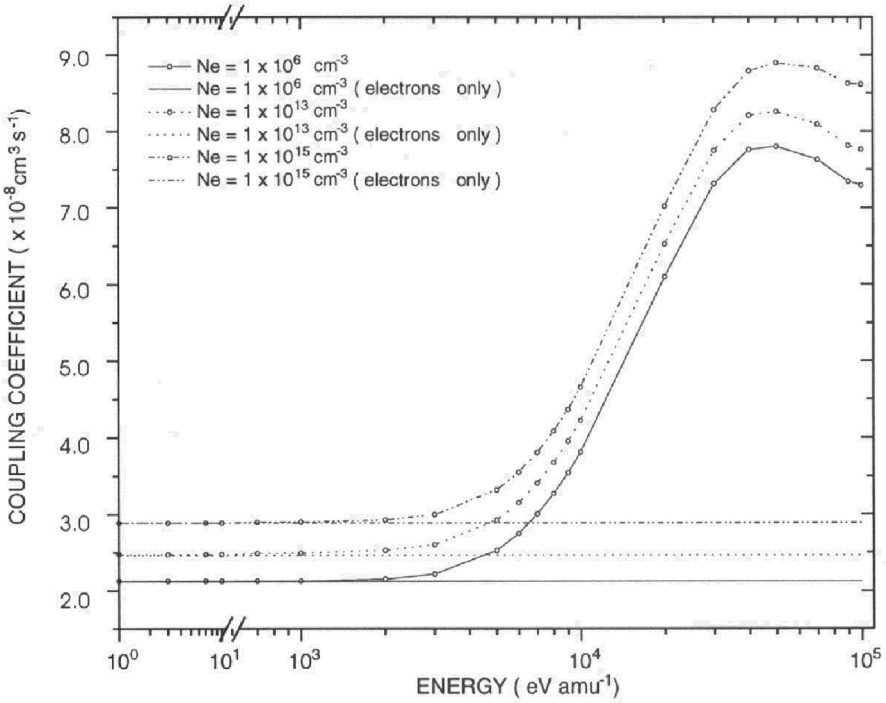

Figure 3.8: Energy dependence of the so-called 'cross-coupling coefficient' describing total loss from ground state He (S_{1^1S}, see chapter 3.3, equation 3.8) in a deuterium plasma with electron temperature of 100 eV for three different electron densities. The constant lines represent the rates when neglecting the influence of the deuterons [43].

In order to investigate the potential of fast He beams as diagnostic tools, which was the aim of this work, we have studied for typical tokamak plasmas (ASDEX Upgrade, JET):

(a) the behaviour of the ground and metastable states in a He beam penetrating the plasma,

(b) line-intensity profiles which could be of interest for diagnostic purposes,

(c) the possibility of determining electron density and -temperature profiles from line-intensity measurements

We also made first predictions on the beam intensity necessary to perform meaningful spectroscopic experiments with fast He beams at fusion devices. The possibility of using fast He beams for charge-exchange spectroscopy is outside the scope of this thesis.

In the following chapters the model used for our He beam simulation is presented. A survey of the fundamental data used for these calculations is given in chapter 3.6. Chapter 3.7 deals with different possibilities of determining the plasma parameter profiles from diagnostic measurements.

3.2 The Collisional-Radiative Model

Plasmas with densities between 10^{17} and 10^{24} m^{-3} are usually described by the so-called 'collisional-radiative model' (cr-model). The principle of the collisional-radiative model is shown in figure 3.9 for a simple atom with a ground state and two excited levels. Also the coronal model for low density plasmas and the high-density model are plotted in figure 3.9.

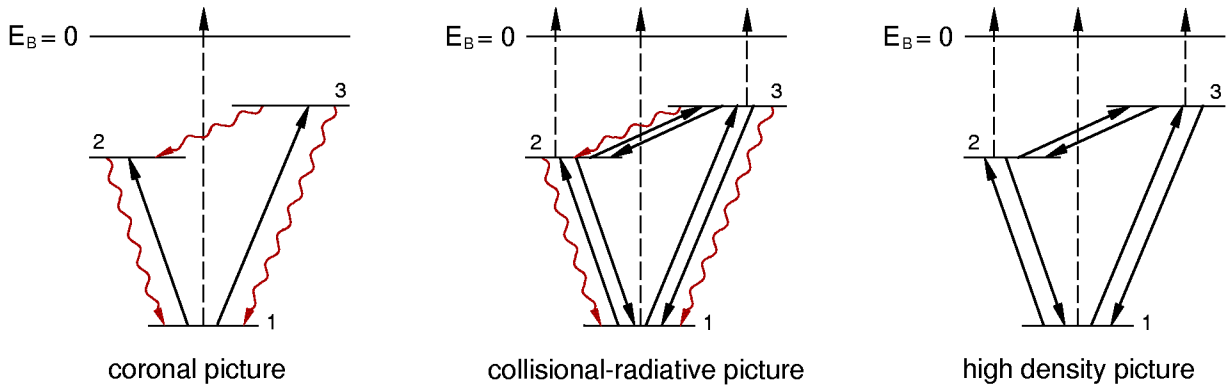

Figure 3.9: The coronal-, collisional-radiative-, and high-density model illustrated for a 3-level atom (ground state and two excited states).

In low density plasmas ($n_{plasma} \leq 10^{17}$ m^{-3}), the probability for spontaneous emission of an excited atom is much higher than for any collisional depopulation process (de-/excitation, ionization). Hence, the only processes considered are collisional excitation and ionization from the ground state and spontaneous emission. For this reason the population density of the excited states is very small in comparison to the ground state population.

In plasmas with higher density (cr-model applies), the collision frequency is higher, which leads to a competition between collisional processes and spontaneous emission. This means that in the cr-model stepwise excitation and ionization from excited states become important.

If the plasma density exceeds 10^{24} m^{-3} (high-density model applies), the collision rates have increased further until spontaneous emission can be neglected, i.e. excited states are depopulated by collisions mainly. In this case the excited states are in local thermodynamic equilibrium with the ground state.

Fusion plasmas are to be described in the cr-model as their plasma densities are in the range of 10^{17} m^{-3} to 10^{22} m^{-3}. The basis of the simulations performed during this work is the cr-model established by the ADAS-(**a**tomic **d**ata and **a**nalysis **s**tructure)[1] group at Strathclyde University in Glasgow. ADAS is a package of tools for assisting with the modelling and analysis of spectral observations of fusion and astrophysical plasmas. It consists of interactive FORTRAN routines driven by an IDL user interface and a collection of fundamental and derived atomic databases. The two ADAS codes used are ADAS311 and ADAS313, which are described in the chapters 3.3 and 3.4. A more detailed description can be found in [43]. The following processes between the beam and the plasma particles have been taken into account:

collisions between He atoms and electrons:	excitation
	de-excitation
	ionization
collisions between He atoms and ions:	excitation
	de-excitation
	ionization
	charge exchange

spontaneous emission from excited He states.

Recombination processes are neglected. The rate for recombination of He ions in the plasma is quite small. Additionally, once a beam atom is ionized it becomes trapped by the magnetic

field. These He ions are quickly removed from the beam and distributed over the respective flux surfaces. Once a particle has been trapped, it is instantly deflected and the probability to become reneutralized inside the beam region with a velocity in the direction of the beam is very small. Hence, the neglection of recombination processes is justified.

In order to solve the population density variation of the He levels of interest we consider the statistical balance equations which represent the rates at which the excited levels of an atom are populated and depopulated. In general these equations are given as:

$$\frac{\partial N_i}{\partial t} + v_b \frac{\partial N_i}{\partial x} = \sum_{j \neq i} \langle \sigma v_r \rangle_{ij,pop.} \, n_t \, N_j - \sum_{j \neq i} \langle \sigma v_r \rangle_{ji,depop.} \, n_t \, N_i + \sum_{j>i} A_{ij} \, N_j - \sum_{j<i} A_{ji} \, N_i \tag{3.1}$$

N_i and N_j denote the population densities of the levels i and j, respectively, v_b the velocity of the projectiles, $\langle \sigma v_r \rangle_{ij,pop.}$ and $\langle \sigma v_r \rangle_{ji,depop.}$ the rate coefficient of the collisional population and depopulation process, n_t the density of the target particles (in this case electrons or ions), and A_{ij} the spontaneous emission coefficient for the emission from level j to level i, respectively. The term $\frac{\partial N_i}{\partial t}$ corresponds to a change in the beam population due to variations in the beam source, but for our calculations this situation will not be considered further,

$$\frac{\partial N_i}{\partial t} = 0. \tag{3.2}$$

Taking into account all processes mentioned above, the rate coefficients for collisionally induced population and depopulation consist of the following expressions:

$$\langle \sigma v_r \rangle_{ij,pop.} = \langle \sigma_{ij,e} v_e \rangle + \langle \sigma_{ij,ion} v_{ion} \rangle, \tag{3.3}$$

$$\langle \sigma v_r \rangle_{ji,depop.} = \langle \sigma_{ji,e} v_e \rangle + \langle \sigma_{ji,ion} v_{ion} \rangle + \langle \sigma_{+i,e} v_e \rangle + \langle \sigma_{+i,ion} v_{ion} \rangle + \langle \sigma_{+i,ce} v_{ion} \rangle. \tag{3.4}$$

v_e and v_p denote the relative velocities between the beam atoms and electrons and protons, respectively. $\sigma_{ji,e}$ stand for the electron induced excitation cross sections from level i to level j, $\sigma_{+i,e}$ is the electron impact ionization cross section and $\sigma_{+i,ce}$ the charge-exchange cross section. The index ion instead of e denotes the corresponding ion impact cross sections.

The population density profile of a He beam penetrating a plasma can be determined by solving these balance equations stepwise, which can be written in matrix form:

$$v_b \frac{dN_i}{dx} = -\sum_j C_{ij} \, N_j. \tag{3.5}$$

C_{ij} is called the collisional-radiative matrix (cr-matrix), which includes all the collisional spontaneous emission contributions mentioned above. Hence, the matrix elements C_{ij} are functions of electron- and ion temperature (T_e, T_i), electron- and ion density (n_e, n_i), and beam energy (E_b):

$$C_{ij} = C_{ij}(T_e, T_i, n_e, n_i, E_b) \tag{3.6}$$

The stepwise solving of the statistical balance equation is being done by the code SCOTTIE developed at IAP, which uses the C_{ij} values calculated from ADAS311 and ADAS313.

3.3 ADAS311

In principle, the statistical balance equations (3.5) could be solved including levels up to an arbitrary principal quantum number n. But with increasing number $\tilde{n}$ of levels treated in non-equilibrium, the equation system gets more and more complex and the solving routine gets slower, as it has to deal with a rectangular matrix of the order $\tilde{n}$. The aim of the first calculations was the prediction of the progression of the He ground state and metastable population and of the expected line intensities in order to assess the favourable metastable content in the initial beam and the minimum beam intensity for first experiments at fusion experiments. For this purpose a simplified version of the cr-model was created by the ADAS-group where all excited states are treated as in equilibrium to ground state 1^1S and the two metastable states 2^1S and 2^3S. Hence, the balance equations were reduced to

$$\begin{aligned}
v_b \frac{dN_{1^1S}}{dx} &= -n_e S_{1^1S} N_{1^1S} + n_e S_{2^1S \to 1^1S} N_{2^1S} + n_e S_{2^3S \to 1^1S} N_{2^3S} \\
v_b \frac{dN_{2^1S}}{dx} &= n_e S_{1^1S \to 2^1S} N_{1^1S} - n_e S_{2^1S} N_{2^1S} + n_e S_{2^3S \to 2^1S} N_{2^3S} \\
v_b \frac{dN_{2^3S}}{dx} &= n_e S_{1^1S \to 2^3S} N_{1^1S} + n_e S_{2^1S \to 2^3S} N_{2^1S} - n_e S_{2^3S} N_{2^3S}
\end{aligned} \tag{3.7}$$

using special condensation techniques [1]. S_{N_i} denotes the total loss from level N_i, $S_{N_i \to N_j}$ stands for the excitation from level N_i to level N_j, including all stepwise processes via excited states. For assessing the progression of the three levels one has to deal only with a (3,3)-matrix. The 9 elements $S_{N_i \to N_j}$ and S_{N_i} of equation (3.8) are called 'generalized radiative coefficients' (GRCs). These GRCs are calculated from ADAS311.

The cross sections, rate coefficients, and spontaneous-emission coefficients for most of the relevant processes involving levels up to principal quantum number $n = 4$ are stored in ADAS (see chapter 3.6), whereas the remaining rate coefficients and those for higher levels are calculated via various approximative methods. The methods available in ADAS311 for the considered processes are:

electron impact excitation:	method of Van Regemorter impact parameter approximation prescription of Percival and Richards
electron impact ionization:	exchange classical impact parameter method of Burgess
ion impact excitation:	semi-empirical formula of Lodge *et al.* impact parameter method two-state approximation of Vainshtein *et al.*
ion impact ionization:	binary encounter formula of Percival and Richards

A detailed description is given in [43]. The first in each list was the method used for our calculations. The corresponding de-excitation cross sections are calculated using the principle of detailed balance.

The levels up to an adjustable level n' are considered as 'nls-resolved', i.e. levels with different principal-, orbital momentum-, and spin quantum numbers are treated as different. Levels with $n > n'$ having the same principal- and spin quantum number are merged ('ns-resolved'). In our calculations n' was chosen to be 5, the maximum principal quantum number was 110. The approximate methods listed above can be used in both pictures, in the nls-resolved picture ion and electron collisions between degenerate levels and electron-driven spin-changing collisions have to be taken into account [83].

In ADAS311 it is assumed that ions and electrons are fully equilibrated, i.e. electron temperature T_e is equal to ion temperature T_i. The velocity of protons can be neglected in comparison to the He beam velocity if

$$T_p[eV] \ll E_{beam}[eV]\sqrt{\frac{m_p}{m_{He}}} = \frac{E_{beam}[eV]}{2}. \tag{3.8}$$

During JET pulses with so called 'internal transport barriers' (modes with very high particle confinement and high temperature and density gradients, see chapter 1.1), maximum ion temperatures of about 35 keV have been measured [14]. Such high ion temperatures cannot

be neglected against beam energies of $\leq$ 80 keV any more. In order to extend the model to cases with such high ion temperatures - which will be of special importance for future plasma regimes - the code has to be modified. However, in the first experiments using fast He beams at JET and ASDEX Upgrade (see chapter 5) the ion temperature was small enough as compared to the beam energy so that the simplification $T_e = T_i$ could be applied.

The input parameters for ADAS311 concerning the plasma and beam are T_e, n_e, and E_b. For each of these parameters up to 25 values can be chosen and the code then scans through these parameters. The scans are a mixture of one- and two-dimensional scans relative to the chosen reference values T_e^{ref}, n_e^{ref}, and E_b^{ref}. In the first version of ADAS311 the output coefficients for all combinations of n_e and E_b at T_e^{ref} are calculated (two-dimensional scan in the (n_e,E_b)-plane), and then the output coefficients for the one-dimensional T_e scan at the reference values n_e^{ref} and E_b^{ref} are generated. The GRCs can be calculated for each fully stripped ion species from He^{2+} up to Ne^{10+}.

These GRCs can then be used to calculate the development of the population densities of the three non-equilibrium levels. The population densities of the excited states can be calculated by solving the corresponding balance relations (equation (3.1), $\frac{dN_i}{dt} = \frac{dN_i}{dx} = 0$) for the given parameters T_e, n_e, and E_b. Every level has a contribution from each of the 3 non-equilibrium states. ADAS311 creates special excitation coefficients [43] for the subsequent calculation of the excited population contributions performed by ADAS313 (see chapter 3.4). The output file of ADAS311 is stored in the ADAS data format adf26 [1]. It has a typical size of 7 Mb. To assist in extracting the coefficients needed for the following calculations, an interactive program (ADAS313) has been developed (see the following subchapter 3.4).

3.4 ADAS313

The line intensity I_{ji} (photons per $m^{-3}s^{-1}$) for emission from level i to level j depends on the population density N_i (m^{-3}) and the spontaneous emission coefficient A_{ji} (s^{-1}):

$$I_{ji}(T_e, n_e, E_b, N_{1^1S}, N_{2^1S}, N_{2^3S}) = N_i(T_e, n_e, E_b, N_{1^1S}, N_{2^1S}, N_{2^3S})\, A_{ji}. \tag{3.9}$$

Based on excitation coefficients generated by ADAS311, the code ADAS313 calculates for each excited level N_i of interest the so called "effective beam emission coefficients" (EECs) $E_{ji}(T_e, n_e, E_b, N_k)$ for each non-equilibrium level N_k at given values of T_e, n_e, and E_b:

$$E_{ji}(T_e, n_e, E_b, N_k) = \frac{A_{ji}\, N_i(T_e, n_e, E_b, N_k)}{n_e\, N_k(T_e, n_e, E_b)} \tag{3.10}$$

Hence, the line intensity I_{ji} can be written as

$$I_{ji} = \sum_{k=1}^{3} (E_{ji}\, n_e\, N_k) \tag{3.11}$$

ADAS313 generates the EECs for all optical emission lines of interest listed in table 3.1 and stores them in adf22 type files. As mentioned earlier, ADAS313 can also extract the GRCs, which are stored in adf21 type files. The structure of both file formats adf21 and adf22 is (like in the underlying adf26 files) the mixed two-dimensional(n_e,E_b)/one-dimensional(T_e) scan.

transition	wavelength
$4^1P \rightarrow 2^1S$	396.5 nm
$4^1D \rightarrow 2^1P$	492.2 nm
$3^1P \rightarrow 2^1S$	501.6 nm
$4^1S \rightarrow 2^1P$	504.8 nm
$3^1D \rightarrow 2^1P$	667.8 nm
$3^1S \rightarrow 2^1P$	728.1 nm
$3^3P \rightarrow 2^3S$	388.9 nm
$4^3D \rightarrow 2^3P$	447.1 nm
$4^3S \rightarrow 2^3P$	471.3 nm
$3^3D \rightarrow 2^3P$	587.6 nm
$3^3S \rightarrow 2^3P$	706.5 nm

Table 3.1: Optical lines of interest: Transitions and corresponding wavelengths.

ADAS311 and ADAS313 can also be run in a mode where ion collisions are neglected. This opens a way to estimate the influence of the ions on the beam atoms.

The first simulations have been carried out for pure electron-/deuteron plasmas ($n_e = n_p$, $Z_{eff} = 1$) with impurities neglected.

The GRCs enable for calculation of ground state and metastable level populations of the He beam on its way into the plasma for given T_e- and n_e profiles and given E_b. From these results the line intensities can be determined at each point on the beam path using the EECs. This is been done by the code SCOTTIE developed at IAP.

3.5 SCOTTIE

The code SCOTTIE [84] generates the GRCs and EECs for the plasma parameter combinations (n_e, T_e, E_b) needed for the model calculations. Then it determines the population progression of the ground state and the two metastable levels of the He beam (E_b) and the resulting line-intensity profiles for the optical lines of interest (see table 3.1) for given T_e- and n_e profiles by using the GRCs and EECs as provided by ADAS313. The code requires the following input parameters:

beam parameters:	initial population densities (1^1S, 2^1S, 2^3S)
	equivalent beam current
	beam energy
	beam diameter
plasma parameters:	T_e profiles
	n_e profiles
model parameters:	path length
	number of steps for calculation.

The code exists in two forms, one with exponentially increasing T_e- and n_e profiles with distance x and a second one with the T_e- and n_e profiles considered as linearly dependent on x. The first one is used for the calculations in the scrape-off layer, i.e. the region outside the separatrix (last closed flux surface) where the density and temperature values decay rapidly with decay lengths of about 1 cm to 3 cm. The input parameters used are the plasma values at the separatrix (T_e^S, n_e^S) and the corresponding decay lengths (λ_T, λ_n). The second version is applied for the region inside the separatrix where the plasma is divided into sections with plasma parameters treated as linearly varying with distance x. Here the input parameters are the initial and final T_e and n_e, respectively.

After reading the input file, SCOTTIE calculates the (T_e,n_e)-pairs for each calculation step. As in general the GRCs and EECs needed for one calculation step do not explicitly appear in the corresponding ADAS file, SCOTTIE has to interpolate the GRCs and EECs in the (n_e, E_b) plane and then to interpolate in the T_e dimension. The interpolation in T_e- and E_b direction has been done linearly, whereas the interpolation in the n_e direction has been performed logarithmically [43]. Afterwards the change in the population densities of 1^1S, 2^1S, and 2^3S is determined by solving equation 3.8 stepwise. Then at each calculation step

the intensity of each line of interest is calculated using equation 3.11. The single results are stored in tables prepared for plotting in spread sheets.

3.6 Fundamental Data

There are three databases in ADAS which contain the fundamental data relevant for the calculations of the He beam:

helike_kvi97#he0.dat:	electron impact excitation
ionelec_szd#he.dat:	electron impact ionization
he.dat:	ion impact reactions

Each of this data is stored in a different data format ('adf': ADAS data format [1]).

3.6.1 Electron Impact Excitation Data

The fundamental data is stored in an adf04 file called 'helike_kvi97#he0.dat' (current location in ADAS: adf04\helike\) as effective collision strengths Y_{ij}, which are dimensionless parameters defined by

$$\langle \sigma v_r \rangle_{ji} = \left(\frac{2\sqrt{\pi}\alpha c a_o^2}{g_i} \right)^{\left(-\frac{E_j - E_i}{kT_e}\right)} \sqrt{\frac{E_{Ry}}{kT_e}} Y_{ij}, \tag{3.12}$$

where i stands for the lower initial level and j for the higher final level. E_i and E_j are the corresponding binding energies, α denotes the fine-structure constant ($\alpha = 7.297 \cdot 10^{-3}$), a_o the Bohr radius ($a_o = 5.29 \cdot 10^{-11}$ m), g_i the statistical weight of level i, and E_{Ry} the Rydberg energy ($E_{Ry} = 13.6$ eV). The collision strengths depend weakly on T_e. They are given for the transitions shown in tab. 3.2.

Most of the data is taken from a compilation of deHeer [85] from 1995. The data can be interrogated with ADAS201, which produces the corresponding rate coefficients for a chosen electron temperature region. The file also includes spontaneous emission coefficients.

↓i j→	1	3	5	7	10	11	13	16	18	19	2	4	6	8	9	12	14	15	17
1 (1^1S)	–	•	•	•	•	•	•	•	•	•	•	•	•	•	•	•	•	•	•
3 (2^1S)	*	–	•	•	•	•	•	•	•	•	*	•	•	•	•	•	•	•	•
5 (2^1P)	*	*	–	•	•	o	•	•	o	o	*	*	o	o	o	o	o	o	o
7 (3^1S)	*	*	*	–	o	•	o	o	o	•	*	o	o	o	o	o	o	o	o
10 (3^1D)	*	*	*	o	–	•	o	o	•	•	*	o	o	o	o	o	o	o	o
11 (3^1P)	*	*	o	*	*	–	•	•	o	o	*	o	o	o	o	o	o	o	o
13 (4^1S)	*	*	*	o	o	*	–	o	o	•	*	o	o	o	o	o	o	o	o
16 (4^1D)	*	*	*	o	o	*	o	–	•	•	*	o	o	o	o	o	o	o	o
18 (4^1F)	*	*	o	o	*	o	*	*	–	o	*	o	o	o	o	o	o	o	o
19 (4^1P)	*	*	o	*	*	o	*	*	o	–	*	o	o	o	o	o	o	o	o
2 (2^3S)	*	•	•	•	•	•	•	•	•	•	–	•	•	•	•	•	•	•	•
4 (2^3P)	*	*	•	o	o	o	o	o	o	o	*	–	•	o	•	•	o	•	o
6 (3^3S)	*	*	o	o	o	o	o	o	o	o	*	*	–	•	o	o	•	o	o
8 (3^3P)	*	*	o	o	o	o	o	o	o	o	*	o	*	–	•	•	o	•	o
9 (3^3D)	*	*	o	o	o	o	o	o	o	o	*	*	o	*	–	o	•	o	•
12 (4^3S)	*	*	o	o	o	o	o	o	o	o	*	o	o	*	o	–	•	o	o
14 (4^3P)	*	*	o	o	o	o	o	o	o	o	*	o	*	o	*	*	–	•	o
15 (4^3D)	*	*	o	o	o	o	o	o	o	o	*	*	o	*	o	o	*	–	•
17 (4^3F)	*	*	o	o	o	o	o	o	o	o	*	o	o	o	*	o	o	*	–

Table 3.2: Electron impact excitation from level i to level j for the 19 lowest HeI levels ($n \leq 4$). Fundamental data contained in ADAS is marked with •, derived deexcitation data denoted with $*$ (see chapter 3.3), and $\circ$ denotes data not available from ADAS.

3.6.2 Electron Impact Ionization Data

This data is stored in an adf07 file called 'ionelec_szd#he.dat' (current location in ADAS: adf07\ionelec\) as Maxwell-averaged rate coefficients for the following processes:

$$\mathrm{He}(1^1\mathrm{S}) + \mathrm{e}^- \rightarrow \mathrm{He}^+ + 2\mathrm{e}^-$$
$$\mathrm{He}(2^3\mathrm{S}) + \mathrm{e}^- \rightarrow \mathrm{He}^+ + 2\mathrm{e}^-$$
$$\mathrm{He}(2^1\mathrm{S}) + \mathrm{e}^- \rightarrow \mathrm{He}^+ + 2\mathrm{e}^-$$

The rate coefficients for the ground state are taken from Bell *et al.* [86], those for the metastable levels from Fujimoto [34]. The ADAS interrogating routine is ADAS502.

3.6.3 Ion Collision Data

This data is stored as cross sections in adf02 file called 'he.dat' (current location in ADAS: adf02\ionatom\). It contains cross sections for the following processes:

single- and double ionization:

$$He(1^1S) + A^{Z+} \rightarrow He^{+} + A^{Z+} + e^{-}$$
$$He(2^3S) + A^{Z+} \rightarrow He^{+} + A^{Z+} + e^{-}$$
$$He(1^1S) + A^{Z+} \rightarrow He^{2+} + A^{Z+} + 2e^{-}$$

single- and double charge exchange:

$$He(1^1S) + A^{Z+} \rightarrow He^{+} + A^{(Z-1)+*}$$
$$He(2^3S) + A^{Z+} \rightarrow He^{+} + A^{(Z-1)+*}$$
$$He(1^1S) + A^{Z+} \rightarrow He^{2+} + A^{(Z-2)+*}$$

transfer double ionization:

$$He(1^1S) + A^{Z+} \rightarrow He^{2+} + A^{(Z-1)+} + e^{-}$$

excitation:

$$He(1^1S) + H^{+} \rightarrow He^{*} + H^{+}$$

He^* ... $He(2^1S)$, $He(3^1S)$, $He(4^1S)$, $He(2^1P)$ $He(3^1P)$, $He(4^1P)$, $He(3^1D)$, and $He(4^1D)$

The ionization- and charge-exchange cross sections are available for the following ion species A^{Z+}:

$$H^{+}, He^{2+}, Be^{4+}, C^{6+}, \text{and } O^{8+}.$$

The fundamental data for B^{5+}, N^{7+}, and Ne^{10+} is stored as 'total stopping' cross sections only, i.e. the sum of single and double ionisation-, charge-exchange-, and transfer double ionisation cross sections. The data is based on a compilation of Summers [1] from 1990 and 1991, and it can be interrogated by ADAS302.

3.7 Application of He Beams for Plasma Diagnostics

In the present work the potential of He fast beams as diagnostic tools is investigated by modelling the beam emission of a helium beam penetrating into a fusion plasma using assumed plasma temperature- and density profiles. For future application of fast He beams for plasma diagnostics, the inverse procedure has to be applied, i.e. plasma parameters have to be deduced from He emission profiles. Several techniques have been considered as candidates for achieving this goal, e.g.:

Line-intensity ratios,
Inverting the balance equations,
Iterative method, and
Neural networks.

Line-intensity ratios

As already mentioned in chapter 1.2.8.3, this method is used as a standard technique for deduction of temperature- and density profiles from emission of thermal He beams. This is possible as the ratios of singlet/singlet emission of these slow beams (e.g. 668 nm/728 nm) are dominated by plasma density but quite insensitive to temperature, whereas singlet/triplet ratios (e.g. 728 nm/707 nm) are dominated by plasma temperature and quite insensitive to density. As ascertained by Brix [92] and also verified in our sensitivity study (chapter 4.2), the He emission and line-intensity ratios are quite sensitive to the metastable fraction in the beam. A thermal He beam with initially no metastable fraction quickly reaches equilibrium with a very small metastable fraction while penetrating the plasma. In contrast, a fast He beam has an initial metastable fraction of 3% or more from its charge-exchange products. While penetrating the plasma this metastable fraction is being rearranged, which means that the relation between intensity ratios and electron temperature changes along the penetration path. Furthermore, the local population density of the triplet states is dominated by the collision frequency and the line ratio of singlet- and triplet lines becomes sensitive to density as well as temperature.

Inverting the balance equations

This is the standard technique in Li-beam diagnostics for deduction of electron density profiles (see chapter 3.1). Inverting the balance equations of the He beam is not as trivial

as in the Li case since not only one but 3 non-equilibrium levels have to be considered. Furthermore, the Li diagnostics deals with only one plasma parameter, i.e. the electron density, as the observed Li emission is almost independent of the electron temperature. Nevertheless, an algorithm as used for Li beams could be used in first approximation for calculating a density profile using a He-beam emission line which is only weakly sensitive to temperature.

Iterative method

From the beam-emission profile of a HeI line which is mainly sensitive to density, a first approximation of a plasma density profile can be calculated, assuming a reasonable temperature profile. The first approximation of the temperature profile could be obtained from the line-average temperature which is available in real time from other diagnostics. Due to the profile stiffness observed in various Tokamak experiments [88] this first approximation should already be quite accurate in most cases. Having calculated a density profile, the second approximation of the temperature profile can be calculated from the emission profile of a line with reasonable sensitivity to temperature, using the first approximation of the density profile. This procedure can now be iterated. As some line intensities have a high sensitivity to density and only weak sensitivity to temperature, it can be expected that this procedure will quickly converge to a selfconsistent solution.

Neural networks

Neural networks could be used to determine temperature- and density profiles rather quickly. Dragosics [87] investigated such neural networks in view of the application for fast He beam diagnostics. In these first studies the potential of neural networks was tested with Li beam diagnostic emission profiles as the results could be easily cross-checked with results from the inversion method. By training the neural networks with Li-emission profiles and the corresponding density profiles, it was possible to reconstruct the plasma parameter profiles from given emission profiles. A reconstruction accuracy of 6% and a calculation duration of less than 3 ms could be reached, which would enable for real-time evaluation. A disadvantage of this method is the fact that solutions for emission profiles are not reliable in case these profiles are not comparable with any of the training profiles. For the application in He-beam diagnostics not only one but two emission profiles are expected to be needed as input: One profile should be predominantly sensitive to temperature and the other one predominantly sensitive to density. So far it has not been verified whether this method will lead to a selfconsistent solution in the case of He-beam diagnostics.

Chapter 4

Results of Model Calculations

4.1 Predictions for Typical Tokamak Plasmas

In order to investigate the diagnostic potential of fast He beams, extensive modelling calculations of the development of He ground state- and metastable states populations and the resulting intensity profiles of HeI lines of interest for a fast He beam penetrating a plasma have been performed. The profiles of all HeI lines in the optical region have been calculated, i.e. 6 singlet- and 5 triplet lines (see figure 3.2). We used electron density- and temperature profiles taken from ASDEX Upgrade- and JET measurements by the respective standard diagnostics. Calculations have been performed for incident pure 1^1S and pure 2^3S beams, respectively. The results for a beam with an initial metastable fraction between those two extremes can be determined by mixing the two results with the corresponding weight factors. The beam energy was taken in accordance with the energy available for our first experiments at these devices. A neutral beam current of 1 A uniformly distributed over a diameter of 0.1 m ($\hat{=}$ 127 A/m^2) was assumed. With these calculations, predictions for first experiments with fast He beams at Tokamak plasmas (ASDEX Upgrade and JET, see chapter 5) in view of beam attenuation, necessary beam intensity, and the most intense visible lines have been made. Also, we focussed our attention on the redistribution of the initial metastable fraction. A detailed presentation of the calculation results has been given in [89]. In the next subchapters the essential results are discussed.

4.1.1 ASDEX Upgrade Plasma

For ASDEX Upgrade ('AUG'), we have chosen the L-mode discharge #11277 with a line averaged density of $8{\cdot}10^{19}$ m^{-2} and a peak electron temperature of 1.8 keV as input for our modelling. The calculations have been performed for an initial beam composition of pure ground state and pure metastable triplet state, respectively.

4.1.1.1 AUG Plasma Edge

The T_e- and n_e profiles used for the AUG plasma-edge calculations are shown in figure 4.1. The modelling parameters are as follows:

beam energy	30 keV
initial equivalent He beam current	1 A
beam diameter	0.1 m
T_e at separatrix	75 eV
T_e decay length	10 mm
minimum T_e value	4 eV [19] (reached for a penetration depth $\leq$ 0.07 m, see figure 4.1)
n_e at separatrix	$4{\cdot}10^{19}$ m^{-3}
n_e decay length	30 mm
number of calculation steps	200
penetration depth	0.1 m

The results for population density- and line intensity profiles for an initially pure ground-state beam are given in figures 4.2 to 4.4. At the separatrix 1% of the initial beam intensity is attenuated, see figure 4.2. The rise of T_e at 70 mm penetration depth has a definite influence on the 2^3S population. Its behaviour is quite similar to the corresponding triplet-line profiles (see figure 4.3). Figure 4.4 shows the singlet line-intensity profiles for the initially pure ground-state beam. The 728 nm-line intensity profile reflects the progression of the 2^1S population, whereas all other singlet lines show a stronger dependence on the electron-temperature profile. All line profiles for both spin systems show good reproduction of the exponential rise of the electron density in the region with constant electron temperature (penetration depth: 0 to 70 mm).

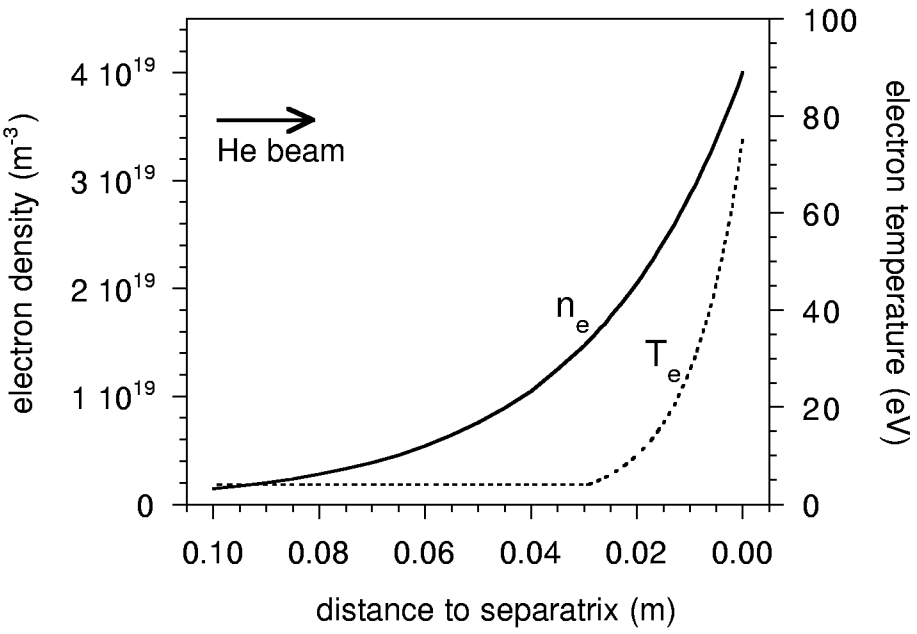

Figure 4.1: n_e- and T_e profiles used for the modelling calculations for a typical AUG edge plasma (discharge #11277).

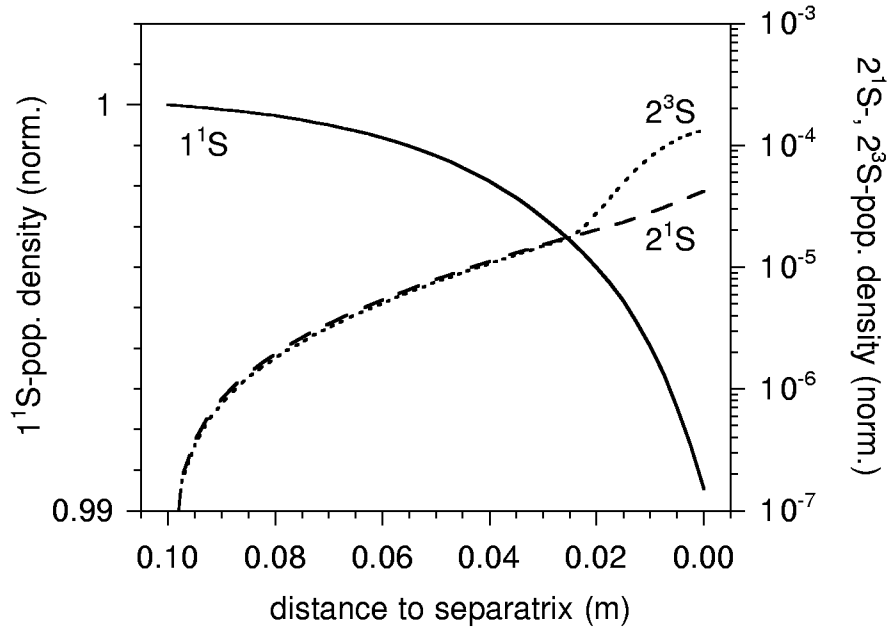

Figure 4.2: Progression of the 1^1S-, 2^1S-, and 2^3S populations for an initially pure 1^1S beam (normalized to the initial beam intensity). The modelling is based on AUG discharge #11277 and a 1 A / 30 keV He beam with 0.1 m diameter.

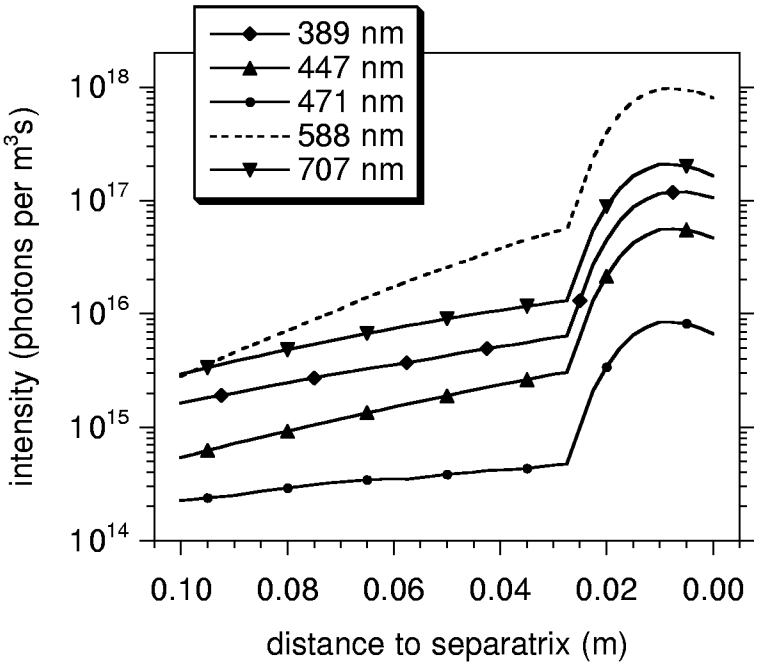

Figure 4.3: Progression of optical HeI-triplet lines for an initially pure 1^1S beam. The modelling is based on AUG discharge #11277 and a 1 A / 30 keV He beam with 0.1 m diameter.

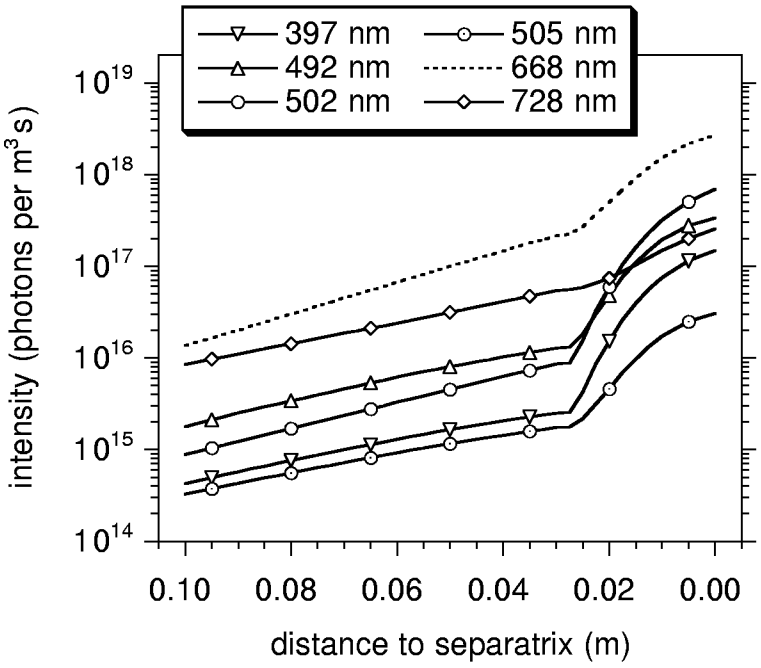

Figure 4.4: Progression of optical HeI-singlet lines for an initially pure 1^1S beam. The modelling is based on AUG discharge #11277 and a 1 A / 30 keV He beam with 0.1 m diameter.

The results for population density- and line-intensity profiles for an initially pure 2^3S beam are given in figures 4.5 to 4.6. At the separatrix the beam is attenuated to 40% of the initial beam intensity, see figure 4.5. De-excitation of the 2^3S into the ground state results in a strong rise of the ground-state population (2% of the initial beam intensity at the separatrix). Also, the 2^1S population shows a much stronger rise (maximum of $4{\cdot}10^{-3}$) compared to that of the initially pure ground-state beam (maximum of $4{\cdot}10^{-5}$, see figure 4.2). Figures 4.6 and 4.7 show singlet- and triplet-line intensities for a pure 2^3S beam. As expected, the triplet-line intensities of the 2^3S beam are much stronger than those resulting for the ground-state beam. In contrast to the 2^3S-population density, the triplet-line intensities rise monotonously, whereas the singlet-line profiles reflect the progression of the 2^1S population density. The correlation between the line-intensity profiles and the electron-temperature profile is not as clearly visible as with the pure ground-state beam, especially in the case of the singlet lines.

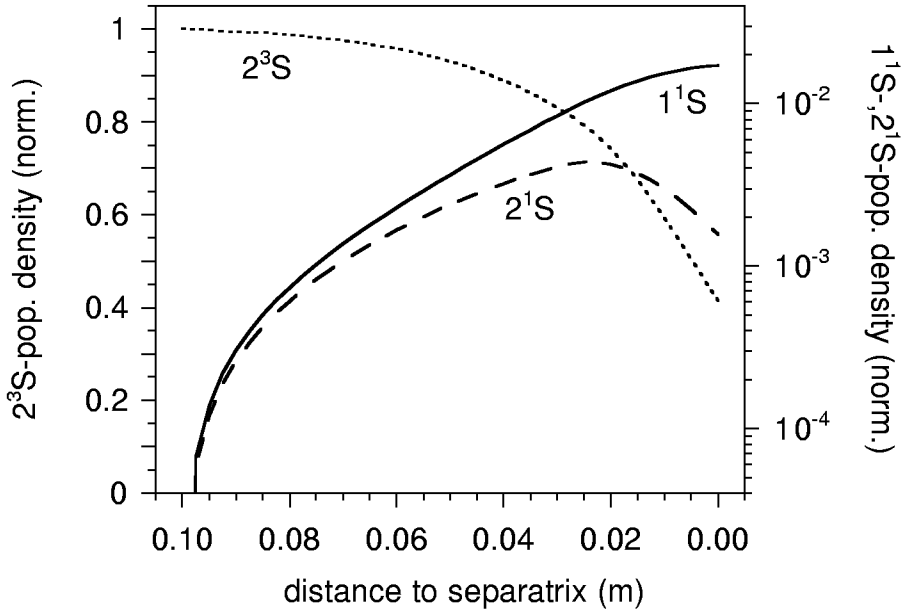

Figure 4.5: Progression of the 1^1S-, 2^1S-, and 2^3S populations for an initially pure 2^3S beam (normalized to the initial beam intensity). The modelling is based on AUG discharge #11277 and a 1 A / 30 keV He beam with 0.1 m diameter.

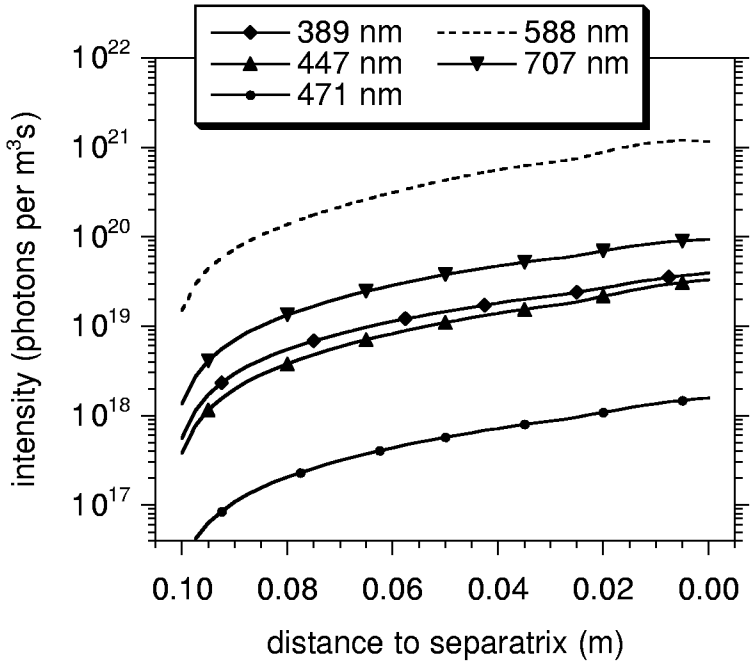

Figure 4.6: Progression of optical HeI-triplet lines for an initially pure 2^3S beam. The modelling is based on AUG discharge #11277 and a 1 A / 30 keV He beam with 0.1 m diameter.

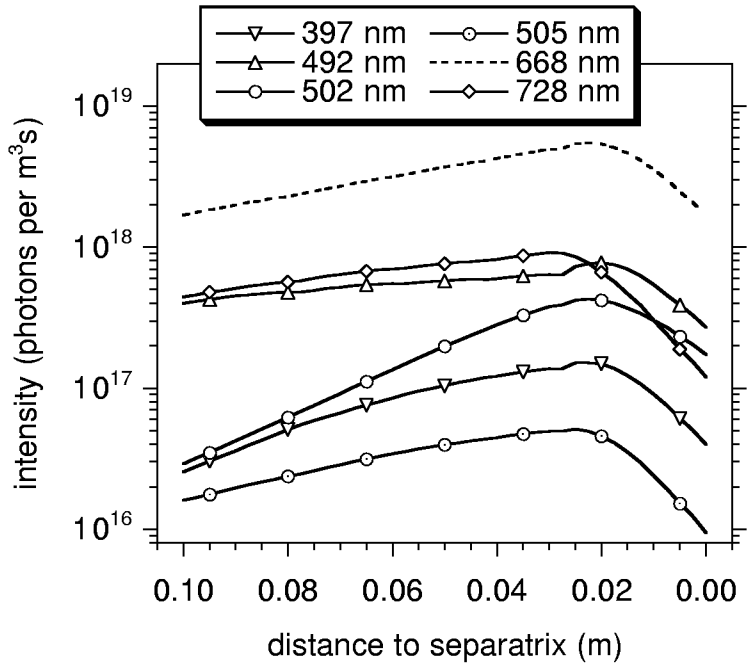

Figure 4.7: Progression of optical HeI-singlet lines for an initially pure 2^3S beam. The modelling is based on AUG discharge #11277 and a 1 A / 30 keV He beam with 0.1 m diameter.

4.1.1.2 AUG Core Plasma

The T_e- and n_e profiles used for the AUG core plasma calculations are shown in figure 4.8. As with the calculations for the plasma edge, a 30 keV He beam of 1 A equivalent current and 0.1 m diameter was considered.

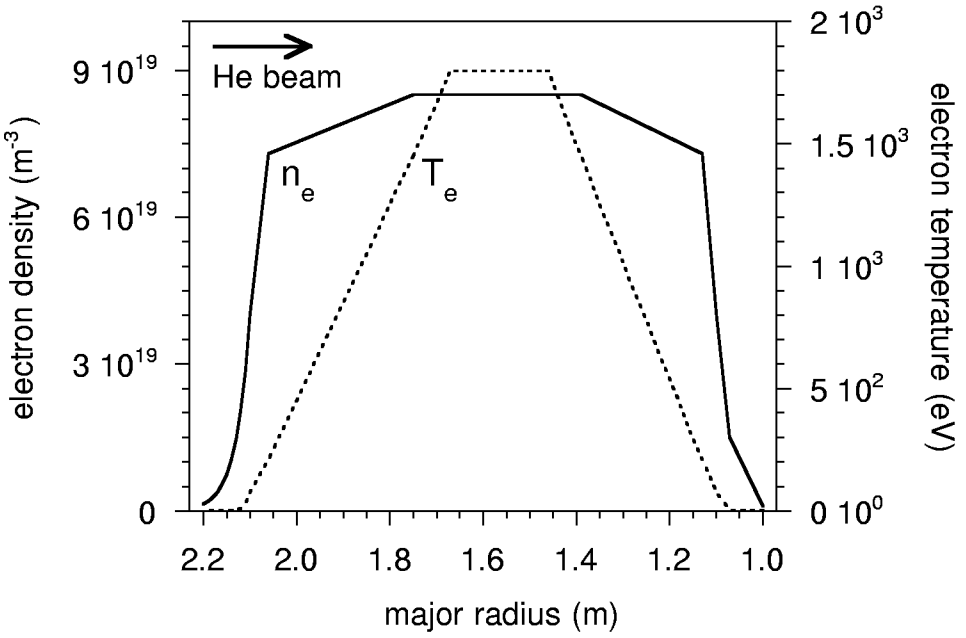

Figure 4.8: n_e- and T_e profiles used for the modelling calculations for a typical AUG core plasma (discharge #11277).

Figure 4.9 shows the radial variation of the non-equilibrium level populations and selected singlet and triplet line-emission profiles for an initially pure 1^1S- and an initially pure 2^3S beam, respectively. Almost all line-intensity profiles of either spin system have the same shape inside the separatrices. Hence, only the most intense lines of each spin system are represented. The 728 nm line-intensity profile differs a little from the other singlet line-intensity profiles. For an illustration of these differences, the progression of the singlet-line intensities are shown in figures 4.10 and 4.11.

After passing the entire plasma the initially pure 1^1S beam is attenuated to 6% of its incident current density. As observed in the plasma edge, the 2^1S-population density is strongly coupled to the 1^1S-population density. The 2^3S-population density shows a quite different behaviour. The 2^3S state is preferably populated in regions with low electron temperature (near the outer and inner separatrix at a major radius of 2.1 m and 1.1 m, respectively),

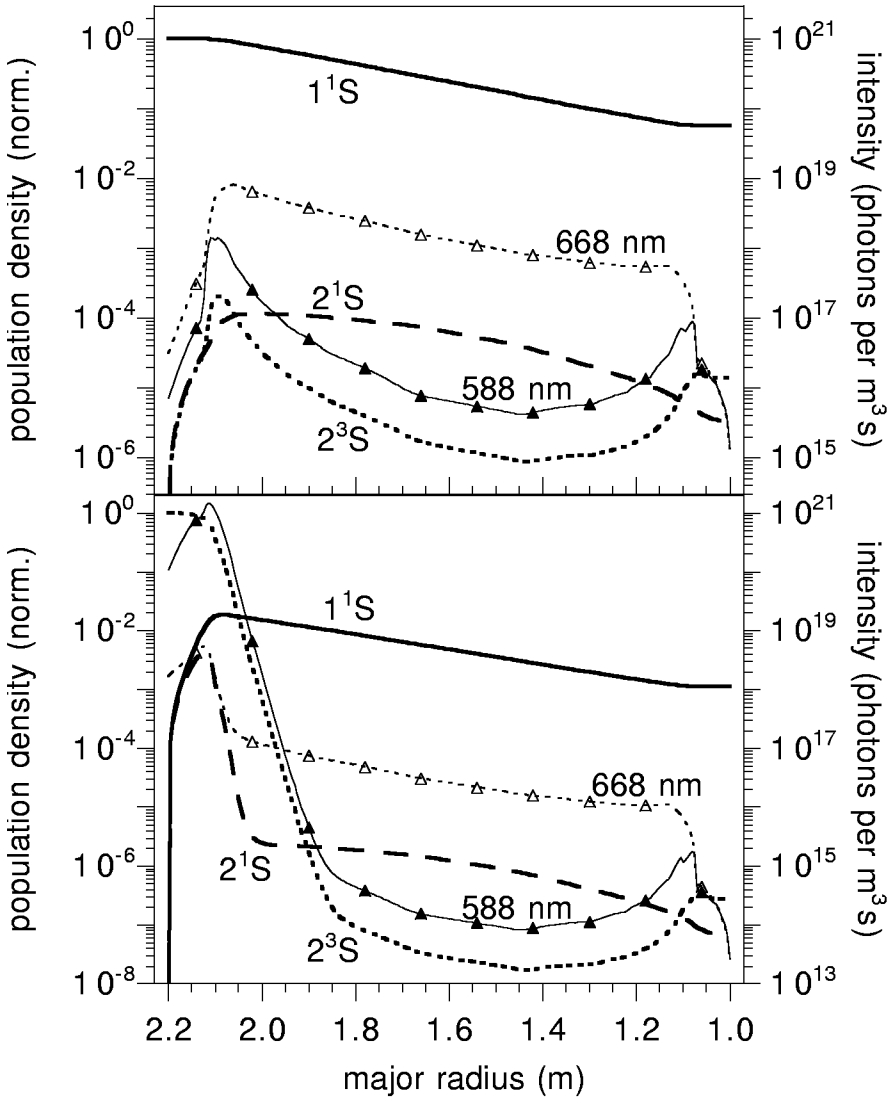

Figure 4.9: Progression of the 1^1S-, 2^1S- and 2^3S populations (normalized to the initial beam intensity) and the most intense singlet (668 nm)- and triplet (588 nm) lines for an initially pure 1^1S- (top) and 2^3S beam (bottom), respectively. The modelling is based on AUG discharge #11277 and a 1 A / 30 keV He beam with 0.1 m diameter.

but strongly depopulated in the hot core. The triplet-line profiles are quite similar to the 2^3S population-density profiles. In figure 4.10 all calculated singlet line-intensity profiles are shown. As observed in the plasma edge (cf. figures 4.4 and 4.2), progression of the 2^1S-population density is represented best by the 728 nm-emission line, see figures 4.9 and 4.10.

The initially pure 2^3S beam decays with an e-folding length of 17 mm (see figure 4.9). Only a few mm inside the separatrix, the ground-state population density reaches its maximum of

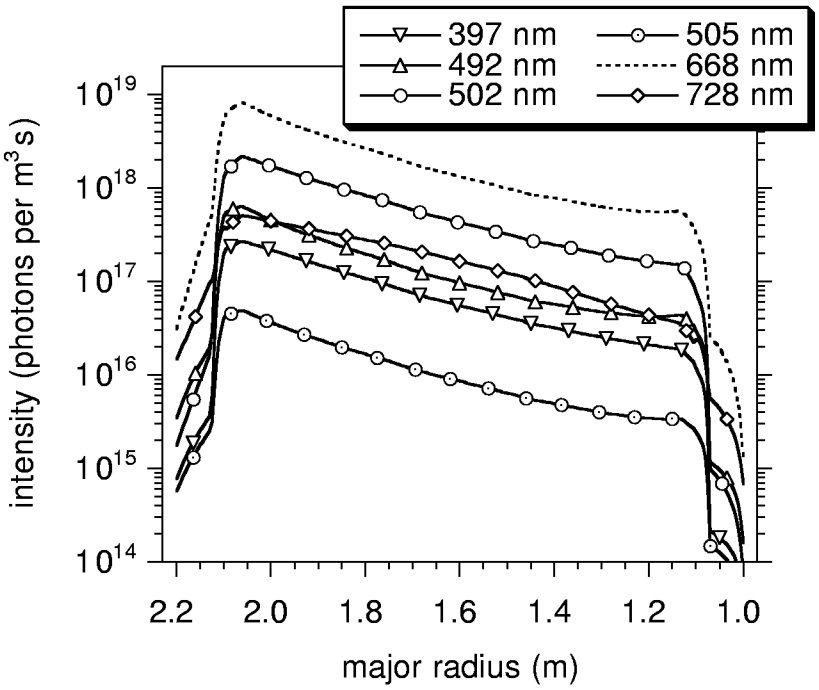

Figure 4.10: Progression of optical HeI-singlet lines for an initially pure 1^1S beam. The modelling is based on AUG discharge #11277 and a 1 A / 30 keV He beam with 0.1 m diameter.

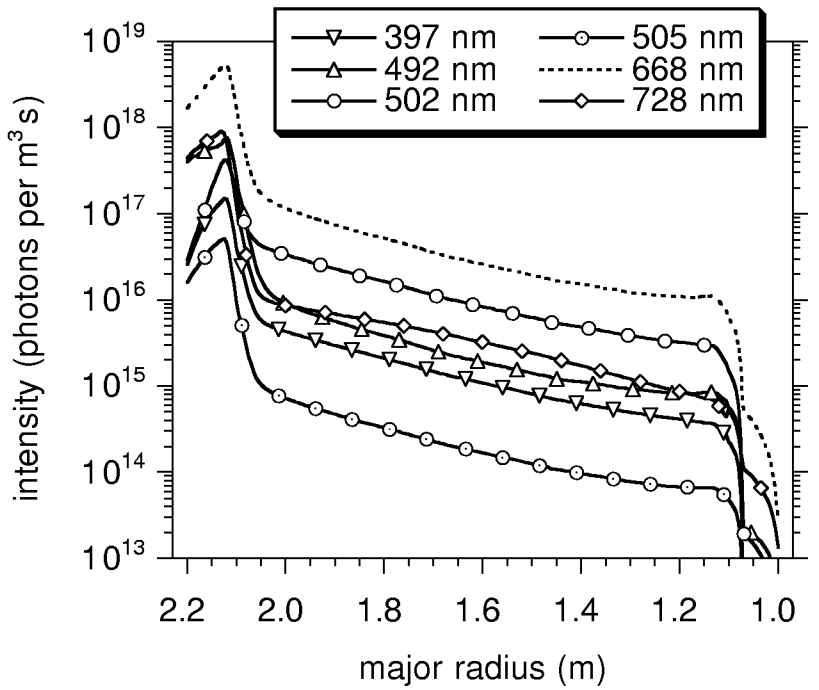

Figure 4.11: Progression of optical HeI-singlet lines for an initially pure 2^3S beam. The modelling is based on AUG discharge #11277 and a 1 A / 30 keV He beam with 0.1 m diameter.

0.02% of the initial beam intensity. As long as the 2^3S concentration outnumbers the ground-state concentration, the progression of the 2^1S-population density is dominated by the 2^3S-population density. In the opposite case the 2^1S-population density is strongly coupled to the ground state. After about 0.3 m a population-density composition independent from the initial beam composition is reached. This means that for such a situation the initial beam composition has no influence on the beam composition in most parts of the core plasma. For an initially pure 2^3S beam the 2^3S concentration in the plasma core is by almost two orders of magnitude lower than in the case of an initially pure ground state beam. This surprising result can be explained by the strong beam attenuation by ionization in the case of the pure 2^3S beam, reducing the beam flux by two orders of magnitude within the first 0.1 m. Again, the line intensity profiles reflect the corresponding metastable state profiles. In figure 4.11 the singlet-line intensity profiles for the initially pure 2^3S beam are shown. Once more, the 728 nm-emission line represents best the progression of the 2^1S-population density.

4.1.2 JET Plasma

For a typical JET plasma we have chosen the H-mode discharge #42676 with a line-averaged density of $3.6{\cdot}10^{20}$ m^{-2} and a peak electron temperature of 5 keV as inputs for our modelling. The calculations have been performed for an initial beam composition with pure ground state and pure metastable triplet state, respectively.

4.1.2.1 JET Plasma Edge

The T_e- and n_e profiles used for the JET plasma-edge calculations are shown in figure 4.12. The modelling parameters are as follows:

beam energy	80 keV
initial equivalent He beam current	1 A
beam diameter	0.1 m
T_e at separatrix	200 eV
T_e decay length	30 mm
n_e at separatrix	$4{\cdot}10^{18}$ m^{-3}
n_e decay length	30 mm
number of calculation steps	200
penetration depth	0.1 m

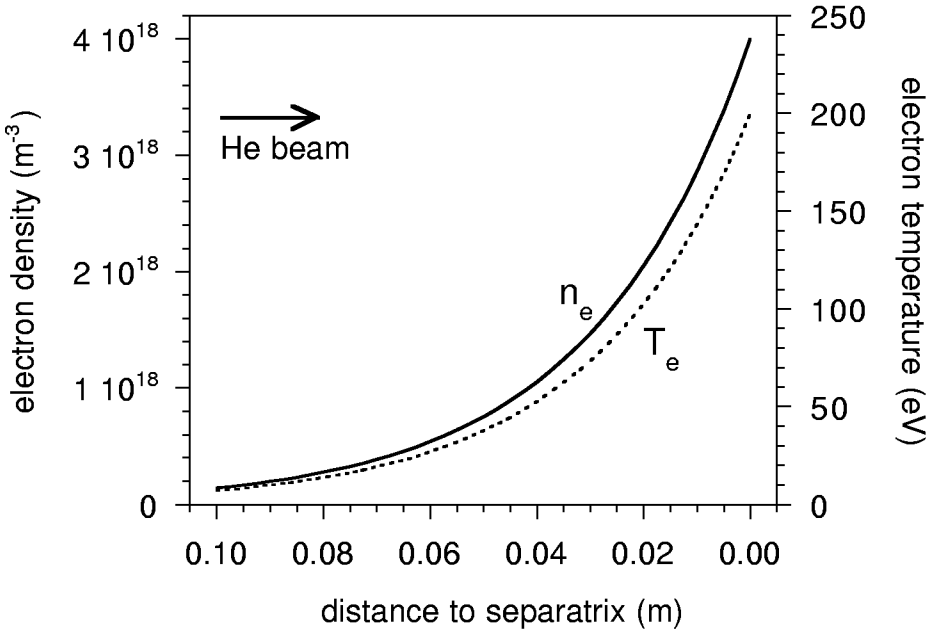

Figure 4.12: n_e- and T_e profiles used for the modelling calculations for a typical JET edge plasma (discharge #42676).

The results for the population density- and the line intensity profiles for the initially pure ground-state beam are given in figures 4.13 to 4.15. At the separatrix only 0.35% of the initial beam intensity is already attenuated, see figure 4.13. The 2^1S-population density shows a similar behaviour to in the AUG case (slower beam, lower n_e- and T_e profiles), and the 2^1S-population density at the separatrix is about one order of magnitude lower than in the AUG case. Due to the high T_e most of the triplet-line profiles already starts to decrease a few cm outside the separatrix (see figure 4.14). Figure 4.15 shows the singlet lines for the initially pure ground-state beam. At the separatrix they have not yet reached their maximum intensity. Compared to the AUG predictive calculations, the line intensities of both the triplet- and singlet system for these calculations for an 80 keV beam penetrating a JET plasma are lower than for the AUG calculations for a 30 keV beam penetrating a less dense plasma.

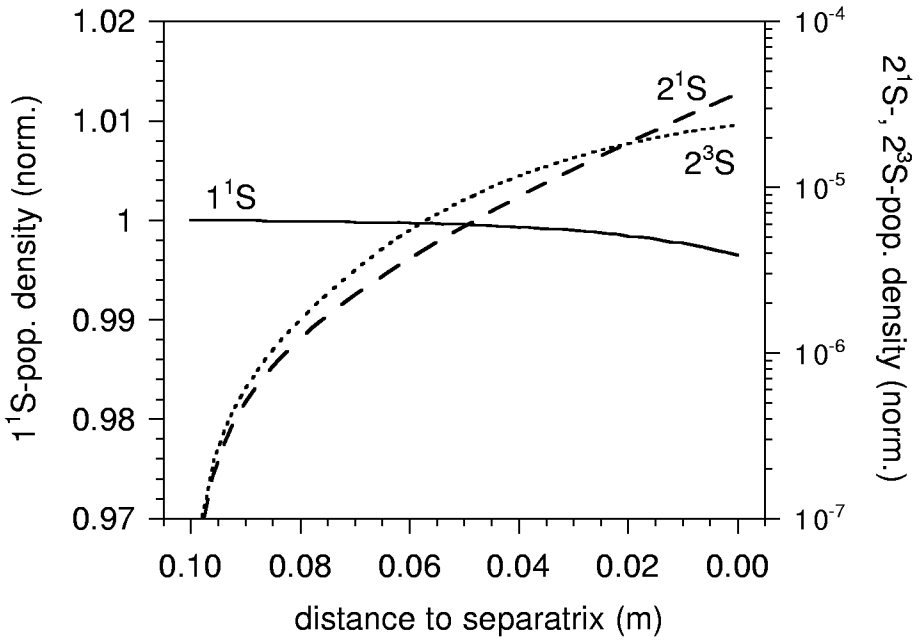

Figure 4.13: Progression of the 1^1S-, 2^1S-, and 2^3S populations for an initially pure 1^1S beam. The modelling is based on JET discharge #42676 and a 1 A / 80 keV He beam with 0.1 m diameter.

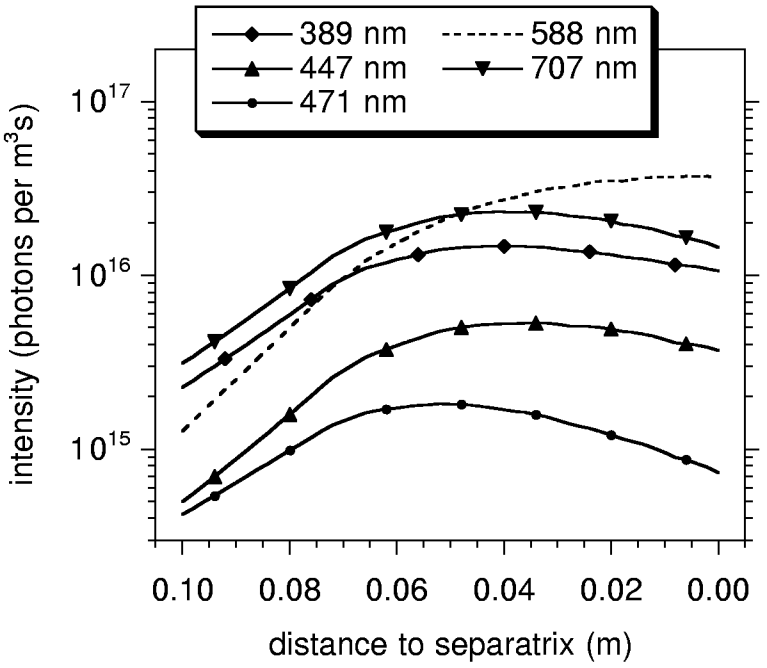

Figure 4.14: Progression of optical HeI-triplet lines for an initially pure 1^1S beam. The modelling is based on JET discharge #42676 and a 1 A / 80 keV He beam with 0.1 m diameter.

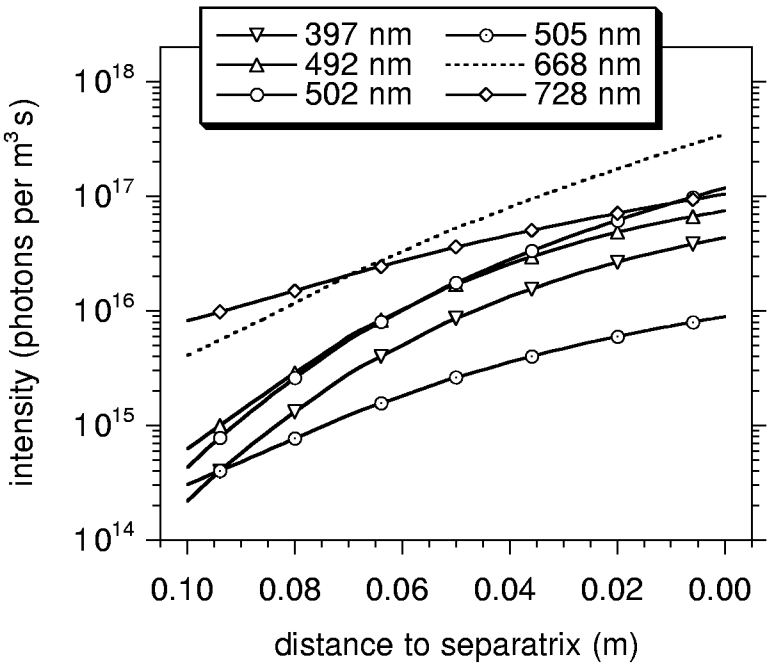

Figure 4.15: Progression of optical HeI-singlet lines for an initially pure 1^1S beam. The modelling is based on JET discharge #42676 and a 1 A / 80 keV He beam with 0.1 m diameter.

The results for the population density- and the line intensity profiles for the initially pure 2^3S beam are given in figures 4.16 to 4.18. At the separatrix only 5% of the initial beam intensity is attenuated, see figure 4.16. The rise of the ground state population ($2{\cdot}10^{-4}$ at the separatrix) due to de-excitation of the 2^3S is much weaker than in the AUG case. The 2^1S population shows a higher rise ($7{\cdot}10^{-5}$ at separatrix) compared to that of the initially pure ground-state beam ($4{\cdot}10^{-5}$ at separatrix, see figure 4.13). The 2^1S-population density is much weaker than in the AUG case (cf. figure 4.5: $1{\cdot}10^{-3}$ at separatrix). Figures 4.17 and 4.18 show singlet- and triplet line intensities for a pure 2^3S beam. As expected, the triplet line-intensity profiles are much more intense than the corresponding population densities in the case of a pure 1^1S beam. In contrast to the 2^3S population density, the triplet-line intensities rise monotonously as in the AUG case. Here, most of the singlet-line intensities do not reflect the progression of the 2^1S population density, since some of them show an almost constant (492 nm, 502 nm, and 668 nm) or even descending profile (505 nm and 728 nm).

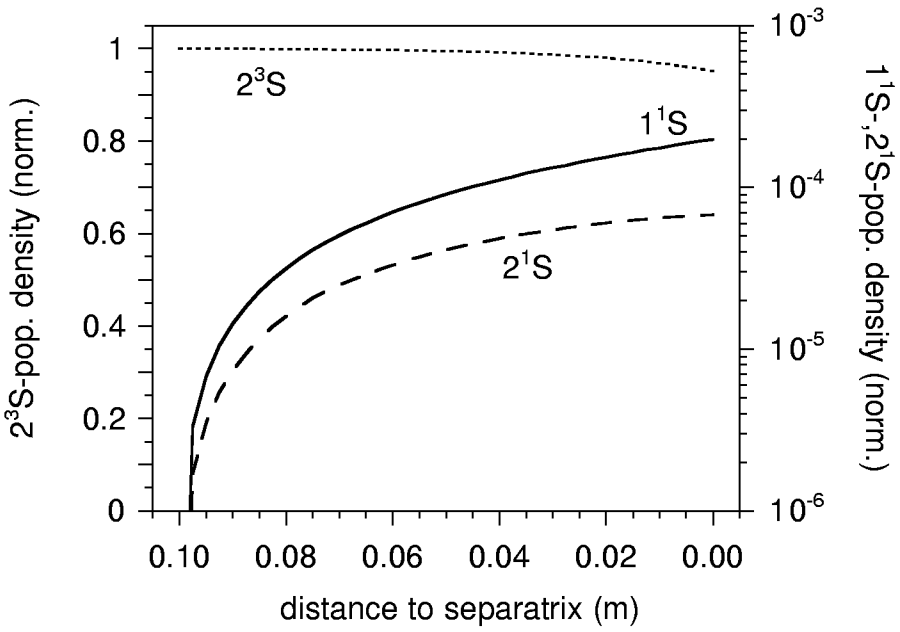

Figure 4.16: Progression of the 1^1S-, 2^1S-, and 2^3S populations for an initially pure 2^3S beam. The modelling is based on JET discharge #42676 and a 1 A / 80 keV He beam with 0.1 m diameter.

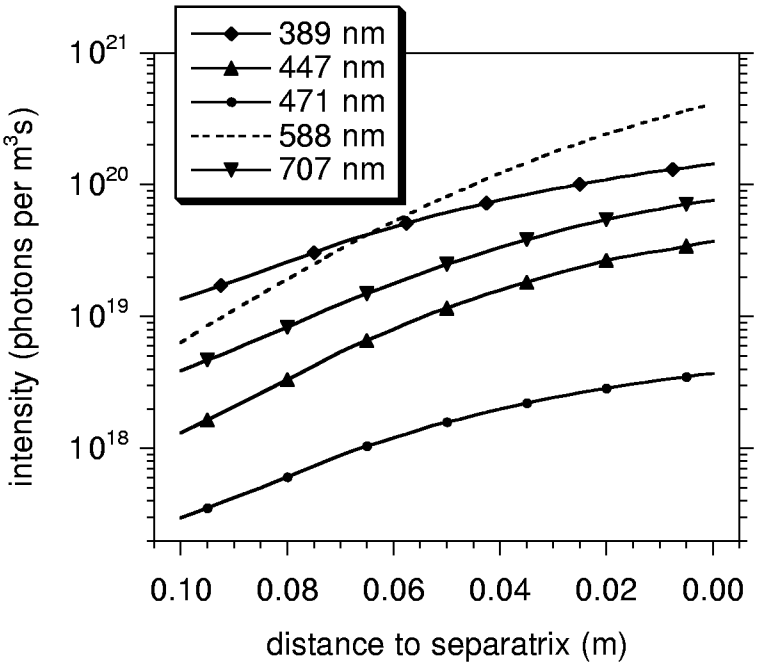

Figure 4.17: Progression of optical HeI-triplet lines for an initially pure 2^3S beam. The modelling is based on JET discharge #42676 and a 1 A / 80 keV He beam with 0.1 m diameter.

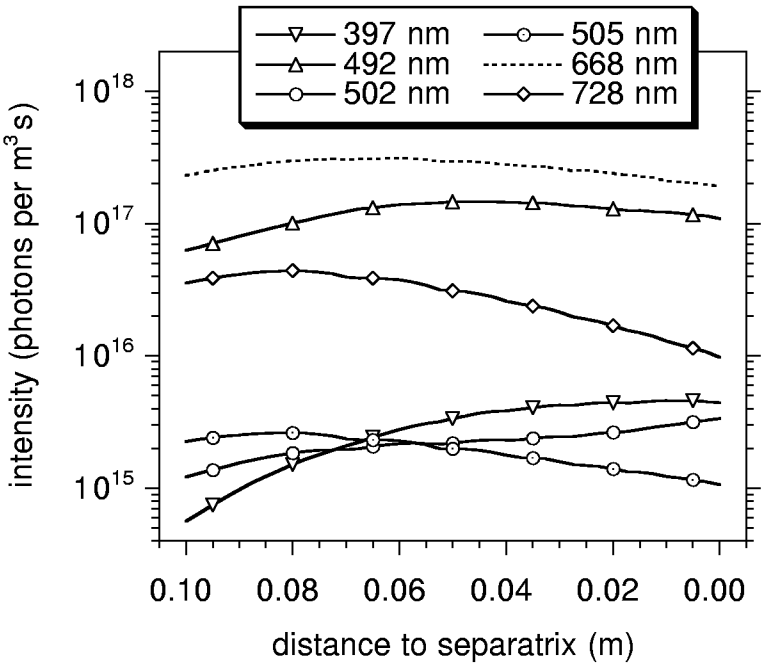

Figure 4.18: Progression of optical HeI-singlet lines for an initially pure 2^3S beam. The modelling is based on JET discharge #42676 and a 1 A / 80 keV He beam with 0.1 m diameter.

4.1.2.2 JET Core Plasma

The T_e- and n_e profiles used for the JET core plasma calculations are shown in figure 4.19. As with the calculations for the plasma edge, an 80 keV He beam of 1 A equivalent current and 0.1 m diameter was considered.

Figure 4.20 shows the radial variation of the non-equilibrium level populations and selected singlet- and triplet line-emission profiles for an initially pure 1^1S- and an initially pure 2^3S beam, respectively. As almost all line-intensity profiles of each spin system show the same behaviour inside the core, only the most intense lines for both spin systems are represented. The singlet-line intensities for the initially pure 2^3S beam show a different behaviour, which is displayed in figure 4.21.

After passing the entire plasma the initially pure 1^1S beam is attenuated to only 40% of its incident current density. This compares with an attenuation to 5% for the predictive calculations for AUG with a slower beam, but lower T_e, n_e, and plasma diameter. As observed in the AUG case, the 2^1S-population density is strongly coupled to the 1^1S-population density, and the 2^3S state is preferably populated in regions with low electron temperature (near the outer and inner separatrix at a major radius of 3.85 m and 2.1 m, respectively), but

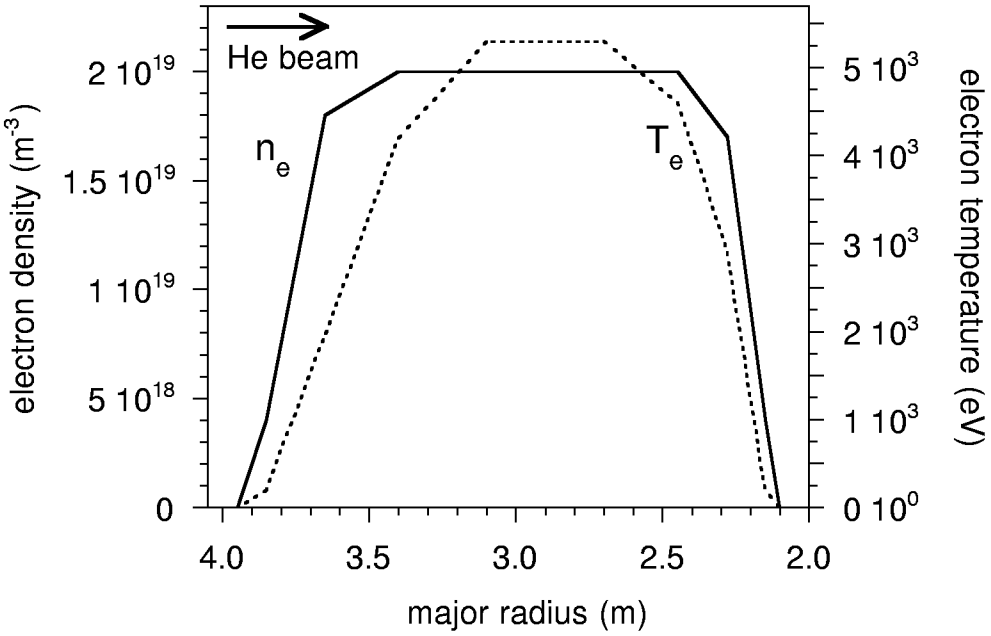

Figure 4.19: n_e- and T_e profiles used for the modelling calculations for a typical JET core plasma (discharge #42676).

strongly depopulated in the hot core. As already mentioned, the line-intensity profiles are very similar to the corresponding metastable population-density profiles. The most intense lines of both spin systems are about one order of magnitude higher than those in the AUG case.

The initially pure 2^3S beam decays with an e-folding length of 105 mm (see figure 4.20). This means that in this case the 2^3S-population density does not reach saturation, in contrast to the AUG case. The progression of the triplet-line intensities inside the core is dominated by the decay of the 2^3S-population density, and no effect of T_e is observed at the inner separatrix. This leads us to the assumption that a high metastable fraction in the beam reduces the temperature sensitivity of the triplet lines (cf. chapter 4.2). About 0.2 m inside the separatrix, the ground-state population density reaches its maximum of 0.04% of the initial beam intensity, which is about 50 times smaller than for the AUG case.

As long as the 2^3S concentration is by more than two orders of magnitude higher than the ground-state concentration, the progression of the 2^1S-population density is dominated by the 2^3S-population density. In the opposite case the 2^1S-population density is strongly coupled to the ground state. Again, the 668 nm line-intensity profile shows the same behaviour as the 2^1S-population density. In figure 4.21 all calculated singlet line-intensity profiles for the initially pure 2^3S beam are given. In contrast to the pure 1^1S beam and both the 1^1S-

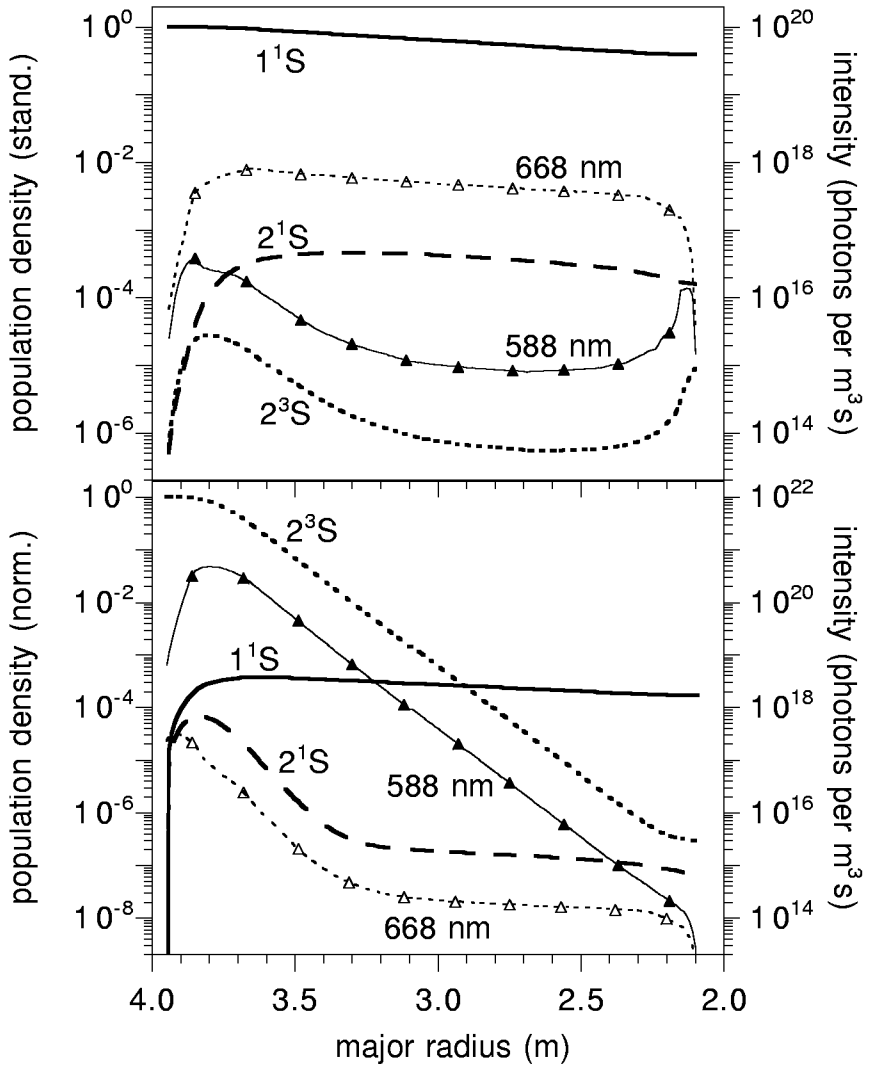

Figure 4.20: Progression of the 1^1S-, 2^1S- and 2^3S populations (normalized to the initial beam intensity) and the most intense singlet (668 nm)- and triplet (588 nm) lines for an initially pure 1^1S- (top) and 2^3S beam (bottom), respectively. The modelling is based on JET discharge #42676 and a 1 A / 80 keV He beam with 0.1 m diameter.

and the 2^3S beam calculated for AUG, the shapes of the singlet-line profiles differ from each other quite strongly. The 492 nm emission line ($4^1\text{D} \rightarrow 2^1\text{P}$) shows strongest coupling to the triplet system. In the region where the 2^1S-population density has reached its saturation, the singlet-line intensities are about two orders of magnitude lower than for the AUG calculations.

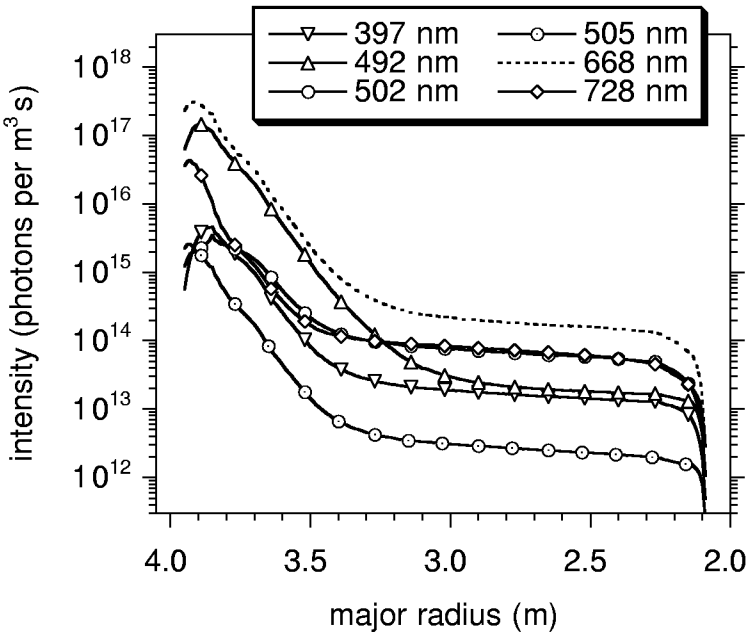

Figure 4.21: Progression of optical HeI-singlet lines for an initially pure 2^3S beam. The modelling is based on JET discharge #42676 and a 1 A / 80 keV He beam with 0.1 m diameter.

4.1.3 Conclusions

The attenuation of a 80 keV He beam penetrating a hot, dense and rather large JET plasma is much weaker than that of a 30 keV He beam injected into a cooler and less dense ASDEX Upgrade plasma with its considerably smaller dimension. In both cases the progression of the singlet lines differs strongly from that of the triplet lines. The triplet states are preferably populated in regions with low electron temperature, i.e. near the outer and inner separatrices. Furthermore, the line-intensities for both spin systems show a quite different behaviour for the different scenarios. This leads to the assumption that the deduction of both T_e and n_e from singlet- and triplet line-intensity measurements is possible, especially with a pure ground-state beam. For a more systematic examination we have studied how the considered emission lines depend on T_e and n_e, as will be presented in chapter 4.2.

Since in the case of a high initial 2^3S fraction the triplet line-intensity profiles are dominated by the strong exponential drop of the 2^3S-population density, we have to assume that the dependence of the triplet lines on the plasma parameter profiles is dramatically reduced. Also, the singlet lines are affected to some extent by the strong depopulation of the triplet system. Hence, our study presented in chapter 4.2 also deals with the consequence of an initial 2^3S fraction on the sensitivity of line intensities to T_e and n_e, respectively.

4.2 Sensitivity Study for n_e- and T_e dependences

In order to assess the potential of He-beam emission for a useful plasma diagnostics, we have examined the sensitivity of the earlier discussed emission lines (chapter 3.4, table 3.1) with respect to T_e and n_e. Based on profiles from a JET ITB discharge, we have calculated the line emission profiles for smooth T_e- and n_e profiles and for profiles with either n_e- or T_e steps in the plasma edge- and core region. As in chapter 4.1.2 a beam with energy of 80 keV, equivalent current of 1 A, and diameter of 0.1 m was chosen.

4.2.1 Plasma Edge and Pedestal

The T_e- and n_e profiles used for the following sensitivity-study calculations for the plasma edge and pedestal are based on discharge #40554. The edge profiles are taken from the scrape-off layer database:

T_e at separatrix	100 eV,
T_e decay length	17 mm,
n_e at separatrix	$1.05{\cdot}10^{19}$ m^{-3},
n_e decay length	12 mm,
location of separatrix	$R_{maj}^{outer} = 3.9$ m, $R_{maj}^{inner} = 2.1$ m.

T_e- and n_e profiles inside the separatrix are taken from LIDAR measurements and, if required, extrapolated to the value at the separatrix as given above. For the calculations we have used either these smooth profiles or profiles with constant sections and steps as shown in figure 4.22.

Calculations have been performed for 3 different scenarios:

- smooth T_e- and n_e profiles,
- smooth T_e profiles, n_e steps,
- smooth n_e profiles, T_e steps.

Both ground-state He beams and He beams with 10% initial 2^3S fraction have been modelled. The results for beams with 10% 2^3S fraction are given in figures 4.23 to 4.28. Figures 4.23 and 4.24 show line-intensity profiles for smooth n_e- and T_e profiles, figures 4.25 and 4.26 the

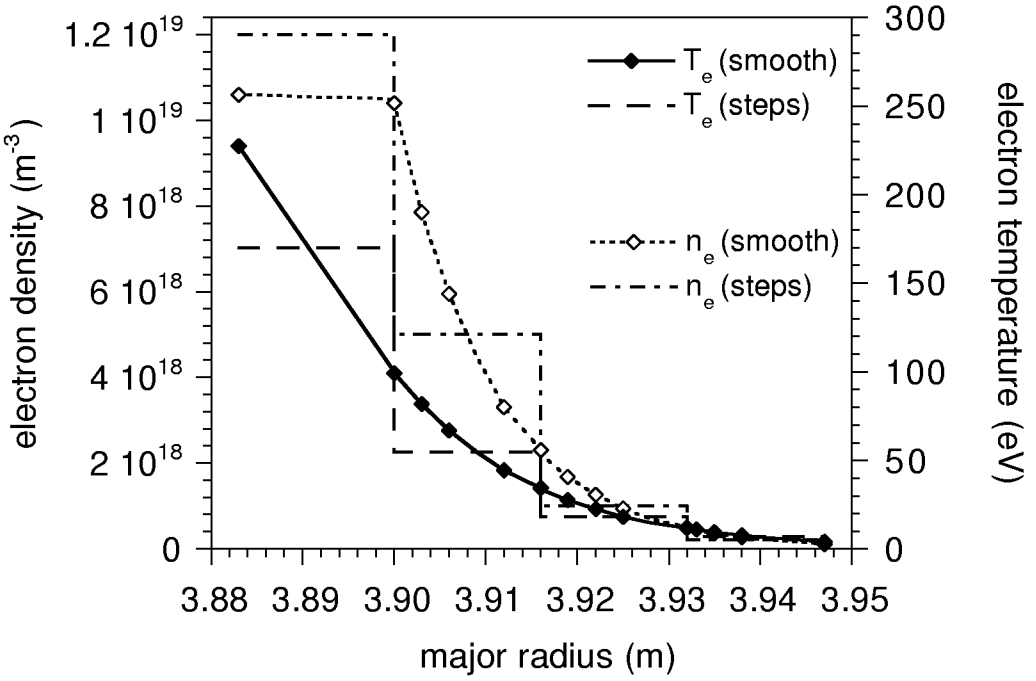

Figure 4.22: n_e- and T_e profiles used for the sensitivity study. The data for the smooth profiles is taken from JET scrape-off layer database and LIDAR measurements for discharge #40554.

ones for n_e steps, and figures 4.27 and 4.28 the ones for T_e steps. Comparison between first experimental results at JET (see chapter 5.2) and the corresponding calculations showed that calculated line intensities have to exceed 10^{16} photons $m^{-3}s^{-1}$ in order to be detected by the spectroscopic system. This limit is marked in the figures.

The intensity of the singlet lines is strongly correlated to n_e as can be seen in figure 4.25. In particular, the profiles of the 668 nm- and 492 nm line have the same shape as the n_e profiles. Both lines are not very sensitive to T_e, as can also be seen in figure 4.27. The 668 nm line appears in the highest intensity which makes it a prime candidate for deriving n_e profiles from emission profiles.

To deduce the T_e profile from line-emission profiles, lines which are primarily sensitive to T_e would be desireable. Unfortunately, all lines are too sensitive with respect to n_e for being suitable for T_e profile deduction on their own. Some singlet lines show a strong sensitivity to T_e, e.g. the 728 nm line which is the second strongest singlet line. The 389 nm triplet line shows the strongest sensitivity to T_e.

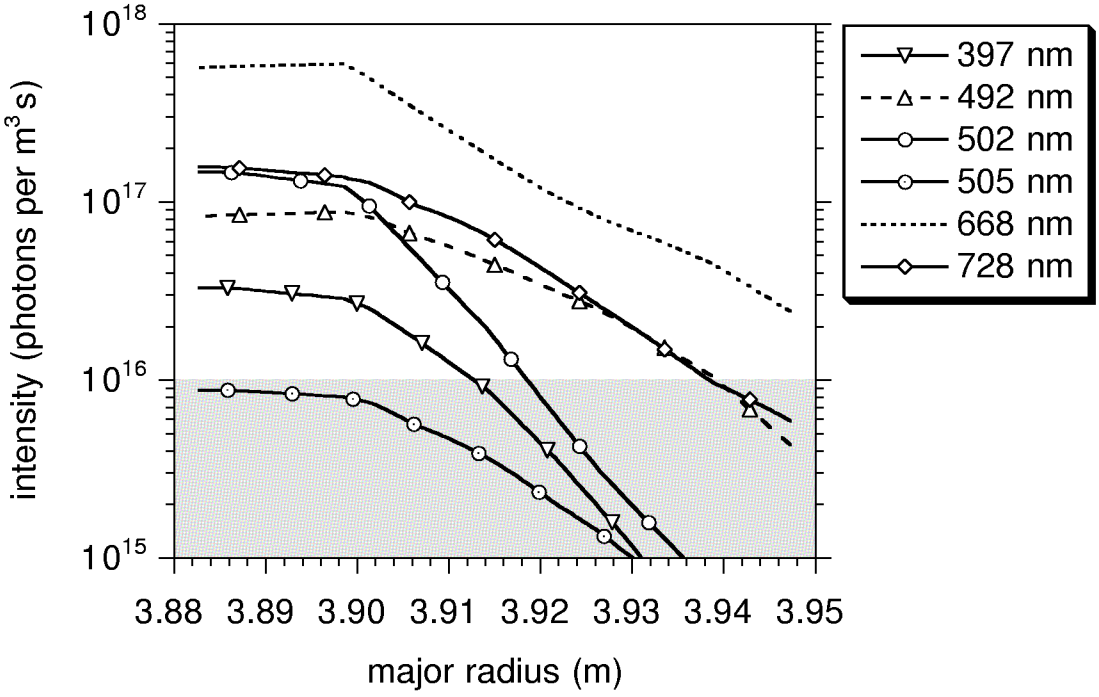

Figure 4.23: Singlet line-intensity profiles for smooth n_e- and T_e profiles and an initial 2^3S fraction of 10%.

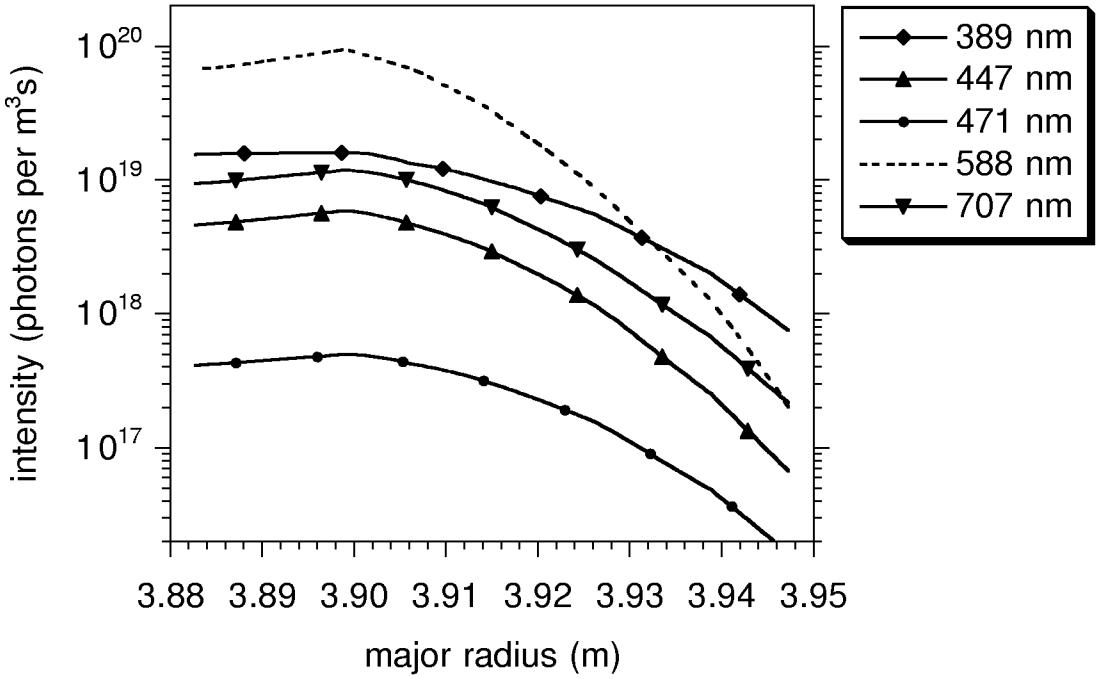

Figure 4.24: Triplet line-intensity profiles for smooth n_e- and T_e profiles and an initial 2^3S fraction of 10%.

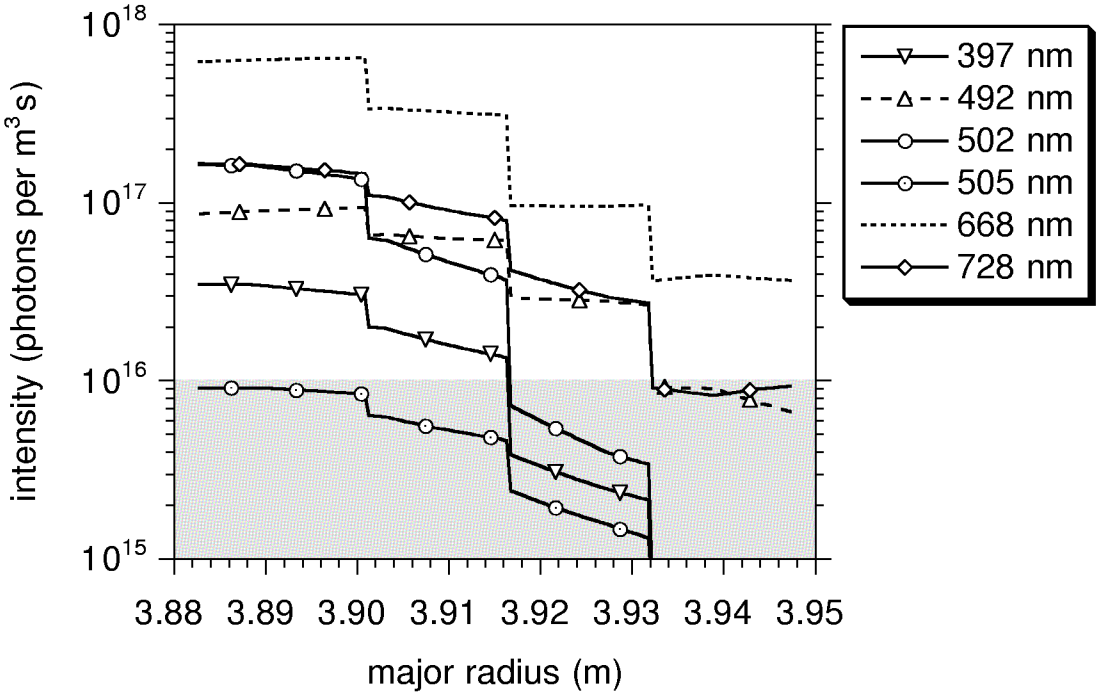

Figure 4.25: Singlet line-intensity profiles for profiles with n_e steps and an initial 2^3S fraction of 10%.

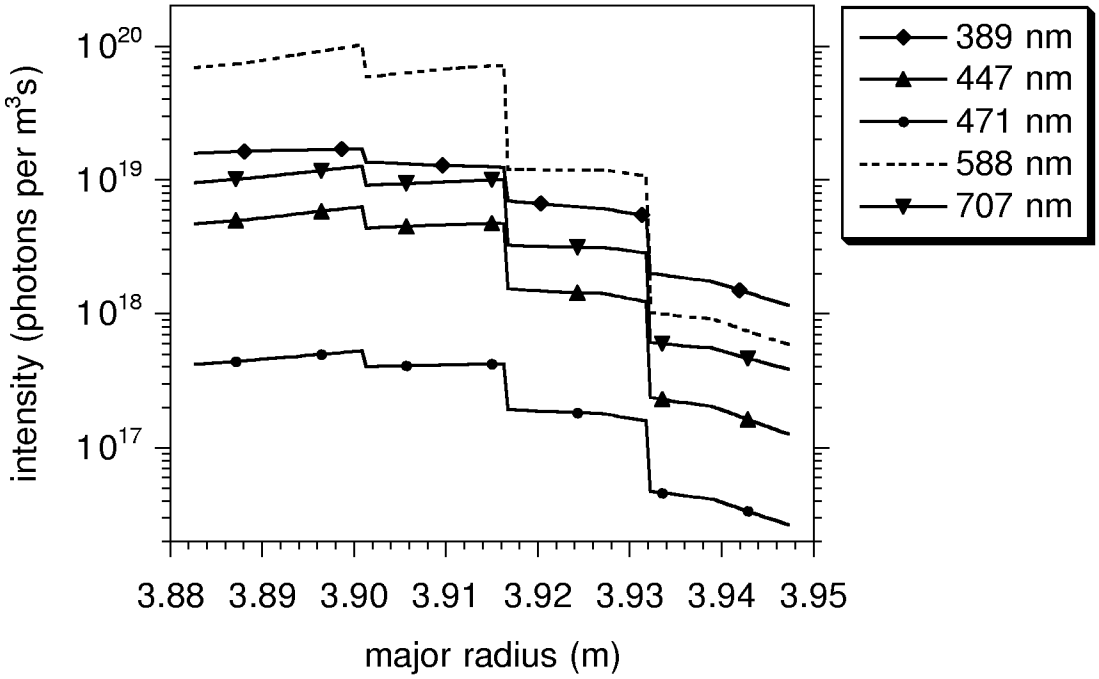

Figure 4.26: Triplet line-intensity profiles for profiles with n_e steps and an initial 2^3S fraction of 10%.

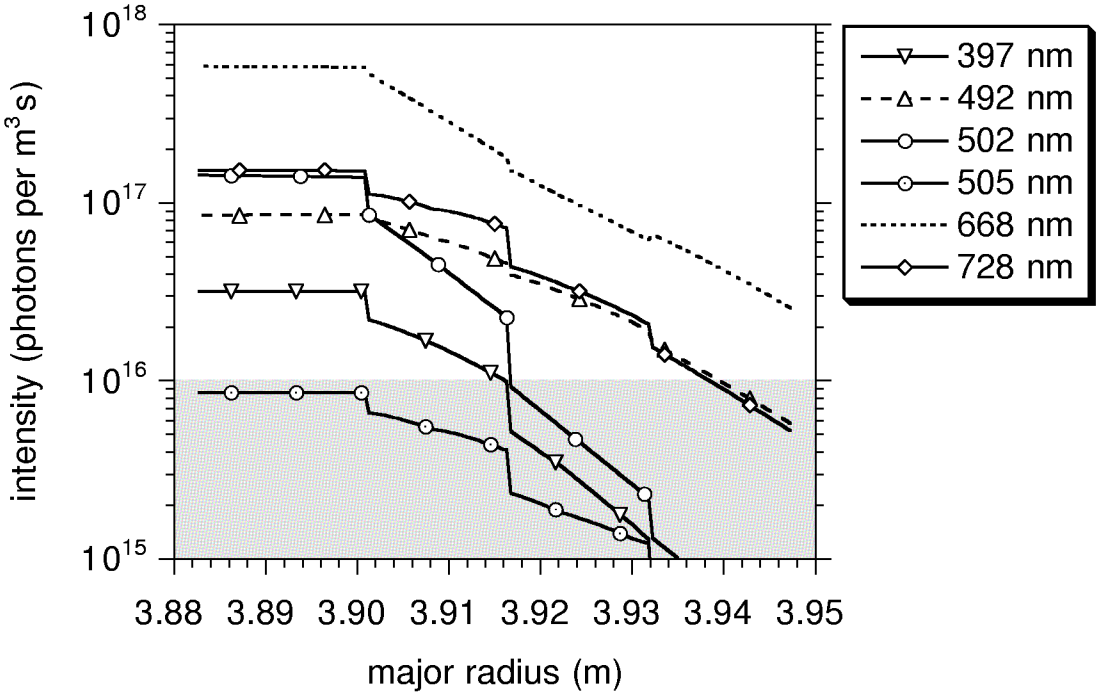

Figure 4.27: Singlet line-intensity profiles for profiles with T_e steps and an initial 2^3S fraction of 10%.

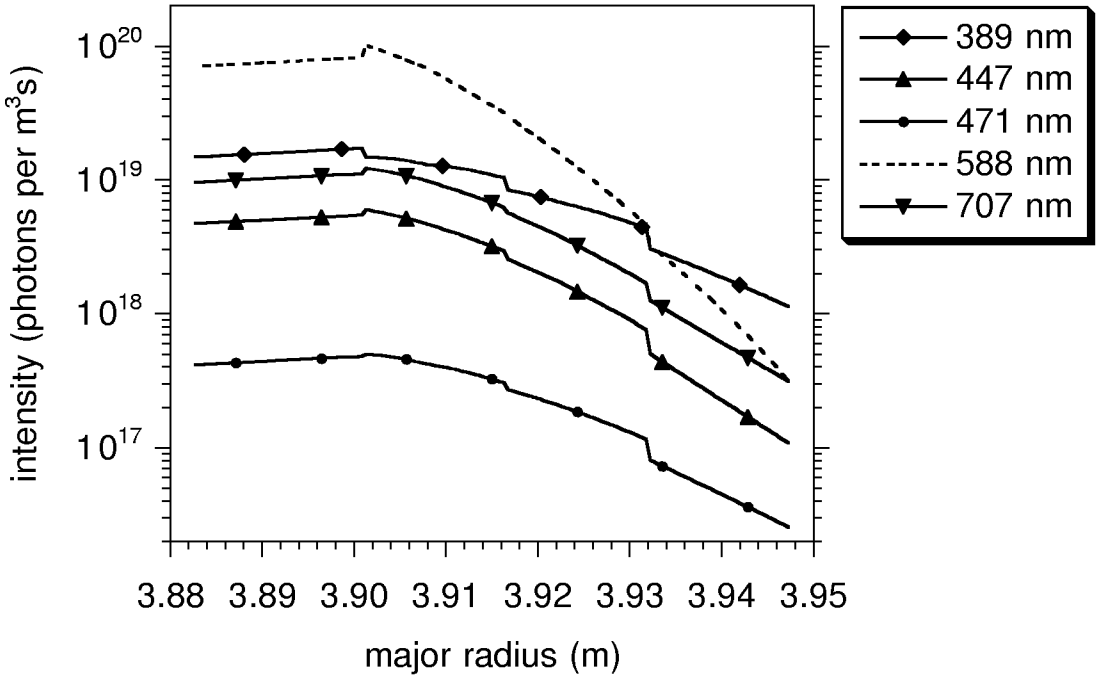

Figure 4.28: Triplet line-intensity profiles for profiles with T_e steps and an initial 2^3S fraction of 10%.

In order to quantify the response of line emission to n_e- or T_e steps, we have calculated the ratios S_n and S_T defined as

$$S_{n,j} = \left(\frac{\Delta I/I}{\Delta n/n} \right)_j \tag{4.1}$$

and

$$S_{T,j} = \left(\frac{\Delta I/I}{\Delta T/T} \right)_j , \tag{4.2}$$

where j defines particular n_e- or T_e steps. $\Delta I/I$ is the relative intensity change, and the $\Delta n/n$ and $\Delta T/T$ give relative changes in n_e and T_e, respectively.

The values of S_n and S_T for a pure ground-state He beam and a He beam with 10% initial 2^3S fraction, respectively, are shown in tables 4.1 to 4.4. For better guidance, values exceeding ± 0.4 are given in bold (high sensitivity to the considered parameter), whereas values between -0.15 and 0.15 are plotted in italic (low sensitivity to the considered parameter).

major radius	T_e in eV	n_e in 10^{18} m^{-3}	397 nm	492 nm	502 nm	505 nm	668 nm	728 nm
			$(\Delta I/I)/(\Delta n/n)$, 0% 2^3S					
3.932 m	11.8	0.2 - 1.0	**1.00**	**0.90**	**1.04**	**0.55**	**0.94**	**0.75**
3.916 m	34.3	1.0 - 5.0	**0.80**	**0.72**	**1.00**	**0.43**	**0.91**	**0.45**
3.901 m	100	5.0 - 12	**0.49**	**0.50**	**0.87**	0.34	**0.81**	0.33
			$(\Delta I/I)/(\Delta n/n)$, 10% 2^3S					
3.932 m	11.8	0.2 - 1.0	**1.13**	**0.72**	**1.00**	**0.63**	**0.69**	**0.75**
3.916 m	34.3	1.0 - 5.0	**0.82**	**0.52**	**1.00**	**0.46**	**0.78**	**0.45**
3.901 m	100	5.0 - 12	**0.49**	**0.43**	**0.87**	0.34	**0.77**	0.33

Table 4.1: Relative emission-intensity changes for n_e steps for all considered singlet lines of a pure ground-state He beam and a He beam with 10% initial 2^3S fraction, respectively.

Basically all singlet lines are rather sensitive to changes in n_e, with S_n values varying between 0.33 and 1.13, see table 4.1. At the separatrix S_n can become relatively small, e.g. 0.33 for the 728 nm line and 0.34 for the 505 nm line. An initial 2^3S fraction of 10% has little impact on the sensitivity to n_e. The 668 nm line is very sensitive to n_e and has almost identical S_n values for all three steps. As already noted (figure 4.25), the 668 nm line is the strongest singlet line and would be an ideal candidate for n_e measurements.

major radius	T_e in eV	n_e in 10^{18} m^{-3}	389 nm	447 nm	471 nm	588 nm	707 nm
			$(\Delta I/I)/(\Delta n/n)$, 0% 2^3S				
3.932 m	11.8	0.2 - 1.0	**0.75**	**0.95**	**0.57**	**1.22**	**0.90**
3.916 m	34.3	1.0 - 5.0	**0.51**	**0.69**	0.30	**1.08**	**0.64**
3.901 m	100	5.0 - 12	0.31	0.40	0.20	**0.67**	0.32
			$(\Delta I/I)/(\Delta n/n)$, 10% 2^3S				
3.932 m	11.8	0.2 - 1.0	**0.68**	**1.01**	**0.81**	**1.24**	**0.97**
3.916 m	34.3	1.0 - 5.0	**0.41**	**0.76**	**0.55**	**1.07**	**0.76**
3.901 m	100	5.0 - 12	0.27	**0.45**	0.34	**0.66**	**0.41**

Table 4.2: Relative emission-intensity changes for n_e steps for all considered triplet lines of a pure ground-state He beam and a He beam with 10% initial 2^3S fraction, respectively .

The sensitivity of the triplet lines with respect to n_e is given in table 4.2. Compared to the singlet lines, S_n is much smaller for most of the triplet lines. The 588 nm line is the most sensitive one. In the outermost region the sensitivity of all triplet lines with respect to n_e is relatively high. Towards the separatrix this sensitivity drops. An increase of the initial 2^3S fraction has little impact on the sensitivity of the triplet lines. As for the singlet lines S_n is relatively high for all triplet lines. The 389 nm line shows the smallest sensitivity and it is very intense.

major radius	T_e in eV	n_e in 10^{18} m^{-3}	397 nm	492 nm	502 nm	505 nm	668 nm	728 nm
			$(\Delta I/I)/(\Delta T/T)$, 0% 2^3S					
3.932 m	7 - 18	1.0	**1.67**	**6.01**	**8.61**	**4.92**	**2.54**	**2.61**
3.916 m	18 - 55	5.0	**0.99**	**0.78**	**1.02**	**0.80**	**0.61**	**0.69**
3.901 m	55 - 170	12	**0.45**	0.22	**0.48**	0.33	0.14	0.34
			$(\Delta I/I)/(\Delta T/T)$, 10% 2^3S					
3.932 m	7 - 18	1.0	**0.64**	0.21	**1.05**	**1.23**	*-0.14*	**0.49**
3.916 m	18 - 55	5.0	**0.59**	*0.14*	**0.80**	**0.52**	*0.14*	**0.47**
3.901 m	55 - 170	12	0.34	*0.05*	**0.44**	0.25	*0.05*	0.29

Table 4.3: Relative emission-intensity changes for T_e steps for all considered singlet lines of a pure ground-state He beam.

Results for S_T for singlet lines are given in table 4.3. In the case of a pure ground-state beam the singlet lines show a larger sensitivity to T_e than to n_e for the two outermost steps, but this is dramatically reduced for the third step located at the separatrix. An increase in

the initial 2^3S fraction results in a strong decrease in S_T. The lines at 492 nm- and 668 nm lose their sensitivity to T_e almost entirely, S_T of the 668 nm line even changes its sign, i.e. a sudden increase in temperature would result in a drop in emitted intensity (cf. figure 4.27). Additionally to its favourable sensitivity to n_e, the 668 nm line shows almost no sensitivity to T_e confirming that this line is the prime candidate for n_e measurements in the plasma edge.

major radius	T_e in eV	n_e in 10^{18} m^{-3}	389 nm	447 nm	471 nm	588 nm	707 nm
			$(\Delta I/I)/(\Delta T/T)$, 0% 2^3S				
3.932 m	7 - 18	1.0	**5.60**	**5.94**	**4.88**	**6.45**	**5.08**
3.916 m	18 - 55	5.0	0.15	*0.07*	*0.07*	*0.03*	*0.05*
3.901 m	55 - 170	12	**-0.53**	**-0.73**	**-0.67**	**-0.79**	**-0.69**
			$(\Delta I/I)/(\Delta T/T)$, 10% 2^3S				
3.932 m	7 - 18	1.0	**0.59**	**0.77**	**0.61**	**0.66**	**0.50**
3.916 m	18 - 55	5.0	0.21	*0.12*	*0.10*	*0.01*	*0.06*
3.901 m	55 - 170	12	0.16	*-0.10*	*-0.04*	-0.24	*-0.10*
			$(\Delta I/I)/(\Delta T/T)$, 1% 2^3S				
3.932 m	7 - 18	1.0	**0.62**	**0.84**	**0.76**	**0.70**	**0.59**
3.916 m	18 - 55	5.0	0.20	*0.12*	*0.10*	*0.01*	*0.06*
3.901 m	55 - 170	12	0.15	*-0.12*	*-0.06*	-0.25	*-0.12*

Table 4.4: Relative emission-intensity changes for T_e steps for all considered triplet lines of a pure ground-state He beam and a He beam with 10% and 1% initial 2^3S fraction, respectively.

Table 4.4 shows the sensitivity of triplet lines to T_e. For a pure ground-state beam values of S_T change dramatically from high positive at the outermost point to high negative at the separatrix. For all emission lines the absolute values for S_T decrease with increasing initial 2^3S fraction. For showing that this reduction in sensitivity already occurs for very small initial metastable fractions, an additional case with 1% 2^3S fraction has been given in table 4.4. The same effect has also been pointed out by Brix [92]. Fast He beams used for the tokamak plasma experiments are produced by neutralization of fast He ions in gaseous targets (H_2, D_2, and He, see chapter 5). These neutral beams have at least a few % of metastable atoms. In spite of the lower sensitivity to T_e for such a realistic metastable fraction the 389 nm line has a relatively constant sensitivity to T_e which should be large enough for T_e evaluation. Assuming that the n_e profile is already known, it appears feasible to derive T_e profiles from the 389 nm line using this n_e profile and the emission profile as

inputs. Some of the singlet lines have comparable or even higher sensitivity to T_e (397 nm, 502 nm, 505 nm, and 728 nm, cf. table 4.1). However, even the most intense one at 728 nm falls below the detection limit of the JET spectroscopic system in the outermost plasma region. Additionally, its sensitivity to n_e is higher than for the 389 nm line. Hence, for T_e measurements the emission line at 389 nm is recommended.

4.2.2 Core Region

The n_e- and T_e profiles for our sensitivity test in the core region are based on JET discharge #40554 which developes an ITB. The profiles were taken from LIDAR measurements (ppf LIDR/NE, LIDR/TE) at 0.2 s (without ITB) and 0.7 s (with ITB) after the start of the high power phase. For our calculations we have used either profiles for which the LIDAR data is linearized within a few ranges, or profiles with constant sections and steps as shown in figures 4.29 and 4.30. Both n_e and T_e are quite high which causes a rather strong beam attenuation. The calculation showed that the beam will be attenuated in the plasma center to about 72% of its initial ground-state population density in case of the lower profiles (before ITB phase), whereas in case of the higher profiles (during ITB phase) the beam attenuation is about 64%.

Calculations have been performed for 6 different scenarios:

1. linearized T_e- and n_e profiles before ITB phase,
2. same as 1. but with n_e steps,
3. same as 1. but with T_e steps,
4. linearized T_e- and n_e profiles during ITB phase,
5. same as 4. but with n_e steps,
6. same as 4. but with T_e steps.

In order to quantify the response of the line emissions to n_e- or T_e steps, we have calculated S_n and S_T (see equations 4.1 and 4.2) at each position with a n_e- or T_e step.

The values of S_n and S_T (cf. equations 4.1 and 4.2) for a pure ground-state He beam and a He beam with an initial 2^3S fraction of 10% are shown in tables 4.5 to 4.8. Once again, values exceeding ± 0.4 are indicated in bold, those between -0.15 and 0.15 in italic, respectively.

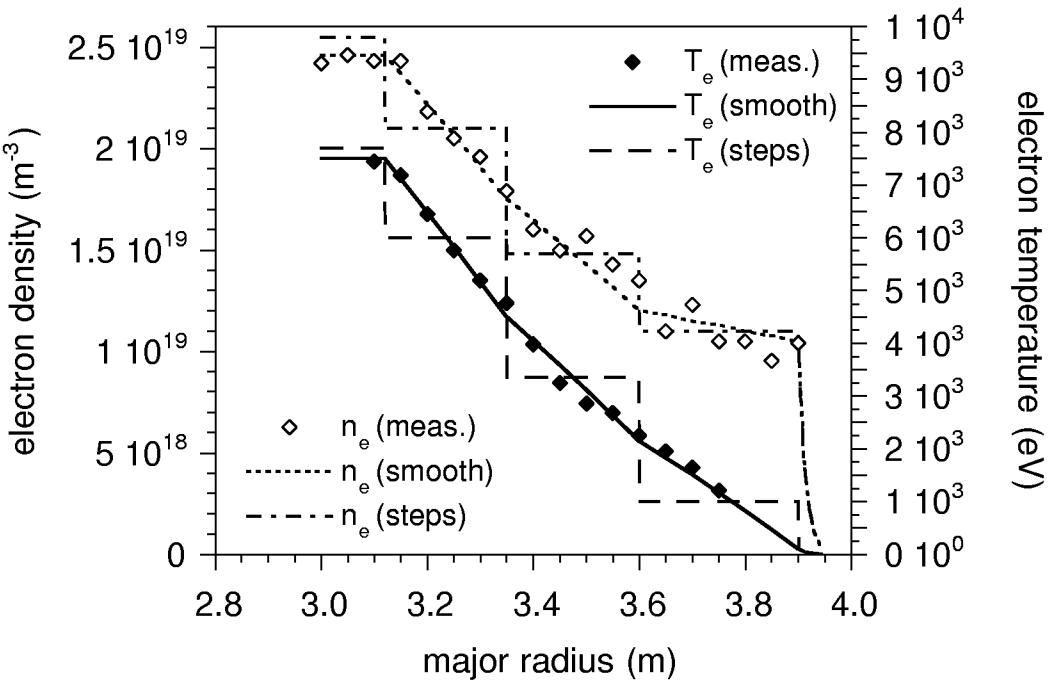

Figure 4.29: n_e- and T_e profiles used for the sensitivity study of the JET core region. Data is taken from LIDAR measurements (JET discharge #40554) at 0.2 s after start of the high power phase.

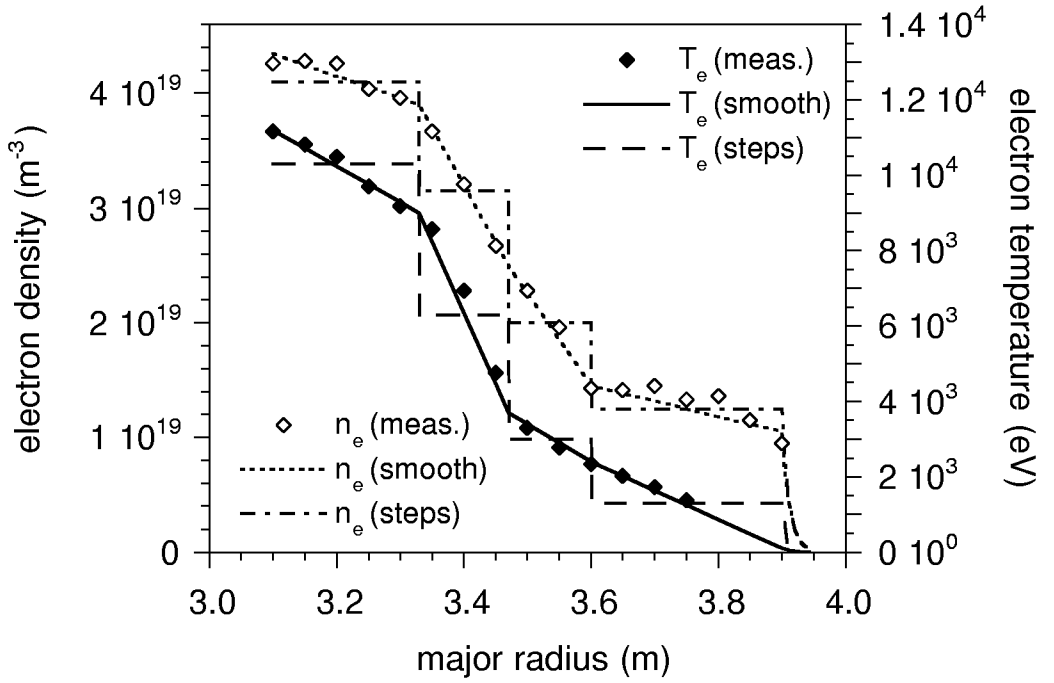

Figure 4.30: n_e- and T_e profiles used for the sensitivity study of the JET core region. Data is taken from LIDAR measurements (JET discharge #40554) at 0.7 s after start of the high power phase.

major radius	T_e in keV	n_e in 10^{19} m^{-3}	397 nm	492 nm	502 nm	505 nm	668 nm	728 nm
			$(\Delta I/I)/(\Delta n/n)$ before ITB formation, 0% 2^3S					
3.60 m	2.15	1.10 - 1.48	**0.49**	**0.57**	**0.81**	**0.43**	**0.78**	**0.42**
3.35 m	4.50	1.48 - 2.10	0.39	**0.50**	**0.78**	0.29	**0.76**	0.27
3.12 m	7.50	2.10 - 2.55	0.27	**0.44**	**0.78**	*0.14*	**0.76**	*0.10*
			$(\Delta I/I)/(\Delta n/n)$ before ITB formation, 10% 2^3S					
3.60 m	2.15	1.10 - 1.48	**0.49**	**0.56**	**0.81**	**0.43**	**0.78**	**0.42**
3.35 m	4.50	1.48 - 2.10	0.39	**0.50**	**0.78**	0.29	**0.76**	0.27
3.12 m	7.50	2.10 - 2.55	0.27	**0.44**	**0.78**	*0.14*	**0.76**	*0.10*
			$(\Delta I/I)/(\Delta n/n)$ after ITB formation, 0% 2^3S					
3.60 m	2.4	1.25 - 2.00	**0.43**	**0.54**	**0.81**	0.35	**0.79**	0.33
3.47 m	3.7	2.00 - 3.15	0.26	**0.42**	**0.77**	*0.12*	**0.75**	*0.09*
3.33 m	9.0	3.15 - 4.10	0.36	**0.49**	**0.64**	0.34	**0.67**	0.33
			$(\Delta I/I)/(\Delta n/n)$ after ITB formation, 10% 2^3S					
3.60 m	2.4	1.25 - 2.00	**0.43**	**0.53**	**0.81**	0.35	**0.78**	0.33
3.47 m	3.7	2.00 - 3.15	0.26	**0.42**	**0.77**	*0.12*	**0.75**	*0.09*
3.33 m	9.0	3.15 - 4.10	0.36	**0.49**	**0.64**	0.34	**0.67**	0.33

Table 4.5: Relative emission-intensity changes for n_e steps for all considered singlet lines of a pure ground-state He beam and a He beam with 10% initial 2^3S fraction, respectively.

Table 4.5 shows S_n for all considered singlet lines. The S_n for the singlet lines in the core region are smaller than in the edge region. Nevertheless, the sensitivity to n_e is satisfactory. S_n has values between 0.27 and 0.81 for all lines but at 505 nm and 728 nm. Occasionally S_n can become rather weak, e.g. 0.09 for the 728 nm line and 0.12 for the 505 nm line. An initial 2^3S fraction of 10% has almost no effect on S_n. The 502 nm-, 668 nm-, and 492 nm lines are the most sensitive ones with respect to S_n, showing only small variations over the whole core region. The 492 nm line is of much weaker intensity in the core than the other two lines (about by one order of magnitude lower than the 668 nm intensity). Hence, 502 nm and 668 nm are the prime candidates for deriving n_e in the core region.

The sensitivity of the triplet lines with respect to n_e is given in table 4.6. Compared to the singlet lines, S_n is much smaller for most of the triplet lines with 588 nm line being the most sensitive one. In the outermost region the sensitivities of all triplet lines with respect to n_e are relatively high. Towards the plasma center this sensitivity drops. In some cases S_n even changes its sign, i.e. a sudden increase in temperature results in a drop in the emitted intensity (389 nm, 471 nm, and 707 nm). An increase of the initial 2^3S fraction has little

major radius	T_e in keV	n_e in 10^{19} m^{-3}	389 nm	447 nm	471 nm	588 nm	707 nm
			$(\Delta I/I)/(\Delta n/n)$ before ITB formation, 0% 2^3S				
3.60 m	2.15	1.10 - 1.48	0.32	0.39	0.33	**0.52**	0.36
3.35 m	4.50	1.48 - 2.10	*0.14*	0.26	0.18	**0.45**	0.23
3.12 m	7.50	2.10 - 2.55	-0.17	*0.02*	*-0.11*	0.31	*-0.01*
			$(\Delta I/I)/(\Delta n/n)$ before ITB formation, 10% 2^3S				
3.60 m	2.15	1.10 - 1.48	0.30	0.38	0.33	**0.51**	0.36
3.35 m	4.50	1.48 - 2.10	0.15	0.25	0.17	**0.46**	0.23
3.12 m	7.50	2.10 - 2.55	*-0.13*	*0.04*	*-0.09*	0.35	*0.01*
			$(\Delta I/I)/(\Delta n/n)$ after ITB formation, 0% 2^3S				
3.60 m	2.4	1.25 - 2.00	0.23	0.33	0.25	**0.52**	0.30
3.47 m	3.7	2.00 - 3.15	*-0.13*	*0.05*	*-0.10*	0.35	*-0.02*
3.33 m	9.0	3.15 - 4.10	0.19	0.24	0.22	0.33	0.25
			$(\Delta I/I)/(\Delta n/n)$ after ITB formation, 10% 2^3S				
3.60 m	2.4	1.25 - 2.00	0.22	0.33	0.26	**0.51**	0.31
3.47 m	3.7	2.00 - 3.15	*-0.14*	*0.06*	*-0.07*	0.35	*0.02*
3.33 m	9.0	3.15 - 4.10	0.17	0.22	0.19	0.30	0.21

Table 4.6: Relative emission-intensity changes for n_e steps for all considered triplet lines of a pure ground-state He beam and a He beam with 10% initial 2^3S fraction, respectively.

impact on the sensitivity of the triplet lines. To deduce T_e profiles from line emission profiles, lines which are mainly sensitive to T_e changes would be advantageous. Unfortunately, S_n becomes relatively high for each triplet line at least for some T_e/n_e combinations, as already observed in the edge region. The 389 nm- and 471 nm lines show the smallest sensitivity. The 471 nm line is the least intense one, whereas emission at 389 nm is very strong. Hence, the emission line at 389 nm would be most suitable for T_e deduction provided its sensitivity to T_e is not too small.

Results of S_T for singlet lines are given in table 4.7. As with S_n, the sensitivities of the singlet lines with respect to T_e are practically not effected at all by an increase for the initial 2^3S fraction. Hence, only the results for the pure ground-state beam are presented in table 4.7. As expected, the singlet lines are not as sensitive to T_e as to n_e. For most lines, S_T is rather weak and decreases towards the plasma center. The 502 nm- and 492 nm lines have negative correlation to T_e for all steps. The 502 nm line was suitable for deducing n_e profiles because of its high sensitivity to n_e. In the edge region this line was not further considered due to its weak intensity. As this line has a rather small sensitivity to T_e for all steps considered, it

major radius	T_e in keV	n_e in 10^{19} m^{-3}	397 nm	492 nm	502 nm	505 nm	668 nm	728 nm
			$(\Delta I/I)/(\Delta T/T)$ before ITB formation, 0% 2^3S					
3.60 m	1.00 - 3.35	1.20	*-0.09*	-0.26	*-0.14*	*-0.11*	-0.25	*0.14*
3.35 m	3.35 - 6.00	1.75	*-0.07*	-0.21	*-0.12*	*0.00*	*-0.17*	0.23
3.12 m	6.00 - 7.70	2.46	*0.03*	*-0.06*	*-0.01*	*0.08*	*-0.02*	0.21
			$(\Delta I/I)/(\Delta T/T)$ after ITB formation, 0% 2^3S					
3.60 m	1.3 - 3.0	1.45	*-0.09*	-0.24	*-0.14*	*-0.09*	-0.23	*0.14*
3.47 m	3.0 - 6.3	2.50	*-0.06*	-0.19	*-0.11*	*0.00*	-0.15	0.22
3.33 m	6.3 - 10.3	3.90	*0.04*	*-0.06*	*0.00*	*0.10*	*-0.02*	0.25

Table 4.7: Relative emission-intensity changes for T_e steps for all considered singlet lines of a pure ground-state He beam.

looks most promising for deriving n_e profiles in the core region. The 668 nm line which also has a high sensitivity to n_e, appears to be less suitable because of its higher S_T value.

Table 4.8 shows the sensitivity of triplet lines with respect to T_e. In the case of a pure ground-state beam all values of S_T are negative. As for the singlet lines, the absolute values of S_T decrease towards the plasma center. Nevertheless, line emission at all wavelengths apart from line at 389 nm shows a useful sensitivity to T_e for all steps. For all emission lines the absolute values for S_T decrease with increasing initial 2^3S fraction. As observed in the edge region, this reduction in sensitivity already occurs at very small initial metastable fractions as can be seen from the values for a beam with 1% 2^3S fraction given in table 4.8. Nevertheless, both the 389 nm- (positive S_T) and the 588 nm emission line (negative S_T) for a beam with a few percent metastable fraction display rather constant sensitivities to T_e which are large enough for useful evaluation. Since the 588 nm line is much more sensitive to n_e than the 389 nm line, the latter one would be favourable for T_e deduction in the core region.

4.2.3 Conclusions

The here presented sensitivity study showed that a He beam with an initial 2^3S content is much less sensitive to T_e than a pure ground-state beam. Since fast He beams produced by He^+ neutralization in a gaseous target always contain at least a few percent of metastable atoms, only results with a non-zero metastable fraction are relevant.

In order to derive from measured line-emission profiles the T_e- and n_e profiles, such lines

major radius	T_e in keV	n_e in 10^{19} m^{-3}	389 nm	447 nm	471 nm	588 nm	707 nm
			$(\Delta I/I)/(\Delta T/T)$ before ITB formation, 0% 2^3S				
3.60 m	1.00 - 3.35	1.20	-0.15	**-0.48**	**-0.64**	**-0.67**	**-0.70**
3.35 m	3.35 - 6.00	1.75	*-0.01*	-0.33	**-0.47**	**-0.59**	**-0.75**
3.12 m	6.00 - 7.70	2.46	*0.00*	-0.19	-0.25	-0.36	**-0.47**
			$(\Delta I/I)/(\Delta T/T)$ before ITB formation, 10% 2^3S				
3.60 m	1.00 - 3.35	1.20	0.17	*0.01*	*0.00*	-0.24	*-0.14*
3.35 m	3.35 - 6.00	1.75	0.20	*0.11*	*0.08*	-0.20	*-0.11*
3.12 m	6.00 - 7.70	2.46	*0.12*	*0.10*	*0.07*	-0.16	*-0.11*
			$(\Delta I/I)/(\Delta T/T)$ after ITB formation, 0% 2^3S				
3.60 m	1.3 - 3.0	1.45	*-0.14*	**-0.45**	**-0.60**	**-0.63**	**-0.67**
3.47 m	3.0 - 6.3	2.50	*-0.03*	-0.33	**-0.45**	**-0.57**	**-0.70**
3.33 m	6.3 - 10.3	3.90	*-0.01*	-0.26	-0.34	**-0.48**	**-0.65**
			$(\Delta I/I)/(\Delta T/T)$ after ITB formation, 10% 2^3S				
3.60 m	1.3 - 3.0	1.45	0.16	*0.03*	*0.01*	-0.21	*-0.12*
3.47 m	3.0 - 6.3	2.50	0.20	*0.11*	*0.09*	-0.18	*-0.09*
3.33 m	6.3 - 10.3	3.90	0.20	0.18	*0.14*	*-0.12*	*-0.06*
			$(\Delta I/I)/(\Delta T/T)$ after ITB formation, 1% 2^3S				
3.60 m	1.3 - 3.0	1.45	0.16	*0.02*	*0.01*	-0.21	*-0.13*
3.47 m	3.0 - 6.3	2.50	0.20	*0.11*	*0.08*	-0.19	*-0.11*
3.33 m	6.3 - 10.3	3.90	0.20	0.17	*0.13*	*-0.13*	*-0.08*

Table 4.8: Relative emission-intensity changes for T_e steps for all considered triplet lines of He beam with 0%, 1% and 10% initial 2^3S fraction, respectively.

would be most suitable which are exclusively or at least predominantly sensitive to either T_e or n_e, as in the case of thermal He beams [36]. For fast He beams (80 keV) there exists one line which is mainly sensitive to n_e, but no line which is predominantly sensitive to T_e.

It is thus expected that the density profile can be derived from the 668 nm line. If the sensitivity of the optical system can be enhanced, also the 492 nm line would be suitable. Once an n_e profile is known it should be possible to calculate the related T_e profile from any line with a sufficiently strong sensitivity to T_e, even if that line is also sensitive to n_e. The 389 nm line is the most sensitive one with respect to T_e. Although its sensitivity is still relatively small, it might be adequate for T_e deduction. He beam emission spectroscopy, being a local diagnostics, could thus have potential in resolving strong local temperature gradients, even if its overall sensitivity to T_e is much weaker than that to n_e. However, appropriate methods to derive T_e- and n_e profiles from measured HeI emission profiles still have to be developed.

Chapter 5

Preliminary Experiments at Tokamaks

In order to assess whether the beam emission profiles of visible HeI lines can serve for a diagnostic for n_e- and T_e profiles, experiments have been performed by Mr. M. Proschek and Dr. H.-D. Falter of this institute at the ASDEX Upgrade ('AUG') tokamak in Germany and the JET tokamak in the UK. For these experiments the existing neutral-beam heating systems were applied to produce fast neutral He-atom beams of a few hundred milliseconds duration. For the measurement of the beam-emission profile, spectrometers dedicated to ion-temperature measurements have been used. The aim of these experiments was to

- verify which He lines have sufficient intensity to be used, to
- measure beam-emission profiles, and to
- compare them with the corresponding profiles calculated with our code.

Ideally, one should use repetitive discharges with no or only little variations in the density- and temperature profiles for the various He emission lines. Furthermore, the discharge should be in steady state during the He-beam injection, thus allowing sufficiently long integration times to identify variations in the beam emission caused by the He injection.

The first experimental attempt to assess the suitability of a fast He beam for beam-emission diagnostics have been made at ASDEX Upgrade. One of the 4 beam sources of one neutral-beam injector was converted from hydrogen to He producing a 30 keV beam with an equivalent neutral-beam current of about 14 A. Helium was injected during some ten discharges. For the experiments at JET, so-called 'doped' beams were produced, i.e. neutral deuterium beams with a small fraction of He atoms. In the next subsections the sequence of these

experiments is described and the most important results are discussed. A more detailed description has already been given in [90].

5.1 Experiments at ASDEX Upgrade

The experiments performed at ASDEX Upgrade ('AUG') in late July and early August 1999 were our first experimental attempt to assess the suitability of a fast He beam as beam-emission diagnostics. For these experiments pure He-atom beams were produced by running one of the neutral beam sources with He instead of deuterium or hydrogen. This was easy to realize as no hardware modifications were required. The drawback of this method is that the beam source used will not be available for plasma heating. Also, He gas accumulates in the neutral-injector box, since it is not pumped by the titanium getter pumps. The rise in partial pressure in the injector box leads to increased losses due to charge-changing collisions and limits the pulse duration of the injector. Hence, the duration of the He beam injection was set to 300 ms or less and He injection could only be performed at the end of a discharge.

AUG has two beam injectors with four beam sources each. The He injection was carried out with source 4 of the so-called 'SO' ('süd ost' in german) injector rated for 60 keV beam energy and 78 A ion-beam current in deuterium per beam source. The source was operated at half the extraction voltage of the other sources of that injector, namely 30 keV and 27 keV, respectively. The so produced neutral He beams had an equivalent injected neutral-beam current of about 14 A.

For the spectroscopic measurements the standard horizontal charge-exchange spectroscopy system ('CER') with 16 lines of sight could be used for plasma discharges in which the measurement of the ion temperature was not required. This condition severely limited the number of discharges available for measurements of the He-beam emission. To overcome this limitation 3 spare fibres from the CER diagnostic which viewed the plasma near the plasma center where routed to a second spectrometer from the Li-beam diagnostic. Initially this spectrometer was used to identify the most intense He lines. However, it turned out that the intensity of the Doppler-shifted He line was weak, and in order to distinguish this line from other unshifted peaks at this wavelength one has to verify that the Doppler shift varies with the viewing angle. Later on, it was also discovered that the preamplifier of this spectrometer was faulty. As a consequence only the measurements with the CER spectrometer were suitable for evaluation. The measured spectra are usually analysed by a fitting routine using

a Gaussian distribution to fit the Doppler-shifted intensity after applying a linear background subtraction. The error bars in the figures showing the experimental results (figures 5.4 to 5.7) represent the quality of these fits.

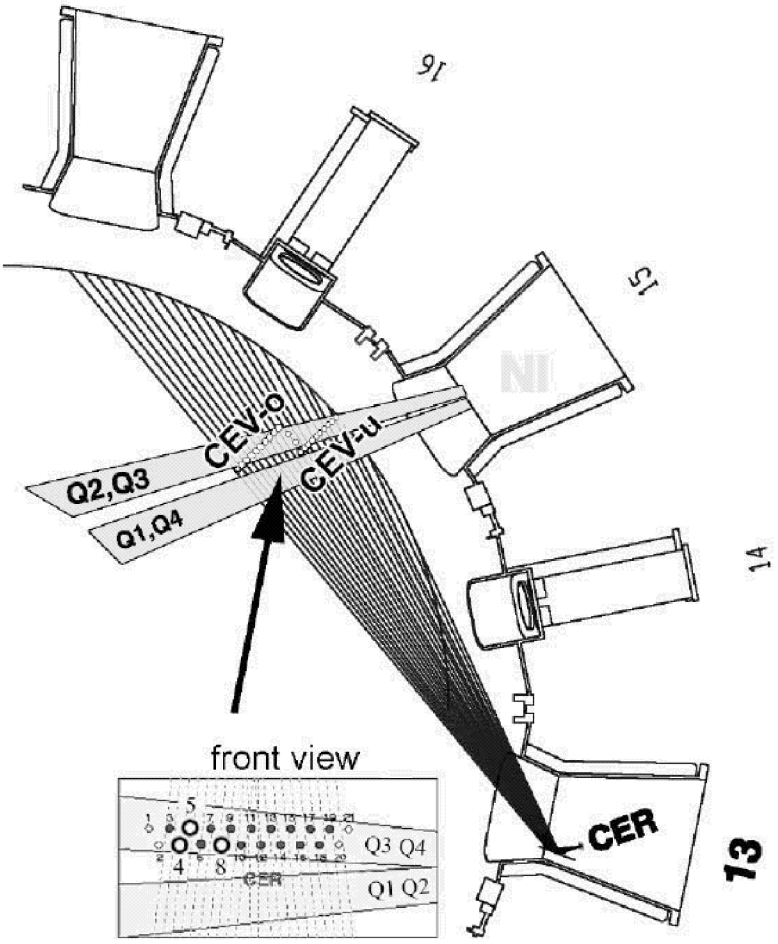

Figure 5.1: Top view of the schematics of the CER diagnostic system at ASDEX Upgrade. The black lines denote the lines of sight, the grey bars denote the four heating-beam paths (Q_1 to Q_4). The position of the lines of sight vs. beam path is also shown in front view. The fibres for the CER diagnostic are marked by dots, those for the Li-beam diagnostics are marked by open circles.

The geometry of the CER spectroscopic system is shown in figure 5.1. The fibres of the CER diagnostic view the plasma from the edge to the plasma center. The angles between the lines of sight used for the experiments and the beam are given in table 5.1. Near the scrape-off layer the viewing angle is close to 90°. Hence, the Doppler shift for the fibres viewing the plasma edge (#18 and #19) is too small to be resolved satisfactory, consequently these data points have been left out of the analysis.

line of sight	major radius	viewing angle
#3	1.67 m	74.6°
#6	1.77 m	77.0°
#7	1.80 m	77.6°
#9	1.86 m	79.1°
#10	1.89 m	79.9°
#11	1.92 m	80.6°
#12	1.96 m	81.5°
#13	1.98 m	82.1°
#14	2.02 m	83.0°
#15	2.05 m	83.6°
#16	2.08 m	84.4°
#17	2.11 m	85.1°
#18	2.14 m	85.9°
#19	2.17 m	86.6°

Table 5.1: Viewing angle between the lines of sight and the He beam and major radius of the beam segment viewed by the fibres of the CER diagnostic system used for the first experiments at ASDEX Upgrade.

The intensity of the Doppler-shifted peaks is about by one order of magnitude lower than that of the corresponding unshifted peaks of all observed wavelengths for all lines of sight. The unshifted He emission originates from He gas in the plasma edge as thermalized He atoms can not penetrate deeper into the plasma. The majority of these He atoms in the plasma edge do not originate from the He beam, as the unshifted emission starts well before He gas is released into the injector. One possible source for this He is the first wall, which is subjected to He glow-discharge cleaning between most of the discharges.

The experiments provided three discharges in which the He-beam emission spectra could be evaluated, namely #12635 with 502 nm, #12643 with 588 nm, and #12644 with 668 nm. All three discharges have been performed with hydrogen plasmas. The last two discharges where almost identical ohmic plasmas with some ECR heating at 3 s and He injection at 4.2 s - 4.5 s after plasma initiation. During discharge #12635 the plasma was mainly heated by neutral-beam injection. The He beam was injected at 4.8 s - 5.1 s after plasma initiation. The T_e- and n_e profiles used for the model calculations (figures 5.2 and 5.3) are taken from Thomson scattering measurements. Table 5.2 shows the He-beam parameters used for calculation of the line-emission profiles for the three presented discharges.

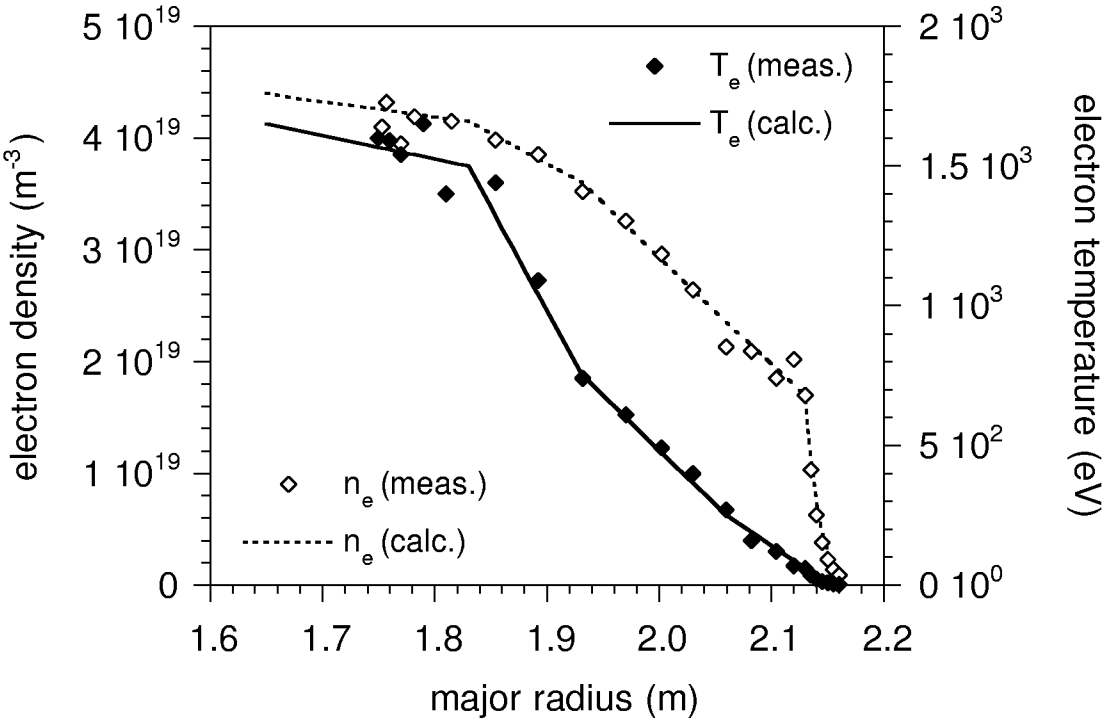

Figure 5.2: T_e and n_e profiles of AUG discharge #12643: Thomson scattering results (diamonds) and therefrom derived profiles used for model calculations (lines).

discharge number	equivalent beam current	beam energy	measured wavelength	corresponding transition
12635	14.2 A	27 keV	502 nm	$3^1P \rightarrow 2^1S$
12643	14.2 A	27 keV	588 nm	$3^3D \rightarrow 2^3P$
12644	14.2 A	27 keV	668 nm	$3^1D \rightarrow 2^1P$

Table 5.2: Discharge number, beam parameters and observed wavelength of the three evaluable measurements at ASDEX Upgrade.

The He beam is inclined by 10.84° in the horizontal plane and 4.9° in the vertical plane, and the beam-path increment is therefore not equal to that of the major radius. The model calculations are performed following the beam-interaction length L_{bi}. n_e- and T_e profiles are being mapped onto L_{bi}. The axis of the AUG vacuum vessel is located at $R_{maj} = 1.65$ m for the presented experiments, the outer separatrix at $R_{maj} = 2.11$ m for #12635 and at $R_{maj} = 2.13$ m for #12643 and #12644.

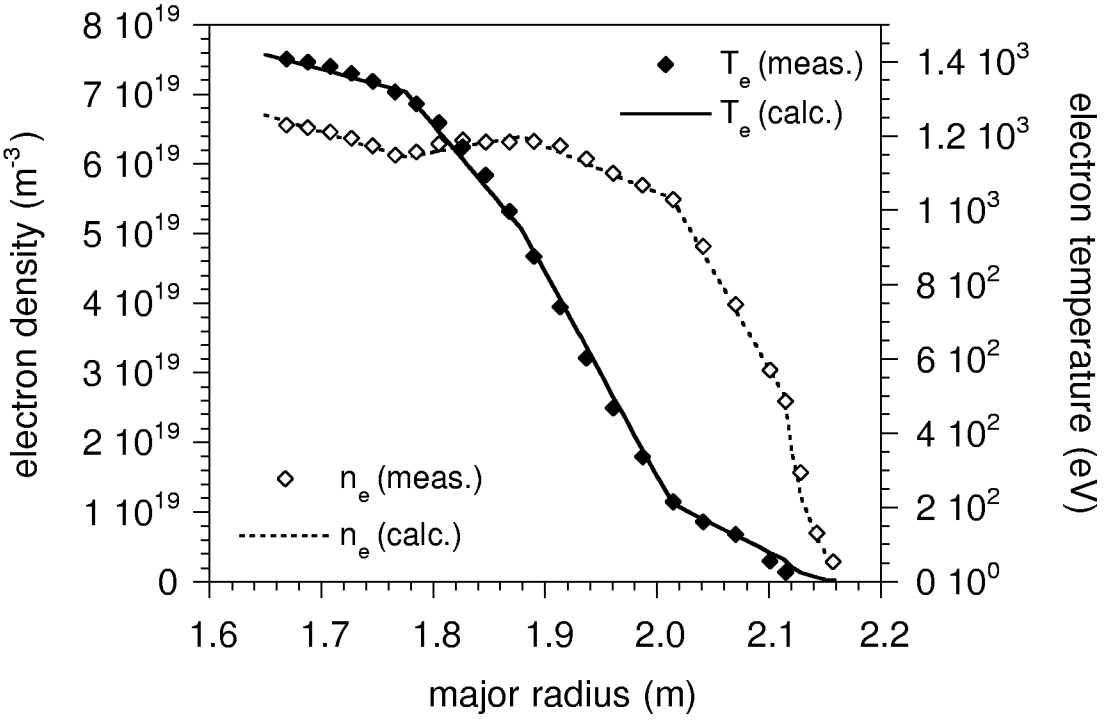

Figure 5.3: T_e and n_e profiles of AUG discharge #12635: Thomson scattering results (diamonds) and therefrom derived profiles used for model calculations (lines).

The minimum distance between the beam axis and the various lines of sight are staggered and slightly offset against each other, see figure 5.1 (front view). This means that the beam intensity is different, depending on this distance. The exact width of the AUG He beam is not known. In this paper we assume a Gaussian profile with a divergence of 0.9° which corresponds to a fall-off length of 120 mm. Moving from the plasma center to the edge, the distance between beam axis and the lines of sight increases. The measured beam emission signal I_ν from line of sight ν has therefore to be corrected by a factor f,

$$f = e^{\frac{\Delta^2}{\lambda^2}}, \tag{5.1}$$

where Δ gives the offset between beam axis and lines of sight and λ the fall-off length of the beam. The correction is small for $\Delta \ll \lambda$. If Δ becomes comparable to λ, as in the case for the outer lines of sight, the correction becomes significant and is critically dependent on the exact knowledge of the beam alignment and the beam profile. As an illustration of the sensitivity of the correction factor to the alignment of the beam, table 5.3 shows f for several examples of beam divergence for one line of sight with the smallest distance to the beam axis (#6) and for one line of sight with a large distance to the beam axis (#17).

It can be seen that the correction for lines of sight in the plasma center are not much affected by uncertainties in the beam divergence, whereas the correction for lines of sight near the plasma edge is very sensitive to such changes. In addition to this effect also the uncertainty in the beam alignment leads to a much bigger error for the lines of sight near the plasma edge than for the ones in the plasma center.

line of sight	Δ in mm	f (0.9°)	f (1.1°)	f (0.7°)
#6	15	1.016	1.011	1.027
#17	97	2.030	1.606	3.223

Table 5.3: Distance between beam axis and lines of sight (Δ) and correction factor f for three different values of the beam divergence for the line of sight with the smallest Δ (#6) and with a large Δ (#17).

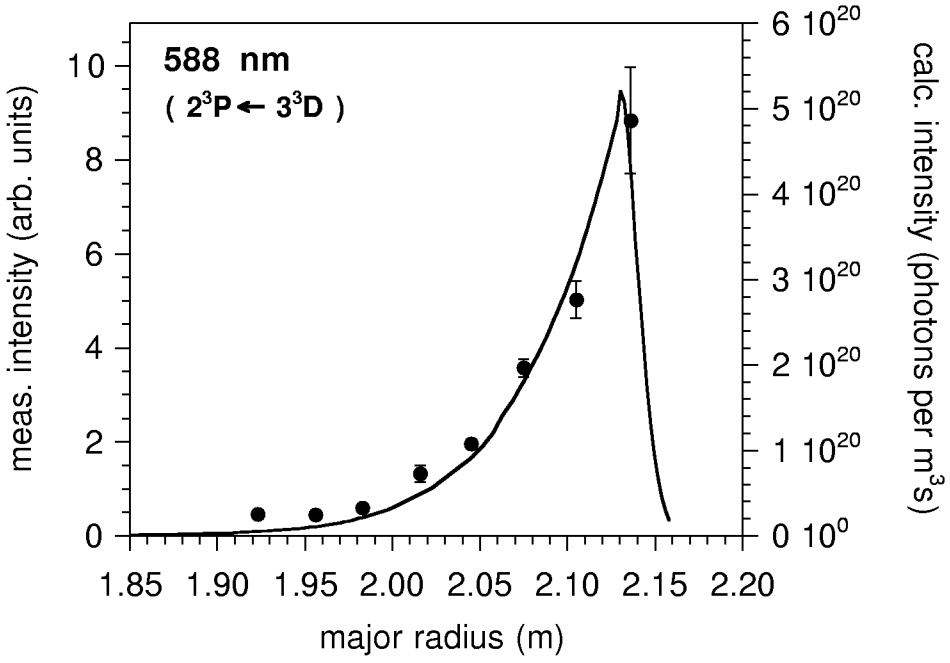

Figure 5.4: Comparison of measured (black circles) and calculated (solid line, based on T_e- and n_e profiles shown in figure 5.2, assuming 2% 2^3S fraction) line emission at 588 nm for AUG discharge #12643.

Figures 5.4 and 5.5 show comparisons of measured and calculated line intensity profiles for discharges #12643 and #12644 assuming an initial 2^3S fraction of 2%.

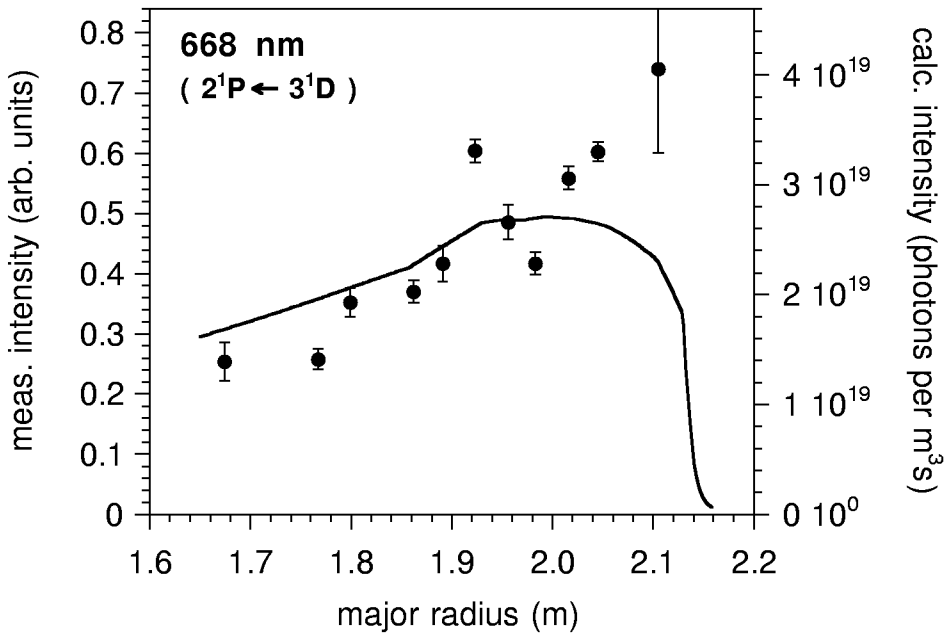

Figure 5.5: Comparison of measured (black circles) and calculated (solid line, based on T_e- and n_e profiles shown in figure 5.2, assuming 2% 2^3S fraction) line emission at 668 nm for AUG discharge #12644.

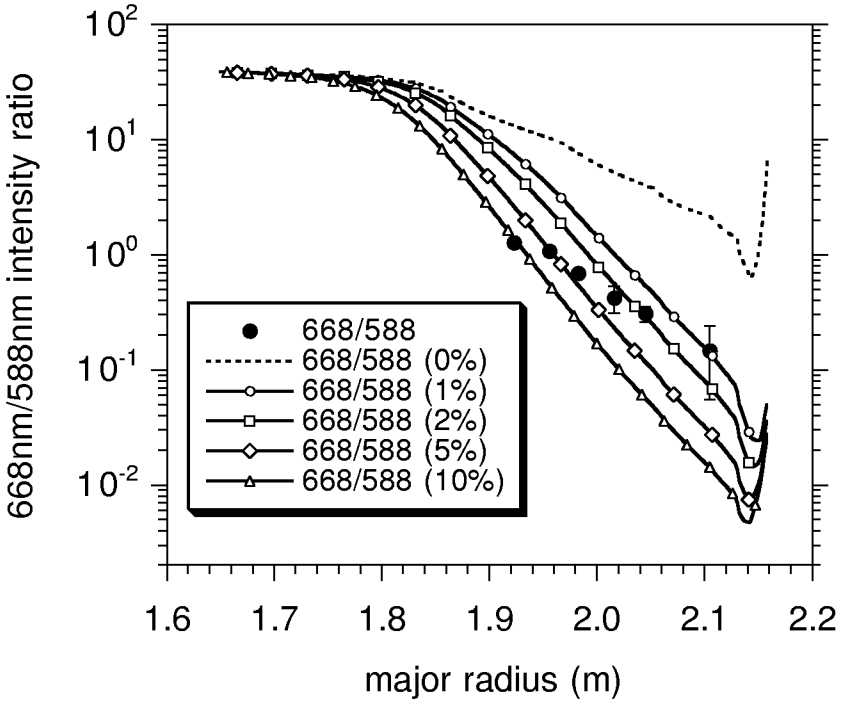

Figure 5.6: Comparison of measured (black circles) and calculated (solid lines, based on plasma profiles shown in figure 5.2, assuming 0%, 1%, 2%, 5%, and 10% initial 2^3S fraction) 668 nm/588 nm line-intensity ratio for AUG discharges #12644 and #12643, respectively.

As already mentioned, the error bars displayed in the figures are a measure for the quality of the fit of the Doppler-shifted peaks only. The large error bar for the outermost point can be explained by the insufficient separation between shifted and unshifted peak. An additional error for the outermost points is possible because of their sensitivity to beam alignment and beam profile, as described above. The observed emission lines are well represented by the model calculations.

As the line-intensity ratios between emission lines of different spin systems is rather sensitive to the initial metastable fraction, the measured 668 nm/588 nm line-intensity ratio has been compared to the corresponding calculated ones for several initial metastable fractions, see figure 5.6. Once again, an initial 2^3S fraction of about 2% seems to be appropriate.

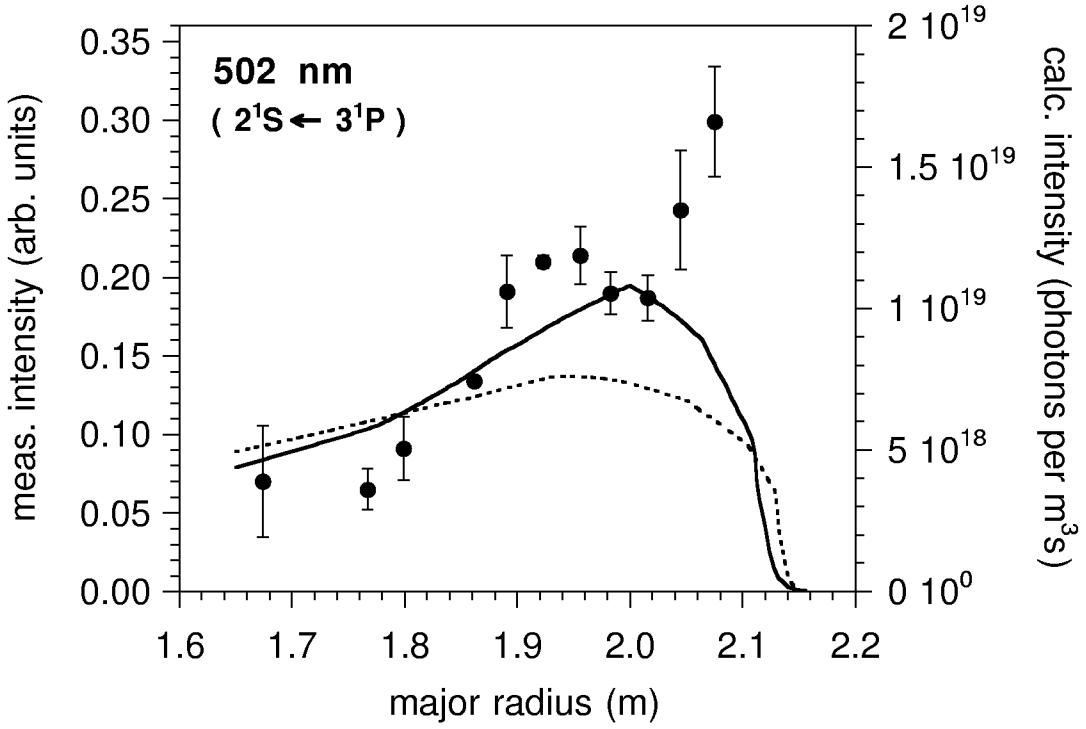

Figure 5.7: Comparison of measured (black circles) and calculated (solid line, based on T_e- and n_e profiles shown in figure 5.3, assuming 2% 2^3S fraction) line emission at 502 nm for AUG discharge #12635. In addition, the calculated 502 nm emission based on the n_e- and T_e profiles of discharge #12643 shown in figure 5.2 (broken line) is displayed.

Figure 5.7 shows a comparison of measured and calculated line intensities at 502 nm for discharge #12635 (based on T_e- and n_e profiles shown in figure 5.3). To illustrate the sensitivity of the calculated emission profile to the input parameters (n_e- and T_e profiles), we show a second 502 nm-emission profile in the calculated profile in figure 5.7.

For this second profile we used the data from discharge #12643 (cf. figure 5.2) instead of that from discharge #12635 (cf. figure 5.3) as input parameters for the modelling. This results in an obvious mismatch between measured and calculated profile. The observed emission line is well represented by the calculation using the correct input files.

5.2 Experiments at JET

The tokamak JET (Joint European Torus) is according to its plasma volume by one order of magnitude larger than AUG, but has about the same heating power in the neutral injection system. Because of this clear lack in heating power the loss of beam power caused by conversion of a beam source to He gas was not acceptable. This led us to the concept of a so-called 'doped' beam, where He gas is temporarily injected additionally to H into a heating-beam source. This was achieved by modifying the gas-inlet system of one of the heating-beam sources. The addition of a He minority (about 10%) does not cause a measurable reduction in heating power which was a prerequisite for carrying out He-injection experiments at JET. These experiments have taken place in mid October and at the beginning of December 1999.

Like AUG, JET has two heating-beam injection systems, one in octant 4 and the other one in octant 8. For our experiments we used PINI 6 of the injector in octant 4 which is rated for 80 keV deuterium beams with 50 - 55 A extracted beam current. By injecting a small flux of He into the ion source operating with deuterium, a He beam with an energy of 75 keV and about 4 A equivalent current was produced. The addition of He had no measurable effect on the beam quality and the transmitted power in the beam-injection system [90]. The He injection has no measurable influence on the impurity level of the plasma as the time trace of Z_{eff} shows no change during He injection. Hence, the doped beam was used at JET on a routine basis. The heating beam was doped with He for 0.5 s at the beginning of the so-called 'flat-top phase' of the discharge, i.e. the phase in which all major plasma parameters (T_e, n_e, heating power, toroidal field, plasma current, etc.) are about constant.

The emission of the He beam was measured with the so-called 'KS7' [93] normally dedicated to ion-temperature measurements. The lines of sight of KS7 are aligned to the beam of PINI 4, but they also cross the beam of PINI 6. The spectrometer on KS7 is optimized for the CVI ($n = 8 \rightarrow 7$) transition at 5291 Å. KS7 uses two spectrometers in series with the first spectrometer acting as a narrow bandwidth filter. If used at wavelengths away from 5291 Å the spectrometer has only its full sensitivity for a narrow band with a considerable reduction

in sensitivity to either side. Attempts have been made to correct this by multiplying the measured signal with a factor compensating the loss in sensitivity. This factor has been obtained by calibrating the spectrometer. So far this procedure is not satisfying and leads to a large scatter in the measured data.

The geometry of the spectroscopic system - consisting of lines of sight viewing top-down ('upper chords') and lines of sight viewing bottom-up ('lower chords') - is shown in figure 5.8.

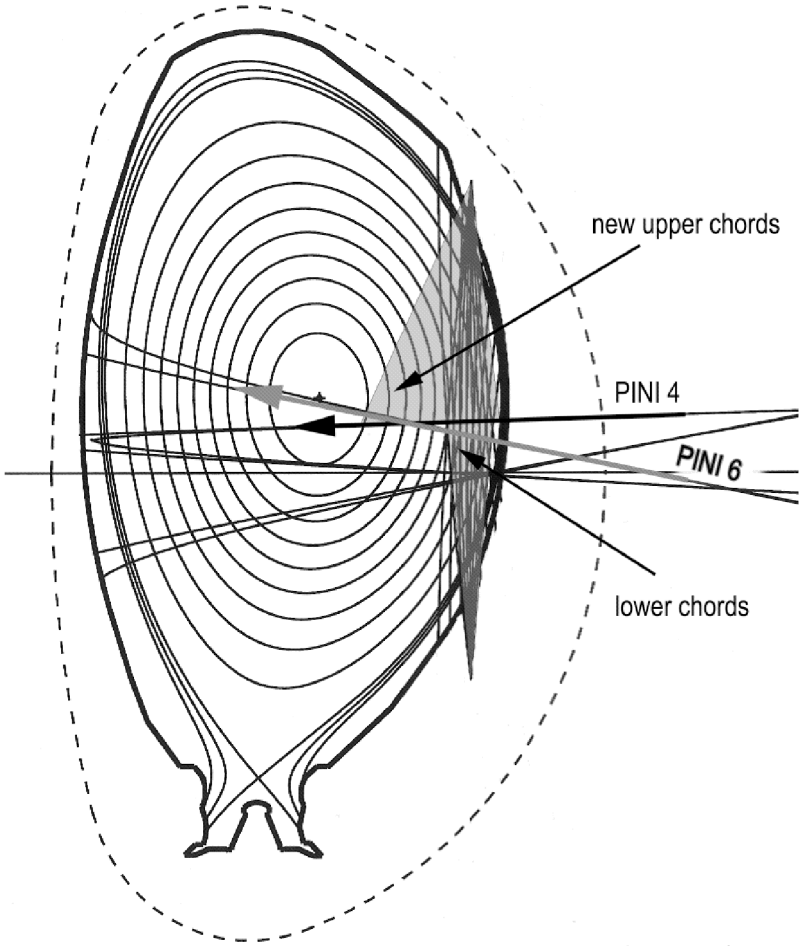

Figure 5.8: Geometry of the spectroscopic system used during the experiments at JET. The grey triangles denote the lines of sight, and the line inscribed with 'PINI 6' denotes the He-beam path.

The upper chords, installed during the 1999 shutdown, cover a larger range of the beam path (major radius R_{maj} 3.19 to 3.90 m). These lines of sight have not yet been end-to-end calibrated and only cross-calibrated with the calibrated lower chords. The width of one line of sight at the location of the beam path is about 10 mm for the lower and 50 mm for the

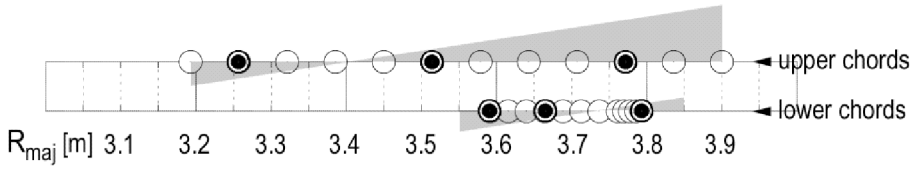

Figure 5.9: Positions of the intersections of the lower and upper chords of KS7 with the beam path of PINI 6 at JET. The grey triangles denote the Doppler shift of the lines of sight.

upper chords. The Doppler shift is zero for the upper chords at $R_{maj} = 3.4$ m and for the lower chords at $R_{maj} = 3.75$ m, which is illustrated in figure 5.9, because at these positions the angle between the lines of sight and the beam is 90°. For some fibres near these positions it was not possible to separate the Doppler-shifted- from the unshifted emission.

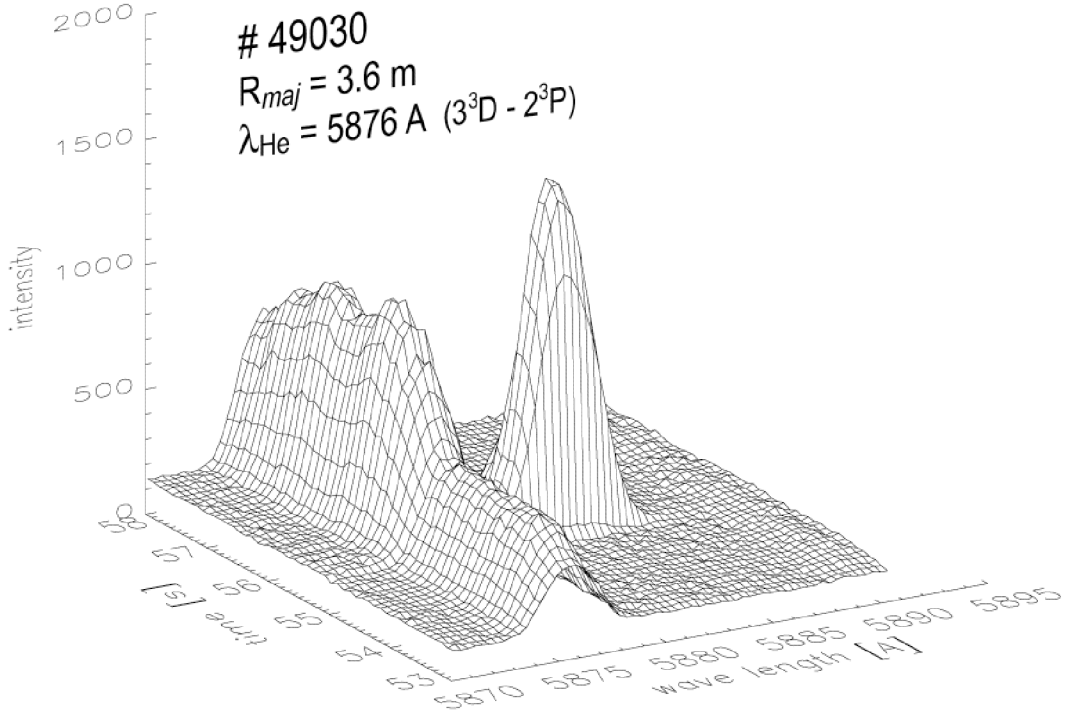

Figure 5.10: Measured intensity spectrum for discharge #49030 in the wavelength region 5870 Å to 5895 Å.

The recorded spectra contain an unshifted intensity and a Doppler-shifted intensity as shown in figure 5.10. As already mentioned in chapter 5.1, the unshifted intensity originates from He atoms in the plasma excited by collisions with other plasma particles. The penetration depth of neutral He is essentially limited to the scrape-off layer where the unshifted intensity must therefore come from. Hence, the intensity of the unshifted radiation is proportional to the gas density in the scrape-off layer. A possible correlation of the unshifted peak with the heating beam can only exist via the energy dependence of the excitation cross sections. The Doppler-shifted intensity originates from fast He atoms in the beam. This intensity is therefore correlated to the timing of the He-beam injection.

The measured data was analyzed in two different ways. If possible, Gauss functions are fitted to both shifted- and unshifted peak, using a suitable subtraction of the background intensity. The intensity of the He beam emission is then calculated from the respective fit parameters. If the Doppler shift becomes so small that the two peaks cannot be resolved, this procedure fails and the second method - the time-trace method - is used. The measured intensity trace of the wavelength-integrated signal consists of Doppler-shifted- and background intensity (including the unshifted peak). Before He injection the intensity is essentially constant, rises during He injection and settles to a new equilibrium value after He injection, see figure 5.10. Before and after He injection all the intensity must originate from the background radiation. It is assumed that this radiation changes its intensity during He injection as the He-background pressure changes. The time constant of that change is assumed to be the same as the time constant of the pressure change in the injector. With this assumption the progression of the background signal during He injection can be obtained. The beam emission signal is the difference between background signal and measured emission trace, as illustrated in figure 5.11.

During our experimental campaign at JET, spectra for the singlet lines at 668 nm and 502 nm, and for the triplet lines at 588 nm, 389 nm, 707 nm, and 447 nm were taken. For 397 nm, 471 nm, and 728 nm the signals were too small to be analysed.

Two discharges, namely #49030 (L-mode) with 668 nm and #49504 (H-mode) with 588 nm are presented in this section. The T_e- profiles used for the model calculations (see figures 5.12 and 5.13) were taken from ECE measurements, the n_e profiles from JET ppf (processed pulse file) NFT2/PROF, i.e. a composition of LIDAR and infrared interferometry (KG1) data. Table 5.4 shows the He-beam parameters used for calculation of the line-emission profiles for the regarded discharges.

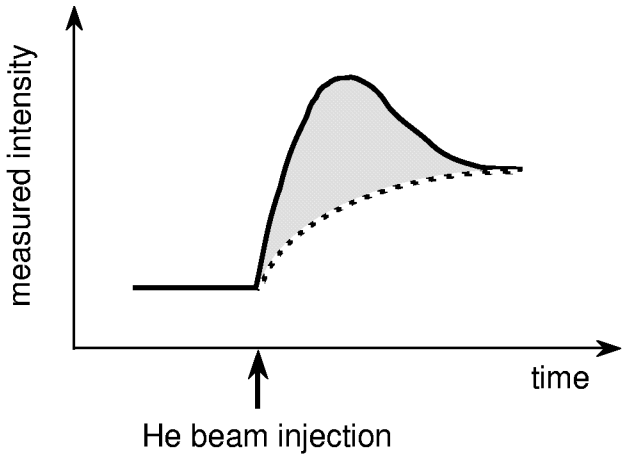

Figure 5.11: Illustration of the time-trace method for determination of the He-beam emission. The intensity of the signal emitted from the He beam (grey area) is obtained by subtracting the background signal (deduced from measurement of the pressure change in the injector, broken line) from the measured emission trace (solid line).

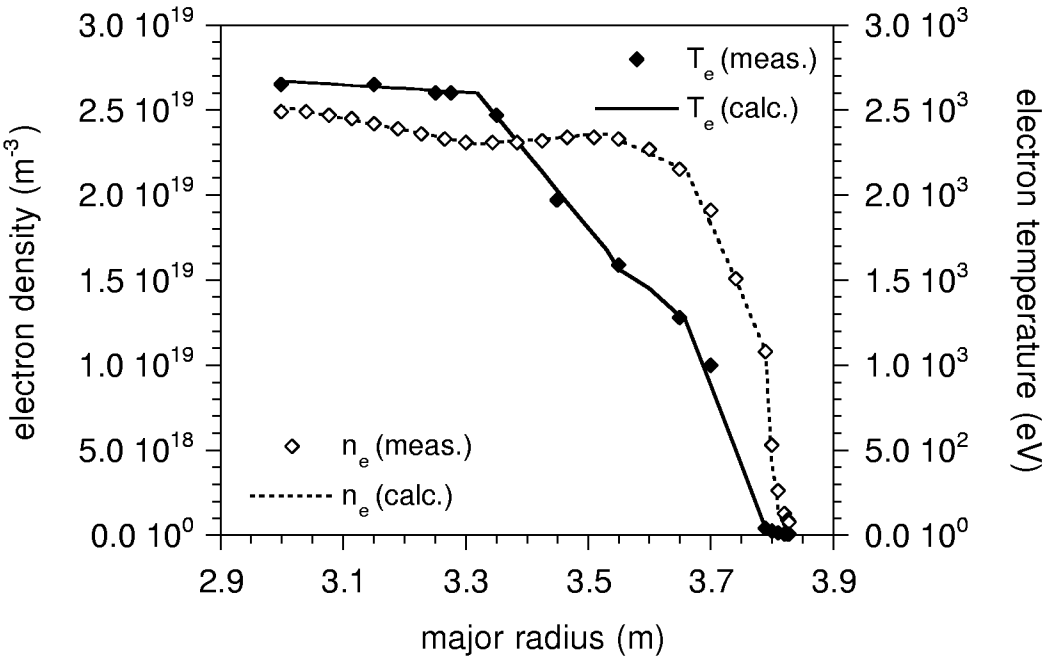

Figure 5.12: T_e and n_e profiles of JET discharge #49030: ECE-, LIDAR- and interferometry measurement results (diamonds) and therefore derived profiles which have been used for model calculations (lines).

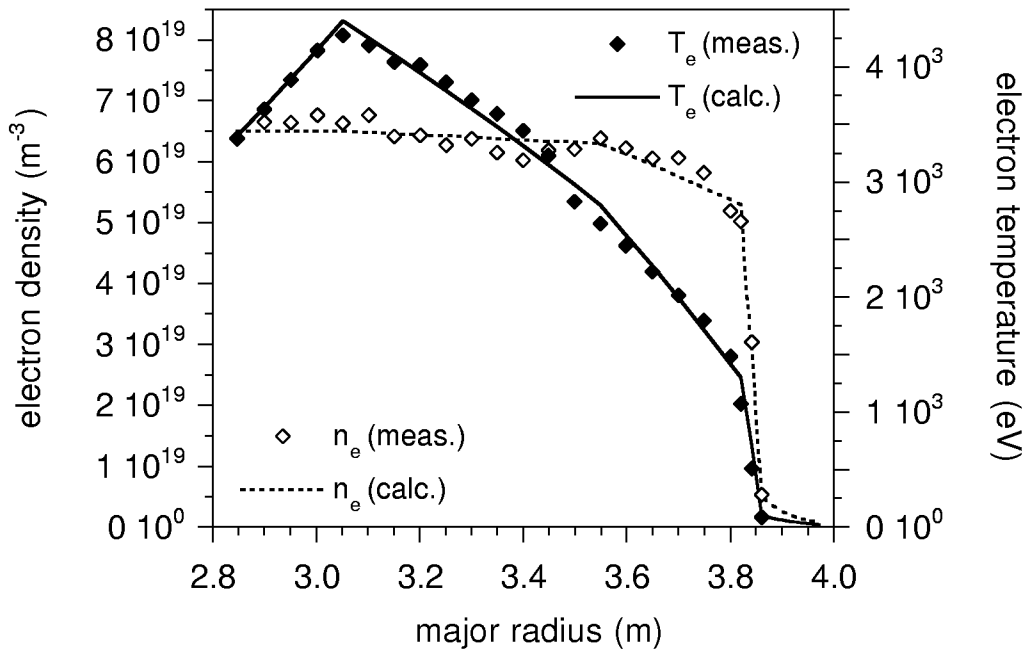

Figure 5.13: T_e and n_e profiles of JET discharge #49504: ECE-, LIDAR- and interferometry measurement results (diamonds) and therefore derived profiles which have been used for model calculations (lines).

discharge number	equivalent beam current	beam energy	measured wavelength	corresponding transition
49030	4 A	75 keV	668 nm	$3^1D \rightarrow 2^1P$
49504	4 A	80 keV	588 nm	$3^3D \rightarrow 2^3P$

Table 5.4: Discharge number, beam parameters and observed wavelength of the presented measurements at JET.

The spectra taken at JET show a higher ratio between shifted and unshifted intensity. In particular, the intensity of shifted triplet lines can exceed that of the unshifted line (see figure 5.10). The reason for this more favourable ratio is, on the one hand, the higher percentage of metastable atoms in the incident beam, since hydrogen gas instead of He is used for neutralization of the He-ion beam. On the other hand, the unshifted peak shows a lower intensity because the He-atom partial pressure in the plasma edge is lower than at AUG.

Due to the inclination of the beam against the radial direction (10° in horizontal- and 22.1° in vertical direction), the beam-path increment is not equal to the major-radius increment.

As already explained in section 5.1, a correction for the penetration depth compared to R_{maj} had to be applied. The values of R_{maj} and the corrected beam-path parameter L_{bi} at the separatrix and in the center of the plasma for the two presented discharges are given in table 5.5.

discharge number	R_{maj} at separatrix	L_{bi} at separatrix	R_{maj} at plasma center	L_{bi} at plasma center
49030	3.79 m	43 mm	3 m	1.004 m
49504	3.86 m	100 mm	3 m	0.710 m

Table 5.5: Major radius (R_{maj}) and beam-interaction length (L_{bi}) at the position of the separatrix and the plasma center for the two presented discharges.

Figures 5.14 to 5.15 show comparisons of measured and calculated line intensity profiles for these discharges, assuming an initial 2^3S fraction of 10%. As with the AUG experiments, the observed emission lines are well represented by the model calculations.

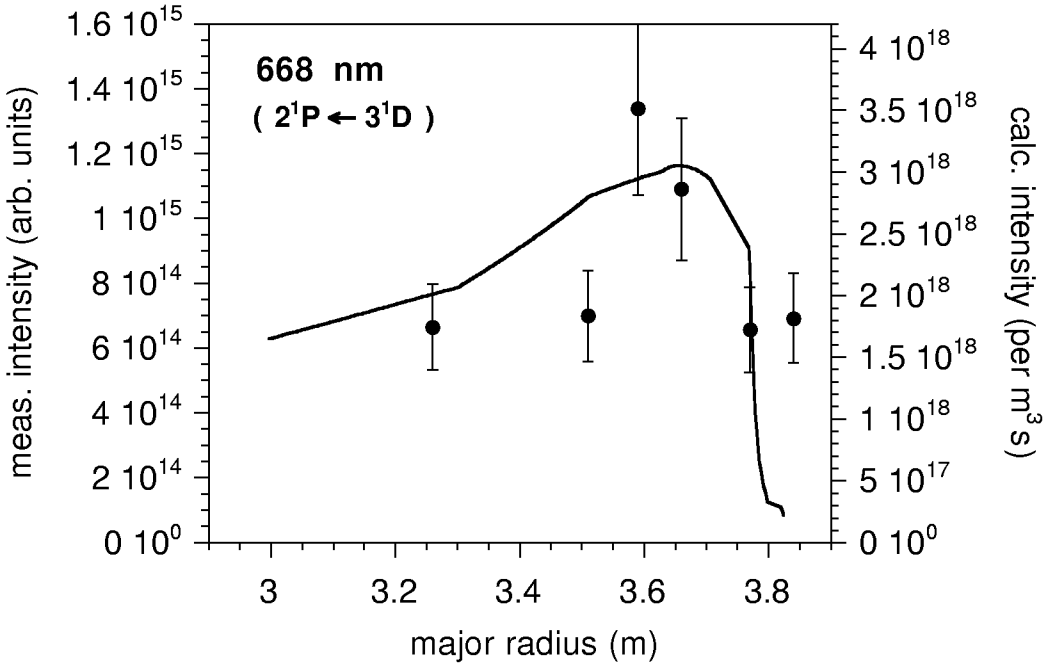

Figure 5.14: Comparison of the measured (circles) and calculated (solid line, assuming 10% 2^3S fraction) line emission at 668 nm for JET discharge #49030.

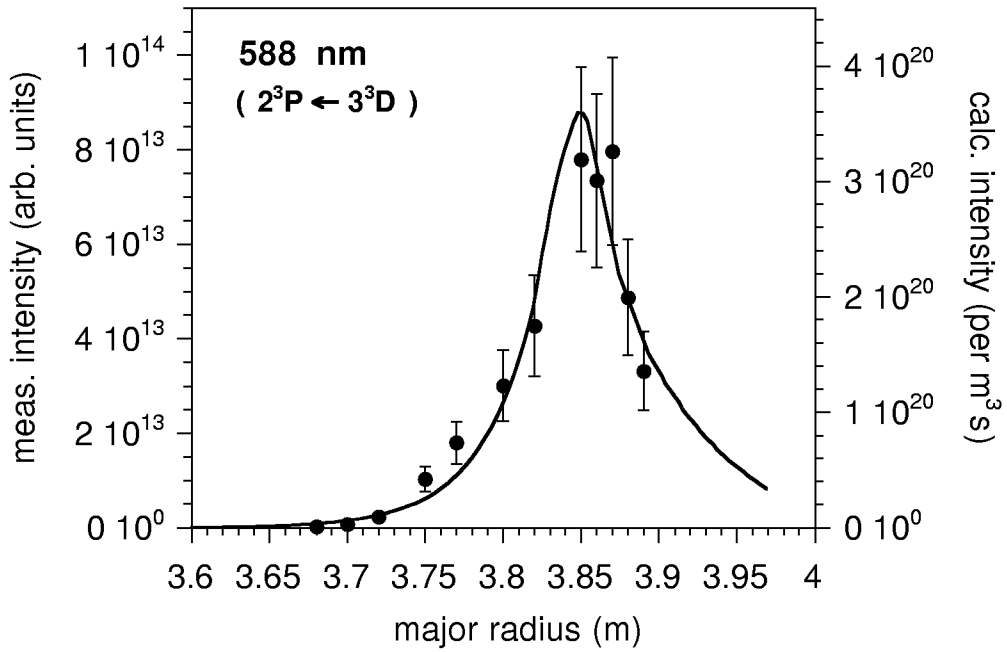

Figure 5.15: Comparison of the measured (circles) and calculated (solid line, assuming 10% 2^3S fraction) line emission at 588 nm for JET discharge #49504.

5.3 Conclusions from the Experiments

The concept of the pure He beam at AUG and the doped He beam at JET worked successfully, enabling for He beam-emission spectroscopy without major capital investment and without impeding the reliability and power of the neutral-beam heating systems. The intensities of the He-beam emission obtained from both He beams is sufficiently large to permit meaningful measurements for both HeI singlet- and triplet lines in the plasma. Comparison between measurement and model calculations show a favourable agreement. However, more effort is required to improve the mapping of the beam emission to the flux surfaces and to extend the evaluation to such measurements with better spatial resolution for the outer part of both AUG and JET plasmas.

During the second experimental phase at AUG - performed in May 2000 - also there a doped He beam has been used. For these measurements PINI 3 was utilized with the advantage of having a more favourable angle which allows for all lines of sight to separate the Doppler-shifted beam emission from the unshifted background emission. These experimental results are now being evaluated, but are not discussed in the course of this thesis.

Summary, Conclusion, and Outlook

In order to investigate the diagnostic potential of fast He beams, extensive modelling calculations have been performed for a fast He beam penetrating a plasma which resulted in the progression of He ground state- and metastable-states populations and the related intensity profiles of visible HeI lines. The calculations are based on the collisional-radiative model for He beams developed by the ADAS group at the University of Strathclyde, Glasgow [1]. We used typical electron density- and temperature profiles from ASDEX Upgrade and JET. He beam energies of 30 keV (AUG) and 80 keV (JET) were chosen to match those used for first experiments at these tokamaks. Calculations have been performed for the extreme cases of incident pure ground state- and pure 2^3S beams, respectively. The results for realistic beams with an initial metastable fraction between these extremes can be determined by mixing the two results with the corresponding weight factors. The calculations showed that the 2^1S-population density is strongly coupled to the 1^1S-population density, whereas the 2^3S-level is preferably populated in regions with low electron temperature (near the outer and inner separatrices), but strongly depopulated in the hot core. In an initially pure ground-state beam the 2^1S fraction reaches about 10^{-4} near the separatrix and drops slightly inside the core, whereas the 2^3S fraction reaches 10^{-5} (JET) or 10^{-4} (AUG) near the separatrix and drops by about one order of magnitude in the core. For an initially pure 2^3S beam the progression of the 2^1S-population density is dominated by the 2^3S-population density in the region where the 2^3S concentration outnumbers the ground-state concentration. The line-intensity profiles of both spin systems resemble the corresponding metastable population-density profiles.

The attenuation of a 80 keV He beam penetrating a hot, dense and rather large JET H-mode plasma is much weaker than that of a 30 keV He beam injected into a cooler and less dense ASDEX Upgrade L-mode plasma with its considerably smaller dimension. In the case of AUG, the beam composition reaches equilibrium after about 0.3 m and becomes independent of the initial beam composition. The initial beam composition is therefore unimportant for the emission from the plasma core. In the case of JET, the 2^3S-fraction does not reach saturation. Here, at each position along the path of the beam its composition is still influenced by the initial composition.

In order to assess the potential of He-beam emission spectroscopy as useful plasma temperature and -density diagnostics, we have examined the sensitivity of visible HeI lines with

respect to n_e and T_e. The calculations were performed for an 80 keV He beam penetrating a JET discharge which develops an internal transport barrier.

Basically all singlet lines are rather sensitive to density variations. The sensitivity is highest in the edge and drops towards the plasma center. The 502 nm-, 668 nm-, and 492 nm lines are the most sensitive ones with respect to density and show only small variations in both edge- and core region. In the case of a pure ground-state beam the singlet lines are more sensitive with respect to temperature variations than to density variations in the outermost edge region, but this temperature sensitivity is dramatically reduced towards the separatrix and inside the core. An increase in the initial 2^3S fraction results in a strong decrease in the temperature sensitivity of all singlet lines in the plasma edge - the lines at 492 nm and 668 nm lose their sensitivity to T_e almost entirely. Additionally to its favourable sensitivity to n_e and relatively small sensitivity to T_e, the 668 nm line is also the strongest singlet line. This makes the 668 nm line the prime candidate for n_e measurements. If the sensitivity of the optical system can be enhanced, also the 492 nm line would be suitable.

To deduce T_e profiles from line emission profiles, lines which are mainly sensitive to T_e would be desireable. Some of the triplet lines are rather sensitive to T_e for an initially pure ground-state beam. This sensitivity decreases strongly with increasing initial 2^3S fraction. The singlet line at 728 nm shows as well a relatively strong sensitivity to T_e. Unfortunately, none of the lines is mainly sensitive to temperature as all lines have a high sensitivity to density. The 389 nm line is the most sensitive one with respect to T_e, with a sensitivity of about 60% in the outermost part of the plasma edge, i.e. a 100% increase in temperature results in a 60% increase in emission intensity. This is reduced to a 20% sensitivity in the plasma center. The favourable sensitivity to density together with the 'stiffness' of temperature profiles observed in various tokamak experiments should result in a good first approximation for the density profile from the 668 nm emission profile. If this density profile is sufficient, it will permit the calculation of an improved temperature profile from the 389 nm line emission profile. This procedure can be iterated and is expected to converge to a selfconsistent solution.

To validate the model calculations, data have been considered from experiments with fast He beams and beam emission spectroscopy performed at ASDEX Upgrade and JET, making use of the respective neutral beam heating systems. The intensities of the He-beam emission obtained from either experiment are sufficiently large to permit meaningful measurements with both HeI singlet- and triplet lines in the plasma. Comparison between measurements and model calculations shows a favourable agreement.

The calculations performed in this thesis and preliminary experiments at tokamak plasmas guided by these calculations have confirmed that fast He beams may serve for a useful plasma temperature- and -density diagnostics.

Recently, a new version of the collisional-radiative ADAS model has been developed which treats all levels up to n=5 as non-equilibrium levels. This work is going on and should allow for still more accurate calculations, especially for large plasma-parameter gradients. It is also intended to improve and update the fundamental atomic collision data in ADAS, which should lead to a better accuracy of the here derived density- and temperature profiles.

Bibliography

[1] H.P. Summers, *Atomic Data and Analysis Structure*, User Manual, Internal Report, JET-IR (94) 06, JET Joint Undertaking, UK (1994)

[2] E. Wolfrum *et al.*, Rev. Sci. Instrum. **64** (1993) 2285

[3] R. Brandenburg, *Lithiumstrahldiagnostik von Kernfusionsplasmen*, PhD thesis, TU Wien (1998)

[4] Annual Report 1998, EUR 19252-EN-C (EUR-JET-AR21), JET Joint Undertaking, UK (1999)

[5] M. Keilhacker, Plasma Phys. Control. Fusion **41** (1999) B1-B23

[6] B. Unterberg *et al.*, Plasma Phys. Control. Fusion **39** (1997) B189-B206

[7] P.E. Vandenplas *et al.*, J. Plas. Phys. **59** (1998) 587-610

[8] C. Gormezano, Plasma Phys. Control. Fusion **41** (1999) B367-B380

[9] P. Breger *et al.*, Plasma Phys. Control. Fusion **40** (1998) 347-359

[10] X. Litaudon *et al.*, JET-P(98)41, JET Joint Undertaking, UK (1998)

[11] U. Schumacher, *Tokamaks*, Clarendon Press, Oxford (1997)

[12] J. Wesson, *Fusionsforschung: Eine Einführung*, Wiss. Buchges., Darmstadt (1993)

[13] http://www.psfc.mit.edu/cmod/

[14] H.D. Falter, private communication (2000)

[15] C.W. Gowers *et al.*, Rev. Sci. Instrum. **66** (1995) 471-475

[16] W. Suttrop, A.G. Peeters, IPP-Report, IPP 1/306, Garching, Germany (1996)

[17] *ITER final design report, cost review and safety analysis (FDR) and relevant documents International Thermonuclear Experimental Reactor*, ITER EDA Documentation Series, IAEA, Vienna, Austria (1999)

see also: http://www.iter.org/

[18] P.E. Stott and A.E. Costley, JET-P(89)68, JET Joint Undertaking, UK (1989)

[19] J. Schweinzer, private communication (2000)

[20] E. Hintz and B. Schweer, Plasma Phys. Control. Fusion **37** (1995) A87-A101

[21] R.C. Isler, Plasma Phys. Control. Fusion **36** (1994) 171-208

[22] W. Mandl, R.C. Wolf, M.G. von Hellermann, and H.P. Summers, Plasma Phys. Control. Fusion **35** (1993) 1373-1394

[23] M. von Hellermann *et al.*, Plasma Phys. Control. Fusion **33** (1991) 1805-1824

[24] H. Anderson *et al.*, submitted for publication in Plasma Phys. Control. Fusion in 2000

[25] B. Wolle, IPP-Report, IPP III/222, Garching, Germany (1997)

[26] T. Morisaki *et al.*, J. Phys. Soc. Japan **65** (1995) 133-138

[27] I.L. Beigmann, G. Kocsis, A. Pospieszczyk, and L.A. Vainshtein, Plasma Phys. Control. Fusion **40** (1998) 1689-1705

[28] A.I. Ledyankin *et al.*, Physics Letters A **230** (1997) 209-217

[29] J. Schweinzer *et al.*, Plasma Phys. Control. Fusion **34** (1992) 1173

[30] R.P. Schorn *et al.*, Appl. Phys. B **52** (1991) 71-78

[31] J. Schweinzer, Habilitation thesis, IPP report, IPP 1/323 (1999)

[32] S.P. Cunningham, Conference on Thermonuclear Reactors, US Atomic Energy Commission Report **279** (1955) 289

[33] B. Brosda, *Modellierung von Helium-Atomstrahlen und ihr Einsatz zur Plasmadiagnostik der Tokamakrandschicht*, PhD thesis, Ruhr-Universität Bochum (1993)

[34] T. Fujimoto, Institute of plasma paysics, IPPJ internal report, IPPJ-AM-9, Nagoja University, Japan (1978)

[35] S. Sasaki *et al.*, Rev. Sci. Instrum. **67** (1996) 3521-3529

[36] M. Brix, *Messung von Elektronentemperatur und -dichte mittels Heliumstrahldiagnostik im Randschichtplasma eines Tokamaks*, PhD thesis, Ruhr-Universität Bochum (1998)

[37] A. Maas, *Helium Distribution Functions in Tokamak Plasmas*, PhD thesis, JET Joint Undertaking (1995)

[38] B.A. Pohlmeyer, A. Dinklage, and H.J. Kunze, J. Phys. B: At. Mol. Opt. Phys. **29** (1996) 221-229

[39] F.M. Levinton, Rev. Sci. Instrum. **57** (1986) 1834-1836

[40] A.A. Korotkov, M. Samsonov, Ioffe Physico-technical Institute report (1989) I1351

[41] A.A. Korotkov, Nuc. Fus. **3** (1992) 79

[42] A.A. Korotkov, R.K. Janev, Phys. Plasmas **3** (1996) 1512-1523

[43] H. Anderson, PhD thesis, Univ. of Strathclyde, Glasgow (1999)

[44] D. Wutte, *Entwicklung und Aufbau eines Lithiumatomstrahl-Injektors und Beiträge zur Lithiumatomstrahl-Plasmarandschichtdiagnostik bei Kernfusionsexperimenten*, PhD thesis, TU Wien (1995)

[45] S. Fiedler, *Entwicklung einer 2.45 GHz-ECR-Ionenquelle*, diploma thesis, TU Wien (1991)

[46] M. Leitner, *Entwicklung einer 2.45 GHz-ECR-Ionenquelle für Anwendung zur Neutralstrahldiagnostik von Tokamak-Randschicht-Plasmen*, diploma thesis, TU Wien (1993)

[47] M. Proschek, *Umbau und Inbetriebnahme einer Ladungsaustauschzelle zur Erzeugung eines He^o-Neutralstrahls*, project work, TU Wien (1996)

[48] S. Bashkin, J. O. Stoner, *Atomic Energy Level and Grotrian Diagramms*, Department of Physics, Volume I, University of Aricona, Treson, North-Holland-Publishing

[49] R. W. McCullough, T. V. Goffe, and H. B. Gilbody, J. Phys. B: At. Mol. Opt. Phys. **11** (1978) 2333 - 2344

[50] D. R. Lide, *Handbook of Chemistry and Physics*, CRC Press, Boca Raton, Florida (1993)

[51] C. Reynaud, J. Pommier, V. Tuan Ngoc, M. Barat, Phys. Rev. Lett. **43** (1979) 579

[52] R. H. Neynaber, G. D. Magnuson, and S. Y. Tang, J. Chem. Phys. **68** (1978) 5112

[53] W. L. Wiese, M. W. Smith, and B. M. Glennon, *Atomic Transition Probabilities*, National Standards Reference Series, National Bureau of Standards, NSRDS-NBS 4, Washington (1966)

[54] C. F. Barnett, *Atomic Data for Fusion. Volume 1: Collisions of H, H_2, He, and Li Atoms and Ions with Atoms and Molecules*, ORNL-6086 (1990)

[55] A. Christmann, S. Seidel, and H. J. Kunze, Rev. Sci. Instrum. **70** (1999) 1627-1630

[56] A. Dinklage, T. Lokajczyk, and H.J. Kunze, J. Phys. B: At. Mol. Opt. Phys. **29** (1996) 1655-1665

[57] H. B. Gilbody, R. Browning, and G. Levy, J. Phys. B: At. Mol. Phys. **2** (1968) 230-232

[58] A. Matsumoto, S. Ohtani, T. Iwai, J. Phys. B: At. Mol. Opt. Phys. **15** (1982) 1871

[59] M. Hollstein, J. R. Sheridan, J. R. Peterson, and D. C. Lorents, Phys. Rev. **187** (1969) 118

[60] T. Hecht, H. Winter, and R. W. McCullough, Rev. Sci. Instrum. **68** (1997) 2693-2697

[61] A. Brazuk, HP. Winter, J. Phys. B: At. Mol. Opt. Phys. **15** (1982) 2233

[62] A. Brazuk, D. Dijkkamp, A. G. Drentje, F. J. de Heer, and HP. Winter, J. Phys. B: At. Mol. Opt. Phys. **17** (1984) 2233

[63] F. Aumayr, G. Lakits, and HP. Winter, Phys. Lett. **114A** (1986) 81

[64] H. Kayser, R. Ritschl, *Tabelle der Hauptlinien der Linienspektren aller Elemente*, Springer Publishing, Berlin (1968)

[65] A. Huber, *Apparatur zur Erzeugung und Untersuchung schneller gemischter Heliumatomstrahlen*, PhD thesis, TU Wien (1998)

[66] M. Noner, *Umbau und Inbetriebnahme einer Ladungsaustauschzelle*, project work, TU Wien (1994)

[67] M. Proschek, *Faradaycup zum Nachweis schneller Heliumneutralstrahlen*, diploma thesis, TU Wien (1998)

[68] R. Dobrozemsky, *Vakuumphysik und Messtechnik*, lecture script, TU Wien (1995)

[69] F. Aumayr, *Atomare Stoßprozesse*, lecture script, TU Wien (1997)

[70] W. Entler, *Design and Installation of an Electrostatic Lens and Beam Profile Measurement at the Atomic Beam System HELMA*, project work, TU Wien (1999)

[71] K. McCormick, IPP report III/82, IPP Garching, Germany (1982)

[72] E. Horsdal Pedersen, J. Heinemeier, L. Larsen, and J. V. Mikkelsen, J. Phys. B: At. Mol. Opt. Phys. **13** (1980) 1167-1183

[73] M. E. Rudd, T. V. Goffe, and A. Itoh, Phys. Rev. A **32** (1985) 829-835

[74] H. Eder, M. Vana, F. Aumayr, and HP. Winter, Rev. Sci. Instrum. **68** (1996) 165-169

[75] L. Woterbeek Muller, J. de Heer, Physica **48** (1970) 345

[76] R. Arrathoon, Phys. Rev. A **4** (1971) 203-207

[77] R. E. Miers and L. W. Anderson, Phys. Rev. A **1** (1970) 819-821

[78] H. S. W. Massey, H. B. Gilbody, *Electronic and Ionic Impact Phenomena*, vol. 4, Clarendon Press, Oxford (1974) 2793

[79] S. Fiedler, *Diagnostik von Fusionsplasmen mit schnellen Lithiumstrahlen*, PhD thesis, TU Wien (1994)

[80] M. Pöckl, *Bestimmung von Plasmaparametern mittels Li-Strahl-Diagnostik*, Diploma thesis, TU Vienna (1992)

[81] Z.A. Pietrzyk, P. Breger, and D.D.R. Summers, Plasma Phys. Control. Fusion **35** (1993) 1725

[82] K. Kadota *et al.*, J. Phys. B: At. Mol. Opt. Phys. **15** (1982) 3297

[83] H.P. Summers, Month. Not. R. Astr. Soc. **178** (1977) 101-122

[84] G. Dragosics, *Modellierung von Heliumstrahlen in Randschichtplasmen*, project report, TU Wien (1999)

[85] F.J. deHeer *et al.*, At. Plasma-Mater. Interact. Data Fusion **6** (1995) 7-26

[86] K.L. Bell *et al.*, Culham laboratory internal report, CLM-R216 (1982)

[87] G. Dragosics, *Über die Anwendung Neuronaler Netzwerke bei der Auswertung von Atomstrahl-gestützter Diagnostik von Kernfusionsplasmen*, diploma thesis, TU Wien (2000)

[88] O. Gruber *et al.*, Overview of the ASDEX Upgrade results, presented at the 18th IAEA Fusion Energy Conference, Sorrento, Italy, 4-10 October 2000

[89] HP. Winter, S. Menhart, Zwischenbericht zum Projekt *Orientierende Untersuchungen zur Heliumstrahldiagnostik an ASDEX Upgrade*, Friedrich Schiedel-Stiftung für Energietechnik (1999)

[90] S. Menhart, M. Proschek, H.D. Falter, F. Aumayr, and HP. Winter, Endbericht zum Projekt *Orientierende Untersuchungen zur Heliumstrahldiagnostik an ASDEX Upgrade*, Friedrich Schiedel-Stiftung für Energietechnik (1999)

[91] J. Schweinzer, private communication (1998)

[92] M. Brix, Abschlußbericht zum Forschungsauftrag Nr. 021/41362607/930 an die Forschungszentrum Jülich GmbH (1999)

[93] N. Hawkes and N. Peacock, Rev. Sci. Instrum. **63** (1992) 5164 -5166

[94] M. Brix, Zwischenbericht zum Forschungsauftrag Nr. 021/41362607/930 an die Forschungszentrum Jülich GmbH (1998)